Development of a Flexible Polarizable Water Model

by

Jing Ding

B.E. Shenyang Pharmaceutical University, Shenyang, China, 1999

M.S. Chinese Academy of Sciences, Beijing, China, 2003

Submitted to the Graduate Faculty of

Arts and Sciences in partial fulfillment

of the requirements for the degree of

Doctor of Philosophy

University of Pittsburgh

2011

UNIVERSITY OF PITTSBURGH

SCHOOL OF ARTS AND SCIENCES

This dissertation was presented

by

Jing Ding

It was defended on

June 3, 2011

and approved by

Rob D. Coalson, Department of Chemistry

Geoffrey Hutchison, Department of Chemistry

Wissam A. Al-Saidi, Department of Chemical and Petroleum Engineering

Kenneth D. Jordan, Department of Chemistry

Development of a Flexible Polarizable Water Model

Jing Ding, PhD

University of Pittsburgh, 2011

Development of a Flexible Polarizable Water Model

Jing Ding, PhD

University of Pittsburgh, 2011

A flexible polarizable water model, DPP2-F, has been developed and its applications to vibrational analysis of water clusters are discussed in this dissertation. The total potential energy function, including intramolecular distortion, point-charge electrostatic, charge penetration, polarization, charge transfer, dispersion and exchange-repulsion contributions, has been evaluated term-by-term with the aid of energy decomposition approach of the Symmetry Adapted Perturbation Theory (SAPT). Detailed error analyses on all potential energy terms are carried out to interpret how the different energy terms balance within the model. The new parameterization scheme improves the water molecular polarizability surface and leads to an increased dipole derivative of the hydrogen-bonded OH stretch. The DPP2-F model successfully predicts the vibrational frequency redshift that happens to the hydrogen-bonded OH vibration, and the appreciation of the vibrational intensity. The magnitudes of these features, however, are severely underestimated by the DPP2-F model. Also included are brief introductions to several other projects undertaken during my graduate study: the *ab initio* molecular dynamics study on $(H_5O_2)^+$, the reparameterization of excess electron-water interaction potential, the transition state of $(NO_2 \cdot H_2O)^-$, the calculation of vibrational spectra of $(H_2O)_n^-$ and $[CH_3NO_2 \cdot (H_2O)_6]^-$.

TABLE OF CONTENTS

LIST OF TABLES

LIST OF FIGURES

LIST OF KEYWORDS

DPP. The rigid water model developed in Jordan group, used in excess electron-water interaction model.

DPP2-R: A second-generation rigid water model developed in the Jordan group, with explicit charge penetration and charge transfer energy components.

DPP2-F: The flexible polarizable water model discussed in this document. It shares similar potential energy function with the DPP2-R model.

PS-PES and **PS-DMS.** The water potential energy surface and dipole moment surface presented by Partridge and Schwenke in 1997. It is used to calculate the intramolecular energy and the partial charges of the flexible water structures in the DPP2-F and TTM2(4)-F models.

TTM2-F. The flexible water model reported by Burnham and Xantheas in 2002, the first flexible water model with geometry-dependent point charges.

TTM4-F. The flexible water model reported by Burnham in 2008, with an excellent prediction of vibrational frequency and intensity associated with the hydrogen-bonded OH bond. Unlike its other TTM flexible models, it employs a modified exponential form of induced dipole damping.

AMOEBA. The flexible and polarizable model potential developed by Ponder group. It employs higher-order multipoles in the electrostatic interaction.

Polarizable water models: AMOEBA, DPP/DPP2, NEMO, TTMn(n=2-4), SIBFA.

Non-Polarizable water models; SPC, TIP4P, TIP5P.

SAPT. Symmetry Adapted Perturbation Theory, the energy decomposition scheme used in this work.

Drude/CI. The one electron-water interaction model developed in the Jordan group. It uses Drude oscillators and configuration interaction (CI).

PM3. The one electron-water polarization potential developed in the Jordan group.

PREFACE

My deepest gratitude is to my advisor, Professor Kenneth D. Jordan for his guidance, patience, understanding and supports during my graduate studies at the University of Pittsburgh. Much of my knowledge in the quantum mechanics theory and computational science came from this precious spell of time. Ken's always kind and patient mentorship and his incise way of approaching the fundamental problems are paramount for me to achieve my long-term professional goals!

I am indebted to the faculty members in the Eberly Hall, Professor Rob Coalson, Professor Wissam Al-Saidi, Professor Geoffrey Hutchison and Professor Lillian Chong for the teachings and their kind suggestions to my research!

I have benefited enormously from discussions with many former Jordan group members, Professor Thomas Sommerfeld, Dr. Hao Jiang, Dr. Jun Cui, Dr. Albert Defusco, Dr. Tae Hoon Choi, Dr. Haitao Liu, Dr. Daniel Schofield, and the current group members! Special thanks go to Dr. Revati Kumar and Dr. Fangfang Wang for many helpful discussions on the water models.

I am also thankful to Dr. Richard Christie and the SAM team for the many years' assistance on the carrying out calculations!

I would like to thank the Department of Chemistry at the University of Pittsburgh especially, Elaine Springel and Fran Nagy, for providing us such an easy studying environment!

To my family!

1.0 INTRODUCTION

Research on water clusters plays a vital role in understanding the connection between the gas phase water molecular aggregates and the macroscopic condensed phase of water and allowing us to isolate particular hydrogen-bonded morphologies and then to predict how these networked "supermolecules" adapt and rearrange when exposed to different chemical and physical environments. Research developments in *ab initio* quantum chemistry approaches allow accurate theoretical calculations of water clusters consisting of up to hundreds of molecules and thereafter provide an unprecedented opportunity to investigate how the special arrangement of water molecules lead to the wide range of unique properties of liquid water, ice and many other aqueous systems.

The last ten years has seen the breakthrough at the molecular level, in the understanding of many interesting physical phenomena associated with water clusters, i.e. proton transfer,[1] electron-localization,[2] gas hydrate,[3] and unique properties associated with water. For instance, it had been noticed that the $H^+(H_2O)_n$ mass peak with n = 21 was unusually intense relative to those around it. This anomalous intensity was ascribed to an unusual stability for this cluster size, which is referred to as a "magic number". [4]

Water cluster anions provide a model system to unravel how hydrogen-bonded water network deforms to accommodate the excess electron [5] and help in understanding the free

electron hydration at a molecular level. Photoelectron spectroscopy of water clusters anions provides evidence for at least three isomeric classes I–III, characterized by different vertical electron detachment energies (VDEs). [6] Class I isomers bind an excess electron most strongly, followed by Class II. Class III isomers very weakly bind excess electrons. VDEs of class I and II isomers show a linear relationship with respect to $n^{-1/3}$, in which n is the number of molecules. Plotting VDE versus $n^{-1/3}$ and extrapolating the two lines to liquid water leads two intercepts, at 1.6 and 3.3 eV, which were interpreted by some researchers as the surface-solved state and bulk-solvated states. The localization of the excess electron in bulk water or water clusters is of great interest to scientists. The excess electron may choose to form "interior-bound" states, in which the electron density is mainly confined within water network, or to form "surface-bound" states, in which the excess electron is bound to the surface of water. The bifurcation of the VDE extrapolation of the class I and class II isomers, enticed scientists to speculate on whether the excess electron is surface-bound or interior bound, or both in liquid water and water clusters. [7, 8] Structural information from experiments and calculations on isolated hydrated electron clusters has, however, remained controversial. [9, 10]

Infrared (IR) photodissociation studies lead to detailed insights into the structure and binding in hydrated electron clusters. [11] It has been demonstrated that, for water cluster anion $(H_2O)_n^{-1}$, $n < 25$, the excess electron is bound by a "double acceptor" water molecule, with both hydrogen atoms oriented toward the excess electron, (instead of forming H-bond in neutral water cluster) and the direction of the collective dipole of the water network. This type of structures is usually referred as the AA motif and is characterized by a uniquely redshifted bending band in the 1500–1550 cm^{-1} region together with characteristic spectral signatures in the OH stretch. [12]

Valuable structural information of various water clusters can be elucidated through a combined analysis of their vibrational band patterns in the OH stretching and intramolecular bending regions. Computing vibrational spectra is of great theoretical interests, because the vibrational signatures contain rich information of the structures and dynamics. [13] Two approaches for generating vibrational spectrum are mentioned here. First one is harmonic vibrational spectra based on normal mode approximation, which is extremely useful for assigning the spectra. Frequencies usually are scaled to cover anhamonicity. For systems with strong anharmonic effects, i.e. large amplitude mode, cross-mode coupling etc., anharmonic correction methods can be employed, though they may not be able to handle many interesting systems. Harmonic spectra require gradient and hessian matrixes calculations and are computationally very prohibitive for large water clusters and usually become impossible for condensed states of water. It is limited to the static picture at 0 K, and does not reflect the finite temperature effects directly on the measured vibrational spectra.

The other approach produces the vibrational spectrum by calculating the dipole-dipole correlation functions from dynamics simulations. [14] It includes the temperature and anharmonic effects. In practice, the approach is implemented in classical molecular dynamics and makes use of density functional theory (DFT) or classical molecular mechanics (force fields). Due to the classical nature of molecular dynamics, quantum effects are missing from such simulations. Quantum corrections based on centroid and path-integral scheme have been employed for studying the Infrared (IR) spectroscopy of liquid water and ice. [15, 16]

Different as they are, both approaches require accurate descriptions of the potential energy and dipole moments. Thanks to the last three decades' continuing effort, tremendous amount of simulations, molecular dynamics (MD), Monte Carlo (MC), free energy calculations,

had been carried out on system with hundreds of thousands of atoms. Among them the theoretical work on protein folding has demonstrated the power of supercomputers and the success of wisely-crafted force fields or molecular modeling approaches. However, the accuracy of such simulations is crucially influenced by the analytical model chosen to represent the intermolecular interaction energy. Development of force fields has been an actively explored research field for over thirty years. A representative example is from the recent advancement in crystal structure prediction (CSP). [17] Neumann, Leusen and collaborators constructed a non-transferable force field, [18] named the tailor-made force field (TMFF) and parameterized all energy terms in TMFF to reference data generated by dispersion-corrected density functional theory method for target molecules. They applied this approach to the first three blind tests in CSP, and successfully located the observed crystal structures as the most stable form of packing for eight out of ten molecules. [19]

My doctorate research is composed of projects on water clusters: protonated water clusters, water clusters attached with excess electron, nitromethane and NO_2 water complex, and the flexible water force field DPP2-F.

Jordan group have previously developed rigid water models, DPP [20] and DPP2-R [21]. Both models involve explicit parameterizations in the polarization energy term and separation of dispersion and repulsion interactions. The DPP2-R model, however, goes beyond the DPP model by augmenting the electrostatic energy with charge penetration and introducing explicit charge transfer term into total intermolecular interaction energy. Based on these work, a new polarizable flexible model was developed and it was named as DPP2-F for convenience. This document is dedicated to the model work.

In the present DPP2-F model, a reported potential energy surface of water molecule with generated geometry-dependent atomic charges from the corresponding dipole moment surface is employed to model the intramolecular flexibility. Excluding this intramolecular distortion contribution, the total potential energy function of the DPP2-F model has similar terms to the DPP2-R model, with interactions of electrostatic, polarization, charge transfer, dispersion and exchange repulsion. A different charge-penetration damping scheme is used to replace the one used in DPP2-R. Most of the changes happen in the polarization interaction. The charge-(monomer-geometry-) dependent atomic polarizabilities of hydrogen and oxygen sites and modified charge-induced dipole damping scheme have been employed and lead to improved monomer molecular polarizability surface. Differing from the DPP2-R and DPP model, the intermolecular polarization is parameterized to calculate *ab initio* dipole moments of water clusters. The dipole moments from MP2 display a steep slope along the internal O-H bond. This is a crude approximation to the dipole derivative of the H-bonded OH stretch. DPP2-F has been partially recovered this feature, which is closely related to the strong intensity of this vibrational mode. The construction of DPP2-F is done based on term-by-term fitting to the Symmetry Adapted Perturbation Theory (SAPT), [22] energy components. The exchange-repulsion part, however, is determined by fitting to the difference between MP2 interaction energies and the sum of all other energy components in the models. The model was inspired by our test work on using water force fields to calculate vibrational frequencies of water cluster anions. It is being developed with a strong motivation for water cluster vibrational analysis. There are many interesting and also challenging issues here. I have touched some of them in the text and I am hoping that this work would contribute to a better understanding of them.

In appendix A, I briefly introduce the electron-water interaction model potential work that I have done. Drude/CI and polarization models are reparameterized in a consistent way.

Appendix B contains the paper on the IR spectrum of protonated water cluster ($H_5O_2^+$) and its deuterium-substituted isotopologues using *ab initio* molecular dynamics.

Apprentice C is the paper on the vibrationally induced interconversion of H-bonded NO_2^-·H_2O Isomers.

Apprentice D is the paper on the vibrational spectral signature of the $(H_2O)_7^-$ network through the double resonance spectroscopy.

Apprentice E contains the abstract of the manuscript on the IR study of nitromethane water complex anion $[CH_3NO_2 \cdot (H_2O)_6]^-$.

Figure 1 shows some representative water cluster structures studied in my research. The first is the global water dimer minimum with a Cs symmetry. It has been used extensively in the water model development. The four water hexamer isomers have been widely used to parameterize and test models. "Prism" is the lowest-energy minimum, with the energy close to that of "cage". Starting from water heptamer, the clusters are forming 3-D networks, consisting of four-, five-, and six-member rings. The representative structures of larger water clusters $(H_2O)_8$, $(H_2O)_{20}$, $(H_2O)_{24}$, and $(H_2O)_{30}$ are shown. When a free electron is attached with water clusters, the cluster structures change dramatically to accommodate the diffuse excess electron. The dimer, tetramer, and hexamer anion are AA-type isomers. It is a characteristic type of water anions, in which the two hydrogen atoms from the same water are pointing toward the excess electron. As the water cluster size grows, one might imagine that water molecules tend to form spherical network with more H-bonds and minimize the penalty from the electron distortion. This leads to so called cavity-bound isomer, in which electron density is mostly confined with

the water network. Whether the excess electron is localized with the cluster to form a cavity-like structure, or sits at the surface of the cluster remains unclear and raises numerous debates. Both experimental and theoretical approaches have their limitations. [23, 7, 24]

Water clusters with large static dipoles tend to bind excess electrons, but zero dipole clusters may also strongly bind electrons. This comes from dispersion interaction, which needs be treated with accurate electron correlation approach and usually is not well described by conventional density functional theory (DFT) methods. [25] $(H_2O)_{24}^-$-A and $(H_2O)_{24}^-$-B, are studied in Appendix A. Both have zero dipole moments due to symmetry. $(H_2O)_{24}^-$-A is spherical and binds electron tightly with an electron binding energy (EBE) as high as 0.7 eV, while $(H_2O)_{24}^-$-B assumes a flat network and only binds electron weakly with an EBE of less than 0.1 eV.

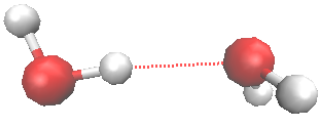

$(H_2O)_2$ - Cs

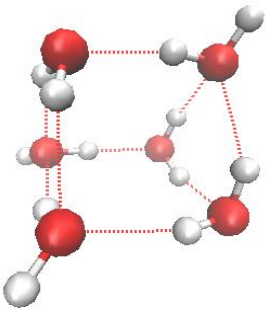

$(H_2O)_6$-Prism

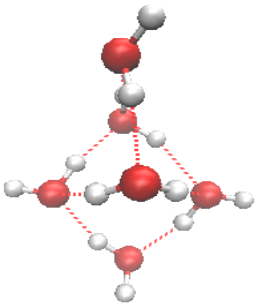

$(H_2O)_6$-Cage

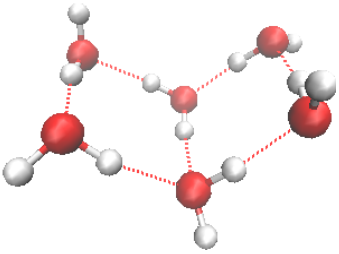

$(H_2O)_6$-Book

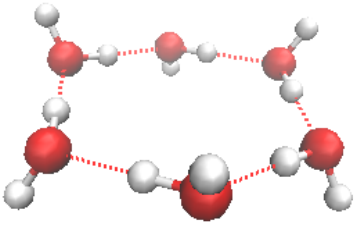

$(H_2O)_6$-Ring

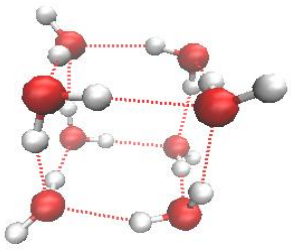

$(H_2O)_8$-D_{2d}

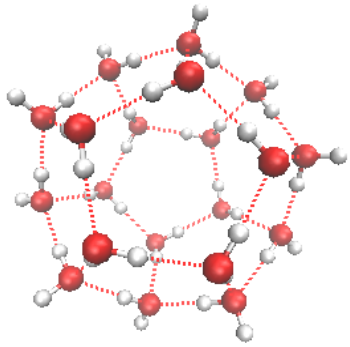

$(H_2O)_{20}$-cage

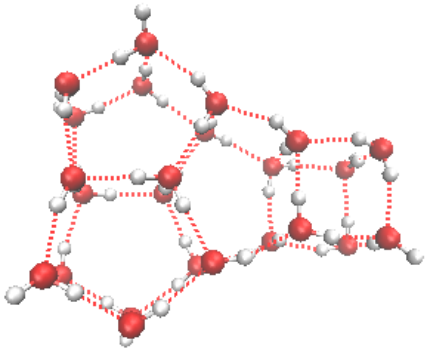

$(H_2O)_{24}$

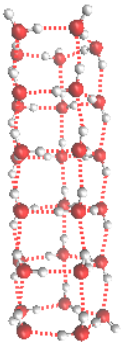

$(H_2O)_{30}$

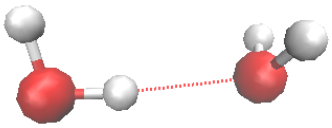

$(H_2O)_2^-$

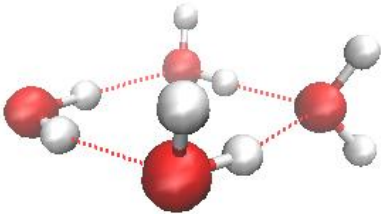

$(H_2O)_4^-$-Ring

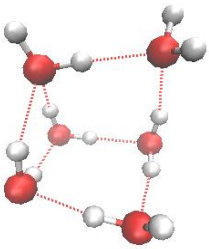

$(H_2O)_6^-$-AA

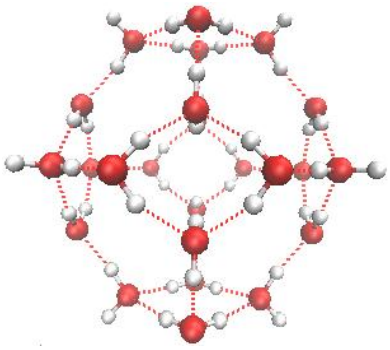

$(H_2O)_{24}^-$ A

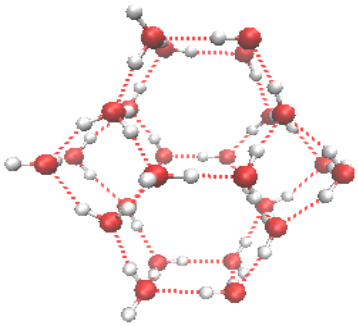

$(H_2O)_{24}^-$ -B

Figure 1. Some representative water clusters and water cluster anions studied in the research.

2.0 INTRODUCTION TO FLEXIBLE WATER MODEL

2.1 FORCE FIELDS AND WATER MODELS

In conventional molecular mechanics (MM), the total potential energy of a molecular system, takes the general expression as follows in term of atomic units,

$$E_{intra} = \frac{1}{2}\sum_{bonds} K_r \left(r - r_{eq}\right)^2 + \frac{1}{2}\sum_{angles} K_\theta \left(\theta - \theta_{eq}\right)^2 + \sum_{dihedrals} \frac{V_n}{2}\left(1 + \cos\left(n\phi - \gamma\right)\right) \qquad (1)$$

$$E_{inter} = \sum_{i<j}^{electrostatic} \frac{q_i q_j}{r_{ij}} + \sum_{i<j} 4\varepsilon_{ij}\left[\left(\frac{\sigma_{ij}}{r_{ij}}\right)^{12} - \left(\frac{\sigma_{ij}}{r_{ij}}\right)^{6}\right] \qquad (2)$$

$$E_{total} = E_{intra} + E_{inter} \qquad (3)$$

E_{intra} is the intramolecular energy that results from bond stretching, valence angle bending, and torsional rotations along rotatable bonds, in which K_r , K_θ and V_n are force constants for bonds, angles and torsional angles; r_{eq} and θ_{eq} are equilibrium values for bonds and angles; and γ is the dihedral angle phase.

E_{inter} describes the intermolecular interactions between different water molecules. For super-molecular clusters with many molecules, the intermolecular interaction, defined as $E_{inter}\left(AB\right) = E_{AB} - E_A - E_B$, typically contains point-charge electrostatic interaction and Lennard-

Jones type interactions, both of which are two-body interactions coming between sites from distinct molecules. In the equation (2), r_{ij} is the intermolecular distance and ε_{ij} and σ_{ij} are characteristic pair parameters between atom *i* and *j* for the L-J type interaction.

Depends on the motivation, there are two categories of Force field. [26] Class I force fields, including AMBER,[27] CHARMM,[28] OPLS,[29] and GROMOS,[30] are based on the above potential energy functions, with variations to different extents. These force fields are constructed and parameterized to reproduce condensed state properties (e.g. thermodynamic and structural properties). They are commonly used in Monte Carlo and molecular dynamics simulations. Despite missing explicit many-body interaction terms, these force fields tend to absorb many-body energy contribution into their pair-wise two body potential in an effective way.

Class II force fields, are parameterized something similar to many semiempirical approaches, to more precisely reproduce molecular and cluster structures, conformational equilibrium, and molecular vibrations. Some examples are MM3,[31] MM4,[32] and UFF [33]. These force fields usually go beyond the simple harmonic potential expression and introduce higher-order anharmonic potentials and cross-term functions for the intramolecular interaction. Compared with Class I force fields, Class II force fields, however, often fail when applied to condensed phase simulations.[34] Some of reasons will be discussed later. In general, at the current state, the force fields still do not allow very large scale simulations of condensed states while being at the same time accurate enough for satisfactory conformational analysis.

Classical water models serve as the basis for classical molecular dynamics and Monte Carlo simulations of many interesting properties of water. [35] One of the grand challenges tackled by modern theoretical chemistry is the accurate modeling of intermolecular interactions. The

knowledge associated with developing water models, enable one to better understand the intermolecular interactions and improve the performance of current molecular modeling scheme.

The development of water models generally starts from the rigid-body approximations, in which, a C_{2V} rigid water molecular geometry with a fixed OH bond distance and HOH bending angle is used. The O-H distance and HOH angle, based on the known geometry of water molecule, are chosen to give good reproduction of water structures or properties of water clusters or liquid water. For example, the SPC water model [36] assumes an ideal tetrahedral shape, with an O-H distance of 1.0 Å and HOH bend angle of 109.47 °. The gas-phase water geometry with an O-H distance of 0.9572 Å and an HOH angle of 104.52 °, however, has been widely used in water models, especially in polarizable water models, which are parameterized to quantum mechanics data.

An alternative practice recommended by Jeziorska uses vibrationally averaged water monomer structures. [37] For instance, a geometry with O-H distances of 0.9716 Å and a HOH angle of 104.69 °, had been used in SAPT-ss, SAPT-5s potentials[38, 39] and by Jansen et al. as well [40]

Assuming a rigid geometry, the simplified water model potential is left with only intermolecular contributions, containing electrostatic (Coulomb term) and Lennard-Jones terms. There are three routes to refine water model potentials. The first is the explicit inclusion of polarization contribution. The second is the improvement of the electrostatic interactions at the short-range distances and going beyond the simple point charges representation. The third consists of refining the representation of the Lenard-Jones term, by separating it to a short-range repulsion and a long-range attractive dispersion.

2.2 POLARIZATION SCHEME

Over the past decade it has become possible on a routine basis to accurately compute intermolecular interactions from quantum chemical calculations. Development of energy decomposition schemes [41] even allows one to study the potential components on a term-by-term basis. [42] Molecular polarization methods play a central role in the next generation of force fields for molecular simulations. This is mainly due to the fact that it is increasingly important to simulate heterogeneous environments, which requires that a given molecular model be able to provide an environment-dependent response. [43] In the condensed phase of water, the two-body interaction energies account for only about 70% of the total interaction energy per molecule. [44] The remaining 30% arises from non-additivity, that is, the interaction energy cannot be represented by a sum of pair-wise interactions. This non-additivity plays a significant role in hydrogen-bonding and is responsible for many important structural properties.

Induction refers to the redistribution of a molecule's electron density due to the electric field exerted by other molecules. [45] If more than two molecules are involved, induction leads to non-additivity, since two molecules will interact differently when polarized by a third molecule than if the third molecule is not present. The use of polarizable force fields dates back to the work of Warshel and Levitt, [46] who introduced this approach as a general way of capturing the effect of electronic polarization and the corresponding dielectric constant in the early-stage QM/MM simulation of protein modeling. For over thirty years, many attempts have been made to include the effects of polarization in simulations of molecular systems.

Simulations using polarizable models are orders of magnitude slower than nonpolarizable models. Non-polarizable water models, sometimes called as the first generation water models,

generally implicitly include the average polarization, a many-body feature, in their effective pair-wise potential functions, by parameterizing to condensed phase properties and measurable experimental information. Selective parameterization enables these models to reproduce a variety of thermodynamic (structural observables, solvation free energies, etc.) and kinetic (diffusion, rotational correlation times, hydrogen bond dynamics, etc.) The straightforward implementation and fast evaluations of energy and forces make such models extensively used in large-scale simulation of liquid water and ice.

The major dilemma faced by the molecular modeling is that an increase in the level of sophistication of the current potential energy functions limits the sampling ability in statistical simulations. For example, the crystallization process has attracted researchers' interest for its widespread applications in chemistry, materials and pharmaceutical industries. [47] It starts off from nucleation, a rare-event process, which makes it hard to model computationally. The crystal growth is a very slow process, and so far is only achievable by molecular simulation for simple systems. Many chemical and biophysical phenomena occur over significant time scales, [48] or require a huge number of simulation steps. [49] Minimalist force fields, with efficient energy and force calculations, allow the large-scale simulation for very complex problems.

The compromise will evidently be dictated by the problem investigated and the nature of the systems. Although for large, complex assemblies of atoms and molecules, especially condensed phase species, neglecting polarization response and assuming a rough representation of electrostatic by Coulomb interactions may prove to be satisfactory at a statistically qualitative level, it is often desirable to improve the description of the constituent molecules by means of more sophisticated potential energy functions.

There are generally three categories of polarizable force fields: the induced point dipole model, [50,51] the fluctuating point charge (FP) model (also known as electronegativity equalization model),[52,53,54] and the classical Drude oscillator model [55] (also known as the shell model or charge-on-spring model). In the first two approaches, either atomic point dipoles or atomic charges are allowed to change in response to the environmental electric field. In the Drude oscillator model, an induced dipole is represented as a pair of point charges connected with a harmonic spring.

The induced dipole approach has been widely adopted in molecular mechanics and is also used in the current work. An incomplete list of such models includes EFP, [56] ASP-W, [57] NEMO, OPEP, [58] AMOEBA, [59] Dang-Chang, [60] TTM-series and many others. The electrostatic field is generally screened according to the formalism proposed by Thole, [50] while an interesting exception is SIBFA model, which resorts to screening by means of Gaussian damping functions.

Table 1. Structural details and dipole moments of the water molecule (W1) and water dimer (W2) calculated from some popular water models, including nonpolarizable models, TIP4P, TIP5P and SPC, and polarizable models AMOEBA, POL-5/TZ and DPP.

	Properties	GAS/EXP [67]	TIP4P [61]	TIP5P [62]	SPC[36]	AMOEBA [63]	POL-5/TZ [64]	DPP [20]
W1	d(OH)/Å	0.9572	0.9572	0.9572	1.00	0.9572	0.9572	0.9572
	HOH/ º	104.52	104.52	104.5	109.5	108.5	104.5	104.5
	dipole/D	1.855	2.18	2.29	2.27	1.77	1.85	1.85
W2	d(OO)/Å	2.976	2.748	2.679	2.734	2.892	2.896	2.890
	dipole/D	2.64	2.71	2.92	3.74	2.54	2.44	2.76

Table 1 compares the distance between oxygen atoms in each optimized water dimer and its dipole moment, calculated with some popular nonpolarizable water models, SPC, TIP4P, [61]

and TIP5P [62] and polarizable water models, AMOEBA, [63] DPP and POL/5Z [64]. Nonpolarizable models generally give poor estimates of gas-phase cluster properties. They systematically underestimate the O-O distance to giving values around 2.7 Å and overestimate the total dipole moments. In comparison, polarizable water models, generally yields satisfactory dipole moments, and O-O distances closer to the *ab initio* value near 2.9 Å. Similar results have been reported by Kiss and Baranyai, who calculated the properties of small water clusters up to water hexamer, with a range of widely-used nonpolarizable and polarizable models. [65] Since water molecules are more closely packed when nonpolarizable model is used, the hydrogen-bonded network of water can be seriously biased, raising a big question mark on the results computed using such models. Considerable polarization interaction exists in water and other polar liquids, leading to a cooperative strengthening of intermolecular bonding. Thus these water molecules display greater dipole moments than the isolated molecules. Simulations of condensed water based on the use of pairwise additive potentials generally require exaggerated monomer dipoles of 2.3 to 2.4 D to reproduce experimental data and the increase in dipole moment on going from the gas to the condensed phase would not be accurately described without polarizability being accounted for explicitly. [66]

In the gas phase, dipole moment of a water molecule measured in experiments is 1.855 D. [67] This value has been confirmed by high-level *ab initio* quantum chemistry calculations. Recent X-ray diffraction measurements of bulk water [68] lead to an estimate of the dipole of 2.9 ±0.6 D at ambient conditions. Theoretical calculations based on different water models give very different dipole moments for the liquid water. The dipoles obtained from the classical induction models fall around 2.5–3.2 D, depending on the empirical parameters used. The DFT molecular dynamics simulation on bulk water at 318 K and 1.0 g cm^{-1} from Silvestrelli and Parrinello [69]

yielded a total dipole moment 3.0 D of the water molecule, a value larger than those obtained from other calculations. The large spread in the reported values of the average dipole moment of liquid water reflects the fact that our understanding of water molecule interaction in condensed phases is still rather limited.

As one might wonder, it is possible that it is not sufficient to have a limited number of induced dipole sites in the mode, say three polarizable sites in most water models. Lindh et al. reported in the NEMO force field, [70,71] that they included quadrupole moment and higher-order polarizabilities up to quadrupole–quadrupole polarizability and found the model gives a better description of the intermolecular interaction for formaldehyde. Due to the complexity of the implementation and inefficiency in force evaluations, research about this is limited.

2.3 BEYOND POINT-CHARGE REPRESENTATION

The electrostatic interaction is represented as a Coulomb interaction between two unperturbed monomer charge distributions,[72] ρ^A and ρ^B,

$$E_{Coul} = \iint \frac{\rho^A\left(\vec{r}_A\right)\rho^B\left(\vec{r}_B\right)}{\left|\vec{r}_A - \vec{r}_B\right|} d\vec{r}_A\, d\vec{r}_B \qquad (4)$$

In the equation (4), the Coulomb operator $\frac{1}{\left|\vec{r}_A - \vec{r}_B\right|}$ is expanded in a Taylor series. [73] In most force fields, electrostatic interactions are modeled using simple Coulomb terms involving interactions between partial atomic charges on atoms or on other sites. The point charge approximation has

an ambiguous physical nature due to the fact that charges of atoms in molecules are not quantum mechanical observables. The point charges, assigned to nuclei atoms or off-atom centers, are typically determined by fitting to the molecular electrostatic potential (MEP) of water molecule.[74]

For water models, three point charges are commonly used to represent the charge distribution of one water molecule. A straightforward assignment is to place the partial charges on O and H atoms, i.e., the SPC model. Another widely used point-charge model, TIP4P, also has three point charges; in the model, however, the negative charge is at an off-atom site, denoted as *M*-site, along the bisection of HOH, instead of on O atom. Introducing the off-atom *M*-site into the electrostatics leads to a better description of quadrupole moments of water molecules.

From a practical perspective, it is tempting to compute electrostatic energy in terms of atomic quantities that can be used directly in molecular mechanics calculations. Conceptually, this approach relies upon some kind of partitioning of the total charge density into regions of Cartesian space that correspond to atoms, e.g. the formalism of atoms-in-molecules proposed by Bader, which relies upon the topological partitioning of molecular charge densities. [75]

Three point charge models lack sufficient mathematical flexibility to describe the electrostatic potential around water molecules. A variety of improvements have been proposed, including introducing additional off-nuclei point charges, [76, 77] the use of higher-order multipole expansions, e.g., up to quadrupole moment, contributions at each nuclear center or chemical bond, [78, 79, 80] the inclusion of penetration effects,[81] and quantum mechanics-like treatment of the charge distribution.[82, 83]

In the 5-site model TIP5P proposed by Mahoney and Jorgensen, [62] a positive charge of $0.241e$ is placed on the hydrogen atomic site and charges of equal magnitude and opposite sign are placed on the lone pair interaction sites. Its more "tetrahedral" water structure results in improvements in reproducing the experimental radial distribution functions from neutron diffraction and the temperature of maximum density of water. TIP5P, however, actually performs even poorer than TIP4P for the water dimer, and generates a large number of extra structures with deep energies not found in the configuration search of other models or quantum chemical calculations.

It is now well known that molecular charge densities can be represented quite accurately, using multi-centered multipolar expansions. [84] The electrostatic interaction energy between two atoms or centers, A and B, on two different molecules, expanded to the level of quadrupole moments is given by

$$\begin{aligned} E_{elst}^{AB} &= f_1(AB)T^{AB}q^A q^B + f_2(AB)T_\alpha^{AB}\left(q^A\mu_\alpha^B - q^B\mu_\alpha^A\right) \\ &+ f_3(AB)T_{\alpha\beta}^{AB}\left(\frac{1}{3}q^A\theta_{\alpha\beta}^B - \mu_\alpha^A\mu_\beta^B + \frac{1}{3}\theta_{\alpha\beta}^A q^B\right) \\ &+ f_4(AB)T_{\alpha\beta\gamma}^{AB}\left(\frac{1}{3}\theta_{\alpha\beta}^A\mu_\gamma^B - \frac{1}{3}\theta_{\beta\gamma}^B\mu_\alpha^A\right) + f_5(AB)T_{\alpha\beta\gamma\delta}^{AB}\frac{1}{9}\theta_{\alpha\beta}^A\theta_{\gamma\delta}^B \end{aligned} \qquad (5)$$

where q^A is the charge, μ_α^A the α component of dipole moment, $\theta_{\alpha\beta}^A$ the $\alpha\beta$ component of the quadrupole moment of atom A. $T_{\alpha\beta}^{AB}$ is interaction tensor, defined as $T = \nabla^{(n)}\frac{1}{r}$,where n is the order of the tensor. The details will be discussed later. $f(AB)$ is the damping function, for instance, the Tang-Toennies damping [85] as used in NEMO. The quality of such high-order multipole models depends on both the number and the location of the centers, as well as on the

length of the expansion. Williams [86]studied the optimal least-squares fits of partial point charge electrostatic models. His results showed that relative root mean square errors, 3-10% over a set of grid points of a series of small polar molecules, has been reduced by 2-3 orders of magnitude via use of atomic multipoles through the quadrupole at each atom-center. His approach was adopted by AMOEBA model. [63] The multipoles can also be distributed both on the atoms and the chemical bonds. Day [87] has shown that in order to reproduce the *ab initio* molecular electrostatic potential, an expansion up to quadrupole moments was sufficient if the distribution was on atoms and bonds. Resorting to octupoles was necessary to ensure for such an agreement if the development was on the sole atomic centers.

Going beyond the high order multipoles, Gaussian electrostatic model (GEM), [88]a force field based on a density fitting approach using *s*-type Gaussian functions, has been presented within the SIBFA force field. This is probably the only model so far to get the energy components of all the ten stationary points of water dimer to excellent agreement with *ab initio* reference data. A Gaussian Multipole Model (GMM) [89] was also reported by the same authors.

The penetration contribution (E_{pen}) is a component of the *ab initio* Coulomb interaction. [73] When the two molecules are brought close enough, such that their charge densities overlap, the nuclei on one molecule will no longer be shielded by its own electron density, and will experience a greater attraction for the electron density associated with the other species. [90] The essence of penetration effects cannot be simply described by point charges or distributed multipoles.

Explicit introduction of E_{pen} has been done in the framework of the EFP potential, SIBFA procedure and a few other models. [91, 92, 93] The short-rage penetration effect is neglected

in all empirical models, and most *ab initio* based models. One can also consider that the effect is implicitly and partially recovered through exchange-repulsion, in the van der Waals (vdW) term in some force fields. The exchange-repulsion decays exponentially with distance. Murrell and Teixeira-Dias have shown that charge penetration (E_{pen}) and exchange-repulsion energies E_{ex-rep} behave similarly and suggested the following relation between the two:

$$E_{ex-rep} = -E_{pen}\left(a + bR\right) \qquad (6)$$

where a and b are empirical parameters, and R is the intermolecular separation. [94]A convenient way to calculate charge penetration between molecules is to introduce a damping function that multiplies the electrostatic potential. It was pointed out that damping of atom-centered point charges is more important than using distributed multipoles. [92]

2.4 SEPARATING LENNARD-JONES INTERACTION EXPRESSION

Nonbonded Lennard-Jones interactions are commonly modeled with the "6–12" Lennard-Jones potential, in which the attractive term falls off with distance as R^{-6} and the repulsive term as R^{-12}, where R represents the distance between two atoms. The vdW interactions generally include only the pair-wise two-body repulsive-attractive interactions acting between oxygen sites. Burnham et al. recently turned to six-term polynomial of r_{OO}^{-n}, with n = 6, 8, 10, 12, 14 and 16, to describe the repulsion and dispersion interactions, and they concluded that inclusion of r_{OO}^{-14} and r_{OO}^{-16} improved the model at short-range. [119]

The apparent limitation of such approaches is that, the interaction only depends on the distances between oxygen atoms and does not change in response to the water molecule configurations, orientation and associated "stereo effect". Apparently, models using this simplification are not appropriate to describe the "flap angle", [20] and they are insufficient for many water clusters. In fact, it had long been proposed that anisotropic repulsion of both oxygen and hydrogen should be taken into account in model development. [95] The simplification, however, is potentially advantageous for simulating condensed state and carrying out minimization of small water clusters.

The attractive component of intermolecular interaction can be represented by a dispersion term that is computed as a sum of R^{-n} terms. For example, SIBFA has R^{-6}, $R^{-8,}$ and R^{-10} in its dispersion term. [96] Dispersion interaction has been modeled with satisfactory accuracy by only keeping the leading R^{-6} term, i.e., in ASP-W,[97] and DPP/DPP2. Many variations, however, have been reported, for instance, it is computed as a sum of buffered R^{-7} terms in AMOEBA model.

Repulsion between atoms is generally modeled by a single term that is proportional to either an inverse power of R (R^{-9}, R^{-12}, R^{-14}) or more accurately, by terms that are proportional to $\exp(\alpha R)$. [98] The latter expression is preferred because the exchange-repulsion energy depends on the overlapping of molecular electronic densities and, thus, exhibits an exponential dependence on *R*. An interesting variant of this kind of exponential repulsion,

$$E_{rep}^{AB} = q_A q_B k_A k_B e^{-r_{AB} b_{AB}} \qquad (7)$$

is used by NEMO, in which q_A is the valence charge for atom A and k_A are atomic parameter fit to quantum mechanics data.

2.5 COMPUTING VIBRATIONAL SPECTROSCOPY WITH FLEXIBLE WATER MODELS

Experimental determination, such as nuclear magnetic resonance (NMR) and neutron diffraction, [99, 100, 101, 102] of the geometry of water molecule within liquid water and the ice lattice have reported that the bend angle (θ_{HOH}) and the O-H separation (R_{OH}) of the water monomer in the liquid water and ice are larger than those of the isolated gas phase monomer (104.52 ° and 0.9572 Å). For liquid water the monomer bend angle increases to θ_{HOH} = 106.1 ±1.8 ° estimated from measured intramolecular distances R_{OD} = 0.970 ± 0.005 Å and R_{DD} = 1.55 ± 0.01Å. Car-Parrinello molecular dynamics [103] simulations show a similar trend. The geometry properties of the water molecule in the gas phase and in the liquid phase are compared in Table 2. [69] The simulations suggest that an average increase of 1 ºin the HOH angle in going from the gas-phase to the condensed phase.

Table 2. Geometrical properties and dipole moments (debye) from Car-Parrinello simulation. Experimental data are given in parentheses.

	HOH ( )	d_{OH}/Å	d_{OO}/Å	Dipole(D)
Monomer	104.4 (104.5)	0.972 (0.957)	-	1.87(1.86)
Liquid	105.5 (106)	0.991 (0.970)	2.78 (2.80)	2.95

Polarization effect has been widely believed in the liquid environment to attribute to the dipole moment enhancement from the gas phase to the condensed phases. To understand the origin of this dipole moment enhancement, Kemp and Gordon [104] used the EFP method to predict

the dipole moments for water clusters. They argued that the enhancement of the dipole moment of a water molecule in the presence of other water molecules arises primarily from decreases in the angles between the lone pair dipole vectors. This angle decrement arises in turn from the increased participation of these lone pairs in hydrogen bonds when a water molecule is surrounded by other waters.

These findings suggest a potential issue involved in the water models that assume the rigid-body water molecular structures. Xantheas argued that their flexible model implementation reproduced the increase in the bend angle in water clusters, liquid water, and ice from its gas phase monomer value. [105]

It has sometimes been argued that flexible water models are not superior to their rigid counterparts and fair judgments are even harder to make due to the need to take the nuclear quantum effect into account. [40] Results from Car–Parrinello simulations show that structural properties and diffusion coefficients obtained with a rigid model are in better agreement with experiment than those determined with fully flexible simulations. [106] Using a rigid model allows one to use larger time steps and thereafter facilitates larger scale simulations. Though rigid body water models seem to have an advantage over their flexible counterpart, this conclusion is arguable. The flexible water models at the current stage certainly were not as advanced as their rigid counterpart. Flexible molecules provide additional challenges to force field development, due to the subtle yet extremely important balance between the intra- and inter-molecular forces. More accurate treatment requires the atomic charges assigned to the sites respond to the geometrical change.[107] Convincing work requires using a reasonable flexible water models and allowing satisfactory treatment of nuclear quantum effects.

The major challenge and also pretty much the objective underlying the flexible water force field development is to accurately reproduce the vibrational features of many kinds of water clusters and condensed phases, especially at the 3000–4000 cm^{-1} range. Important vibrational features include the frequency shift of the vibrations due to the formation of hydrogen bonds, the change in the vibrational intensities associated with the hydrogen bonding, the change of the water bending and stretching regions associated with excess electron attachment [12] and proton transfer[108].

It was reported that the intramolecular frequencies of the O-H stretch modes in water undergo substantial redshifts in the condensed phases, a redshift of 505 cm^{-1} in ice. [109] In nineties of the last century, Reimers,[110] Toukan [111] and Ferguson [112] all proposed that the redshifted stretch results from an anharmonic intramolecular surface. Dang suggest that introduction of a 'Urey-Bradley' term quadratic in the intramolecular H-H separation is required. [113] Although these models reproduced some experimentally observed redshift for liquid water; their models, most being nonpolarizable model, were not designed to be accurate for cluster calculations. In addition, the parameterization used by these models involved intricate error-canceling, the question is still unsolved with regard to how intermolecular and intramolecular interactions participate in the process.

Another experimental observation is the enormous 25-fold increase of the integrated IR intensity in the OH stretch mode in ice compared to that of the gas-phase monomer. [114] Most water models, including many polarizable models, predict almost no increase in the intensities when going to the condensed phase. The OH stretch frequency in water is sensitive to both the local hydrogen bonding environment and the polarization field generated by the liquid.[115]

The general strategy for modeling internal flexibility is to choose quadratic forms for bond stretching and angle bending, and to include anharmonicity by introducing cubic corrections, cross terms between stretching and bending, and additional terms such as Urey-Bradley potential. The AMOEBA water model [63], for instance, uses

$$E_{intra} = E_{bond} + E_{angle} + E_{UB} \qquad (8)$$

The functional forms for bond stretching and angle bending were taken from the MM3 force field and include anharmonicity.

$$E_{bond} = k_1(r - r_0)^2 + k_2(r - r_0)^3 + k_3(r - r_0)^4 \qquad (9)$$

$$E_{angle} = c_1(\theta - \theta_0)^2 + c_2(\theta - \theta_0)^3 + c_3(\theta - \theta_0)^3 + c_4(\theta - \theta_0)^4 + c_5(\theta - \theta_0)^5 \qquad (10)$$

Urey-Bradley function was chosen to model the coupling between stretching and bending modes.

$$E_{Urey-Bradley} = l(d - d_0)^2, \qquad (11)$$

where d is the distance between the two hydrogen atoms of a water molecule.

The major issue with this approach is that the intramolecular charge rearrangement is missing, i.e., the partial charges on the atomic sites are fixed and not allowed to change in response to the structural distortion. This leads to a linear dipole moment surface as discussed by Burnham et al. [114]

2.6 CURRENT STATUS OF THE FLEXIBLE WATER MODEL

The TTM2-F model, developed by Burnham and Xantheas [116] was the first water model using the Partridge-Schwenke potential energy surface (PS-PES) of water to calculate the

intramolecular potential. It also made the use of effective charges that were obtained from the dipole moment surface (PS-DMS) fit by the same authors. Before that, the partial charges in flexible models were kept fixed and did not respond to the geometrical change. These authors found that the use of the prefit nonlinear PS-DMS is essential in modeling the increase in the internal HOH bend angle with cluster size, while using a linear DMS in flexible models for water does not predict this angle increment. When water geometries change, the partial charges, obtained by fitting to a distorted molecular electrostatic potential certainly will change accordingly.

The TTM2-F model and its close variant TTM-2.1F [117] predict an increase in the bending angle as the size of clusters grows. The model, however, fails to predict the redshift in the OH stretching frequencies. The authors also created a test model, TTM2-F(L), in exactly the same way as the TTM2-F model except using fixed partial charges. In order to model the insufficiency of the "linear DMS", TTH2-F(L), has surprisingly partially reproduced the redshift of the characteristic OH stretch. The results were counterintuitive, regarding that the TTM2-F model certainly has a more accurate description of the intramolecular potential energy surface over TTM2-F(L). Later TTM2-F has been modified in order to address this problem. Two important extensions, the TTM3-F model and the TTM4-F model, are discussed below.

The TTM3-F model of Fanourgakis and Xantheas, [118] yields appreciable redshifts of the O-H vibrational stretches for both water clusters and liquid water. They modified the PS-DMS charges ($q_{DMS}^{H_1}$ and $q_{DMS}^{H_2}$) so that the corresponding charges on the hydrogen atom ($q_{DMS'}^{H_1}$ and $q_{DMS'}^{H_2}$) increase with increasing O–H separations

$$q_{DMS'}^{H_1} = q_{DMS}^{H_1} + d_r\left(r_{OH_1} - r_e\right) + d_\theta\left(\theta - \theta_e\right) \qquad (12)$$

$$q_{DMS'}^{H_2} = q_{DMS}^{H_2} + d_r\left(r_{OH_2} - r_e\right) + d_\theta\left(\theta - \theta_e\right) \qquad (13)$$

r_e and θ_e are the equilibrium monomer bond length and bend angle, and d_r *and* d_θ are parameters to be determined during the parameterization procedure. In contrast, the PS-DMS charges on the hydrogen atoms decrease with the increasing O-H separation. The authors claimed that it necessary to asymptotically dissociate the O-H bond into charged species (H^+ and OH^-) at large O-H separations in condensed environments. Other changes include reducing the number of polarizable sites from three in TTM2-F to one on M-site and using the Buckingham exponential-six potential to describe the exchange-repulsion and dispersion.

Despite the impressive success of TTM3-F in predicting the OH stretch redshifts, the model suffers from its use of a single polarizable site. Moreover, the model performs poorly in term of vibrational intensity in water clusters. Burnham demonstrate that the over-rigidity of the OH stretch and the underestimation of intensity in TTM2-F, are connected to the failure of existing models to reproduce the correct monomer polarizability surface. In TTM4-F model, [119] he proposed a modified charge density scheme in the polarization term. This change leads to an improved description of the water molecular polarizability and its derivatives, and thereafter a more reasonable vibrational intensity for the OH stretches. Burnham attributed the improvement in the vibrational spectroscopy to this new charge density scheme used in the polarization interaction term. The model models exchange-repulsion and dispersion interaction using a polynomial with six R^{-n} terms.

$$E_{vdw} = \sum_{i<j}\left[\frac{a_6}{r_{ij}^6} + \frac{a_8}{r_{ij}^8} + \frac{a_{10}}{r_{ij}^{10}} + \frac{a_{12}}{r_{ij}^{12}} + \frac{a_{14}}{r_{ij}^{14}} + \frac{a_{16}}{r_{ij}^{16}}\right] \qquad (14)$$

For liquid water the TTM4-F model has predicted the vibrational OH redshift and the calculated intensities are in good agreement with measured spectrum.

The vibrational analysis has a complicated relationship to the total potential energy function and its components, and the parameters for each energy term vary when the different properties and structures are introduced into the fitting. Through the TTM flexible water models and many others' work[120,121] we have achieved a new level of understanding on the vibrational redshift associated with the hydrogen bonding. It, however, still remains mysterious in the framework of force fields how this is connected to the model development: the potential function expressions and the parameterizations.

2.7 POLARIZABLE FLEXIBLE WATER MODEL AND EXCESS ELECTRON-WATER INTERACTION POTENTIAL

From the simple nonpolarizable point-charge models to sophisticated polarizable models based on Gaussian charge distributions or higher-order multipoles, there are a wide range of water models available. Most of these models, however, are intentionally designed for MD or MC simulations of liquid water, which means they belongs to the Class I force fields or their polarizable counterparts and are not designed to produce satisfactory conformational analysis of water clusters. Recently several models have been built up from energy decomposition and accurate *ab initio* quantum mechanics calculations, but no detailed test on water clusters have been reported.

To satisfactorily describe excess electron-water interactions, the neutral water force field need to

1). Include polarization interactions, so it can adjust charge densities in accordance to external fields from other water molecules and the excess electron.

2). generate accurate dipole moment on each water molecule. In the electron-water potential, the excess electron interacts with the static dipole moments (point charges) and the induced dipole moments on each water molecules. As mentioned earlier, polarizable models yield much more accurate dipole moment than nonpolarizable models. The point charges are predetermined and do not vary much among models, induced dipole moments, however, are influenced by the polarization scheme.

3). reasonably calculate the relatively energies of water clusters. Most water anion clusters have structures greatly distorted due to the excess electron. The work conducted in our group showed that most available polarizable models do not perform very well for these anion structures. The DPP model has been satisfactorily used in group for most of the electron-water interaction calculations. The recently published DPP2-R model, however, show improved results relative to the DPP, by adding charge penetration and charge transfer terms to the potential energy function.

4). Vibrational spectroscopy is one of the most powerful tools to study the water cluster anions. The research community has come to an agreement that the AA type (two hydrogen atoms from the same water pointing towards the external electron cloud) clusters are the most important species observed in the spectroscopy studies of the smaller clusters. When the electron polarizes the O-H stretch, a great appreciation of the vibrational intensities of the O-H stretch will be observed. Getting reasonable intensities has been a major challenge for force fields and it is one of the objectives of the present work.

The model presented in this work, denoted as DPP2-F model, is a polarizable and flexible water model, based on the DPP2-R potential function and many observations from the DPP2-R and DPP models. The static charge distribution of each water molecule is represented by three point charges, two on hydrogen atoms and one on the M-site. The water molecule assumes a flexible geometry, with the equilibrium O-H distance at 0.9584Å and bond angle at 104.52°. There are three polarizable sites, two on hydrogen and one on oxygen and mutual polarization is achieved through the Thole's polarization scheme.

3.0 THEORY AND INPLEMENTATION

3.1 DPP2-F MODEL POTENTIAL ENERGY FUNCTION

The interaction potential energy function of the DPP2-F water model, is formulated as

$$E_{total} = E_{int} + E_{es} + E_{pol} + E_{ct} + E_{ex-rep} + E_{disp} \qquad (15)$$

with intramolecular distortion contribution E_{int} and six intermolecular contributions, electrostatic (E_{es}), polarization (E_{pol}), charge transfer (E_{ct}), exchange-repulsion ($E_{ex\text{-}rep}$),and dispersion (E_{disp}) contributions.

A short description to each contribution is given as follows: [122]

1). Intramolecular contribution is caused by the geometry distortion from the equilibrium structures.

2). The electrostatic term is the classical interaction between the charge distributions of the molecules. In the model, point-charges were used to represent the charge distribution.

3). Induction arises from the distortion of the charge density of one molecule in response to the polarization perturbation from other neighboring molecules.

4). Charge transfer is the gain in the energy that results from the transfer of partial electrons from an electron-rich centre, towards the virtual orbital of neighboring electron-deficient ones.

5). Exchange-repulsion term arises from the overlap of the charge distributions as a consequence of the Pauli principle, which forbids two electrons with the same spin being at the same point in space simultaneously.

6). The dispersion term is a nonclassical interaction arising from correlated fluctuations of the electrons in the interacting molecules.

3.2 SAPT AND ENERGY DECOMPOSITION

In SAPT, [22] the antisymmetrized product of monomer wavefunctions $A\Phi_{AB} = A\Phi_A\Phi_B$ is used for the zeroth-order approximation to the dimer wavefunction. The A here represents the intermolecular antisymmetrization operator. Energy terms can be defined at each order of energy corrections by applying this type of wavefunction. SAPT represents the interaction energy as a sum of terms with a well-defined physical interpretation. It provides a clear physical insight into the nature of intermolecular interaction mechanism. Since all the terms computed by SAPT contribute directly to the interaction energy, the method is free from the basis set superposition error (BSSE). [123]

The total interaction energy is described as interaction energy at the Hatree-Fock (HF) level, E_{inter}^{HF} , plus a higher-order correlation correction E_{SAPT}^{corr}. [40] E_{inter}^{HF} is counterpoise corrected supermolecular HF interaction energy and is given as:

$$E_{inter}^{HF} = E_{elst}^{(10)} + E_{exch}^{(10)} + E_{ind,r}^{(20)} + E_{exch-ind,r}^{(20)} + \delta_{inter}^{HF} \qquad (16)$$

$E_{elst}^{(10)}$ and $E_{exch}^{(10)}$ are first-order electrostatic interaction energy and its corresponding exchange contribution. $E_{ind,r}^{(20)}$ and $E_{exch-ind,r}^{(20)}$ are the second-order induction energy and the corresponding exchange contribution. The first four terms belong to intermolecular SAPT contributions at the Hartree–Fock level and their sum is the SAPT HF interaction energy ($E_{SAPT,inter}^{HF}$). The δ_{inter}^{HF} term recovers the difference between the E_{inter}^{HF} and $E_{SAPT,inter}^{HF}$.

The SAPT correlation energy contributions, E_{SAPT}^{corr} , is computed as

$$E_{SAPT}^{corr} = \varepsilon_{elst,r}^{(1)}(3) + \varepsilon_{exch}^{(1)}(CCSD) + {}^{t}E_{ind}^{(22)} + {}^{t}E_{exch-ind}^{(22)} + E_{disp}^{(20)} + \varepsilon_{disp}^{(2)}(2) + E_{exch-disp}^{(20)} \qquad (17)$$

$\varepsilon_{elst,r}^{(1)}(3)$ is the correlation correction to the electrostatic interaction energy. This contribution is corrected up to the third order in the intramonomer correlation potential and includes orbital relaxation. $E_{each}^{(1)}(CCSD)$ is the correlation correction to the first-order exchange interaction energy. It is determined with the converged coupled-cluster amplitudes for the monomer. ${}^{t}E_{ind}^{(22)}$ and ${}^{t}E_{exch-ind}^{(22)}$ are the 'true' correlation corrections to the second-order induction and exchange-induction energies. The second-order dispersion interaction energy contribution without orbital relaxation and its exchange counterpart are abbreviated as $E_{disp}^{(20)}$ and $E_{exch-disp}^{(20)}$ respectively. $\varepsilon_{disp}^{(2)}(2)$ is the second-order intramonomer electron correlation correction to the second-order dispersion energy.

These energy components are grouped into electrostatic, exchange-repulsion, induction and dispersion contributions:

$$E_{es}^{SAPT} = E_{elst}^{(10)} + E_{elst,r}^{(12)} + E_{elst,r}^{(13)} \qquad (18)$$

$$E_{ex-rep}^{SAPT} = E_{exch}^{(10)} + \varepsilon_{exch}^{(1)}\left(CCSD\right) \qquad (19)$$

$$E_{ind}^{SAPT} = E_{ind,r}^{(20)} + {}^{t}E_{ind}^{(22)} + E_{exch-ind,r}^{(20)} + {}^{t}E_{exch-ind}^{(22)} + \delta_{\text{int}}^{HF} \qquad (20)$$

$$E_{disp}^{SAPT} = E_{disp}^{(20)} + \varepsilon_{disp}^{(2)}\left(2\right) + E_{exch-disp}^{(20)} \qquad (21)$$

The sum of these four terms gives SAPT intermolecular energy:

$$E_{inter}^{SAPT} = E_{es}^{SAPT} + E_{ex-rep}^{SAPT} + E_{ind}^{SAPT} + E_{disp}^{SAPT} \qquad (22)$$

The SAPT energy partition scheme provides a straightforward way to constructing the DPP2-F water models term-by-term. The four main energy contributions are used in the parameterization as the reference energies and to evaluate the performance of the model as well.

3.3 PARTRIDGE-SCHWENKE INTRAMOLECULAR ENERGY

Intramolecular energy (E_{int}) due to internal geometry distortion of water molecule is calculated by the Partridge-Schwenke potential energy surface (PS-PES). [124] The monomer PES was calculated using the cc-pV5Z basis set augmented with a diffuse s, p, and d functions on oxygen and diffuse s and p functions on hydrogen and was fit to a large number of points as well as possible and empirically adjusted to improve the agreement between the computed vibrational line positions and those from database.

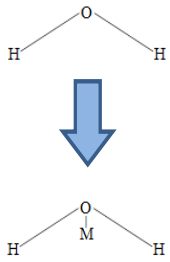

$$q_{DMS}^{H_1}, q_{DMS}^{H_2}, q_{DMS}^{O} \qquad q_{H_1} = q_{DMS}^{H_1} - \frac{\gamma}{2(1-\gamma)} q_{DMS}^{O}$$

$$q_{H_2} = q_{DMS}^{H_2} - \frac{\gamma}{2(1-\gamma)} q_{DMS}^{O}$$

$$q_{H_1}, q_{H_2}, q_M \qquad q_M = -(q_{H_1} + q_{H_2}) = \frac{q_{DMS}^{O}}{1-\gamma}$$

$$r_M = r_O + \frac{\gamma}{2}(r_{H_1O} + r_{H_2O})$$

Figure 2. The scheme to calculate the DPP2-F point charges on hydrogen atoms and the *M*-site using PS-DMS. γ is the parameter used to decide the location of *M*-site. The approach has been employed by the TTM-series flexible models.

The authors also presented a dipole-moment surface (DMS) as

$$\mu(r_1, r_2, \theta) = q(r_1, r_2, \theta) r_{H_1O} + q(r_2, r_1, \theta) r_{H_2O} \qquad (23)$$

in terms of internal coordinates. The atomic charges $q(r_1, r_2, \theta)$ on hydrogen and oxygen atoms are geometry dependent and were fit in terms of polynomials to yield an accurate dipole moment surface. Following the approach reported by Burnham and Xantheas, [116] We take atomic charges $q_{DMS}^{H_1}$, $q_{DMS}^{H_2}$ and q_{DMS}^{O} from PS-DMS and construct the point charges q_{H_1}, q_{H_2} and q_M on hydrogen atoms and the *M*-site for any given water configuration. The charge transformation is given in Figure 2 and it conserves the total dipole moment of the water molecules.

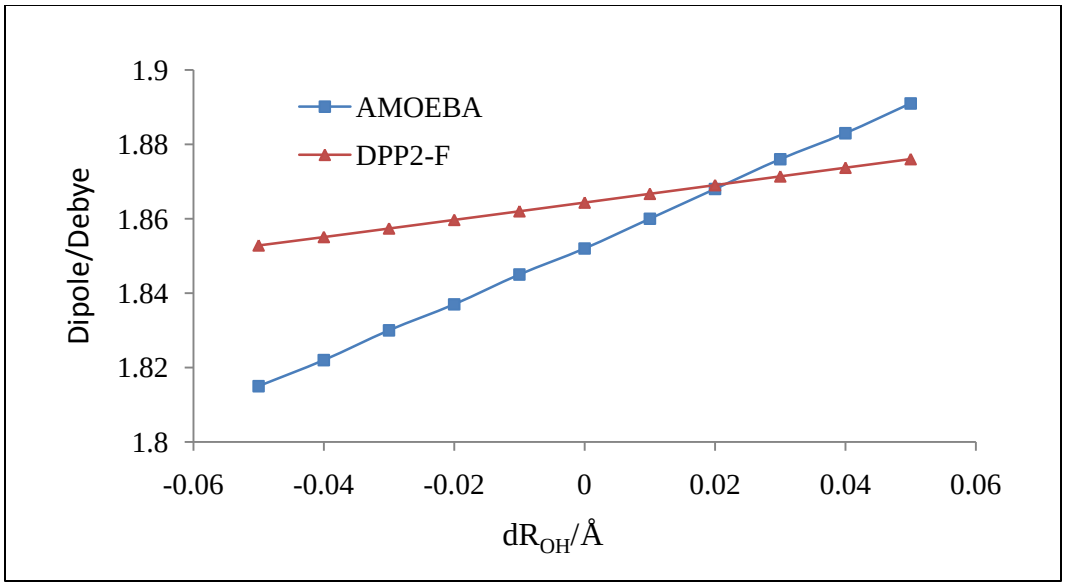

Figure 3. Comparison of water dipole moments computed by the DPP2-F model and the AMOEBA water model. dR_{OH} is the displacement of one hydrogen atom relative to its equilibrium position.

In Figure 3, the DPP2-F and AMOEBA model dipole moments of water molecule are plotted together. This shows how the linear (AMOEBA model) and nonlinear (DPP2-F) dipole moment surface affect the dipoles on the monomer OH stretch. Similar to other early flexible water models, the AMOEBA model does not allow the atomic multipoles to vary as the water geometry distorts, and as a result, the slope of the AMOEBA dipole plot is too steep. As shown by Xantheas, the monomer OH intensity calculated by the AMOEBA is even more appreciable than MP2. [118]

Table 3 compares the effective point charges of water dimer minimum given by the PS-DMS (the charges were fit to give the right dipole moments) on each atom with the fixed charges used in the rigid DPP2-R/DPP/TTM2-R models. The increase of the positive charge on H_{11} (forming the H-bond with O_2) and the decrease on H_{12} (the other hydrogen on the same water)

described by the DPP2-F model provide a more realistic picture of the water cluster electrostatic interactions.

Table 3. Comparison of the partial charges (*e*) on the atomic sites of the water dimer in the DPP2-F and DPP2-R models. (See Figure 4 for the structure)

Atom number	O_2	H_{21}	H_{22}	O_1	H_{12}	H_{11}
Rigid/DPP2-R	-0.6620	0.3310	0.3310	-0.6620	0.3310	0.3310
Flexible/DPP2-F	-0.6637	0.3318	0.3318	-0.6596	0.3308	0.3289

3.4 ELECTROSTATIC AND CHARGE PENETRATION

The damping scheme reported by Freitag et al. in the EFP approach was employed to calculate the charge penetration energy in the DPP2-F model. [90] Each type of point charges has an associated damping coefficient a^{pen}. The charge penetration energy is given by:

$$E_{es}^{pen} = -\frac{1}{2R_{AB}}\left[\begin{array}{l} q_A(q_B+2Z_B)e^{-a_A^{pen}R_{AB}} + q_B(q_A+2Z_A)e^{-a_B^{pen}R_{AB}} \\ +\dfrac{q_Aq_B(a_A^{pen2}+a_B^{pen2})}{a_A^{pen2}-a_B^{pen2}}(e^{-a_B^{pen}R_{AB}} - e^{-a_A^{pen}R_{AB}}) \end{array}\right] \qquad a_A^{pen} \neq a_B^{pen} \qquad (24)$$

when atom A and B are not of the same type, and

$$E_{es}^{pen} = -\frac{1}{R_{AB}}\left[q_Aq_B(1+\frac{a_A^{pe}R_{AB}}{2}) + q_AZ_B + q_BZ_A\right]e^{-a_A^{pen}R_{AB}} \qquad a_A^{pen} = a_B^{pen} \qquad (25)$$

when atom A and B are of the same type. Z_A and Z_B are the net charges on the nuclear sites and are given by the nuclear charge minus the assigned model partial charges. For the DPP2-F model, there are two coefficients, a_H^{pen} and a_M^{pen}, associated with the charges on hydrogen atoms

and the *M*-site. The electrostatic energy is then augmented with the charge penetration energy (unit in *kcal/mol*)

$$E_{es} = \sum_{i<j} E_{es,ij}^{pen} + k\sum_{i<j} \frac{q_i q_j}{r_{ij}} \qquad (26)$$

k is the conversion factor from atomic unit to *kcal/mol*. The DPP2 rigid model [21] uses Piquemal's damping scheme [92]. The approach is also investigated in the current work. In this approach, point-charge electrostatics is given by

$$E_{es} = k\sum_{i,j} \frac{q_i^* q_j^*}{r_{ij}} \qquad (27)$$

where q_i^* and q_j^* are damped atomic charges (*e*) computed by the following expression and are dependent on the distance between atom i and *j*.

$$q_i^* = 2q_i - \left(Z_i - \left(Z_i - q_i\right)\left(1 - \exp\left(\frac{\lambda_{AB} r_{ij}}{\frac{Z_i - q_i}{Z_i}}\right)\right)\right) \qquad (28)$$

Z_i is the number of valence electrons of atom *I*. λ_{AB} is treated as a transferable parameter, adjusted on the nature of the two interacting molecules A and B, and is kept constant for all calculations. Same as the DPP2 rigid model, only one parameter, λ, need be determined.

The two parameters, a_H^{pen} and a_M^{pen} in the first approach, and the one parameter λ, in the second approach were obtained by fitting the model electrostatic energy to SAPT electrostatic energies of water structures generated by varying the O-O distances. For convenience, we refer the first as EFP-CP (EFP-charge penetration) and second one as MC-CP (modified charge-charge penetration).

3.5 POLARIZATION

The polarization energy is defined as

$$E_{pol} = -\frac{1}{2}\sum_i \mu_i E_i \qquad (29)$$

where μ_i, the induced dipole moment at the polarizable site i, is given by

$$\mu_i = \alpha_i \left(E_i - \sum_{j \neq i}^{N} T_{ij} \cdot \mu_j \right) \qquad (30)$$

and is computed in iterative fashion. α_i denotes the isotropic point polarizability of atom i, T_{ij} is the dipole–dipole interaction tensor:

$$T_{ij} = \frac{1}{r_{ij}^3} I - \frac{3}{r_{ij}^5} \begin{pmatrix} x^2 & xy & xz \\ yx & y^2 & yz \\ zx & zy & z^2 \end{pmatrix} \qquad (31)$$

where I is the identity matrix and x, y and z are Cartesian components along the vector between atoms i and j at distance r_{ij}. E_i is the electrostatic field on atom i due to partial charges (or higher-order multipoles) and induced dipoles.

In point dipoles interactions, when atoms come closer than a certain short distance limit, the molecular polarizability can diverge. This is usually referred to as polarization catastrophe and is unphysical in reality. [50] Thole introduced a modification scheme in which one of the point dipoles in each pair of dipole interaction is replaced by a smeared charge distribution.[125] As a result, the dipole interaction energy approaches a finite value instead of becoming infinite as the separation distance approaches zero. Seven charge distribution functions were tested, and for

each of the models, a transferable isotropic polarizability for each chemical element was derived by fitting to experimental polarizabilities of a set of molecules.

The exponential form of charge distribution considered by Thole is

$$\rho(r) = \frac{3a}{4\pi}\exp\left(-au^3\right) \qquad (32)$$

in which $A = \left(\alpha_i \alpha_j\right)^{1/6}$, $u = r/A$. It has been the most popular form and used in the TTM-series (TTM2-R(F), TTM3-F), and AMOEBA models, despite the fact that it was not the one that yielded the smallest fitting errors in Thole's study.

Thus-modified matrix elements of the multipole interaction *T* matrix are derived by differentiating inverse distances between sites i and j:

$$T_{ij} = \frac{\rho\left(r_{ij}\right)}{r_{ij}}, \qquad T_{ij}^{\alpha} = \nabla_{\alpha} T_{ij}, \qquad T_{ij}^{\alpha\beta} = \nabla_{\alpha} T_{ij}^{\beta} \qquad \ldots \qquad (33)$$

(α, β,…= 1, 2, 3, ...correspond to x, y and z Cartesian coordinates)

$$T_{ij}^{\alpha,D} = f_3\left(\alpha_{CD}\right)\frac{r_{ij}^{\alpha}}{r_{ij}^3}, \qquad (34)$$

$$T_{ij}^{\alpha\beta,D} = f_3\left(\alpha_{CD}\right)\frac{1}{r_{ij}^3} I - f_5\left(\alpha_{DD}\right)\frac{3}{r_{ij}^5}\begin{pmatrix} x^2 & xy & xz \\ yx & y^2 & yz \\ zx & zy & z^2 \end{pmatrix} \qquad (35)$$

$f_3\left(\alpha_{CD}\right)$ and $f_5\left(\alpha_{DD}\right)$ are damping functions with respect to the charge-dipole and dipole-dipole interactions.

Recently Burnham presented a modified exponential charge distribution expression as

$$\rho(r)^{m=4} = \frac{au}{\pi}\exp\left(-au^4\right) \qquad (36)$$

He argued that an increase in the power exponent of the charge distribution from m=3 used by Thole to *m* =4, improved equilibrium monomer polarizability and the first order changes in the polarizability as a function of nuclear displacements. [119] This modified scheme has been used in the TTM4-F and POLAR [126] models, and lead to improved infrared intensities for hydrogen-bonded OH stretch vibrations. We use the modified scheme in DPP2-F, but also performed comparison of these two charge density forms in terms of quality of reproducing the molecular polarizabilities of water monomer and related vibrational spectroscopy of water clusters.

Table 4. Comparison of the two induced dipole damping schemes. The original exponential form was presented by Thole in 1981. [50]

	Original exponential form	Modified exponential form
Charge density	$\rho(r)^{m=3} = \frac{3a}{4\pi}\exp(-au^3)$	$\rho(r)^{m=4} = \frac{au}{\pi}\exp(-au^4)$
$f_3(a)$	$f_3(a) = 1-\exp(-au^3)$	$f_3(a) = 1-\exp(-au^4)$
$f_5(a)$	$f_5(a) = 1-\left[1+au^3\right]\exp(-au^3)$	$f_5(a) = 1-\left[1+4au^4/3\right]\exp(-au^4)$
Representative models	Thole's, TTM2-R(F), DPP, DPP2-R, AMOEBA	TTM4-F, POLAR, DPP2-F

Atomic polarizabilities associated with the polarizable sites (on the oxygen and hydrogen atoms) are described in term of simple linear function of the point charges on each site as below:

$$\alpha_O = \alpha_M = \alpha_M^0 + g_m(q_M - q_M^0) \qquad (37)$$

$$\alpha_H = \alpha_H^0 + g_h(q_H - q_H^0) \qquad (38)$$

α_H^0 and α_H^0 are equilibrium atomic polarizabilities for the equilibrium Partridge-Schwenke water molecule. To determine these parameters, we started from the equilibrium configuration and chose a coordinate system with the *y* axis pointing out of the plane of the molecule, the *z* axis along the molecular bisection, and the *x* axis perpendicular to both *y* and *z* and in the molecular plane. By varying O-H separations (in Å) at $r_{OH}^0 - 0.05, r_{OH}^0$, $r_{OH}^0 + 0.05$ and $r_{OH}^0 + 0.1$, and HOH angles (in degree) at $\theta_{HOH}^0 - 2, \theta_{HOH}^0, \theta_{HOH}^0 + 2, \theta_{HOH}^0 + 4$, we created sixty four structures and computed their MP2 polarizability tensors (6 components). To compute the model molecular polarizability tensor, external electric fields on X, Y and Z directions were applied and the numerical derivatives of induced dipole with respect to the electric fields were then calculated. The polarizability tensors were then diagonalized using Jacobi diagonalization method to give isotropic molecular polarizabilities.

The five parameters, the equilibrium atomic polarizabilities (α_O^0, α_H^0), the coefficients (g_h, g_m) and the intramolecular dipole-dipole damping factor (α_{DD}^{intra}), were simultaneously determined by matching the model water molecular polarizability tensors to their MP2 values. The charge-dipole damping factor α_{CD}^{inter} and the intermolecular dipole-dipole damping factor α_{DD}^{inter} appear in intermolecular polarizations of water dimers. Their values would then be obtained by fitting the model dipole moments of a series of water dimers to MP2 dipoles of the same structures.

3.6 CHARGE TRANSFER

The charge transfer energy is computed between oxygen and hydrogen atoms from different water molecules using Stone's attractive exponential function. [73]

$$E_{ct} = a_{ct} \sum_{i<j} \exp(-b_{ct} r_{O_i H_j}) \qquad (39)$$

The parameters a_{ct} and b_{ct} are obtained by fitting the energies to the difference between the SAPT induction and the DPP2-F polarization energy.

3.7 DISPERSION

The dispersion interaction between two water molecules is given as

$$E_{disp} = \frac{c_{OO}}{r_{OO}^6} f\left(\delta_{OO} r_{OO}\right) + \sum_{i<j} \frac{c_{OH}}{r_{O_i H_j}^6} f\left(\delta_{OH} r_{O_i H_j}\right) + \sum_{i<j} \frac{c_{HH}}{r_{H_i H_j}^6} f\left(\delta_{HH} r_{H_i H_j}\right) \qquad (40)$$

in which $f(x) = 1 - \exp(-x) \sum_{k=0}^{6} \frac{x^6}{k!}$ is taken from Tang and Toennies. [85] We use the DPP2-R model dispersion term, because it reproduces the SAPT dispersion energy very well. The fitting errors were much smaller compared with other energy terms.

3.8 EXCHANGE-REPULSION

The exchange-repulsion interaction between two water molecules is computed as:

$$E_{ex-rep} = a_{OO}\exp(-b_{OO}r_{OO}) + \sum_{i<j} a'_{OH}\exp(-b_{OH}r_{O_iH_j}) + \sum_{i<j} a_{HH}\exp(-b_{HH}r_{H_iH_j}) \qquad (41)$$

The coefficient of the O-H pair is made charge-dependent by using below expression.

$$a'_{OH} = a^0_{OH} + c(q_{H-DMS} - q^0_{H-DMS}) + d(q_{O-DMS} - q^0_{O-DMS}) \qquad (42)$$

where a^0_{OH} is the coefficient for equilibrium dimer, and q_{O-DMS} and q_{H-DMS} are effective charges given by PS-DMS. The three parameters within α'_{OH} give extra flexibility in the fitting. The eight parameters are determined by fitting to the difference between MP2 total interaction energy and the sum of all other potential model energy terms, including the intramolecular energy.

3.9 TRAINING SET AND FITTING SCHEME

Referring to Figure 4, structures used for the model parameterization and tests include:

Category 1. Water dimers (Cs geometry) with O_1-O_2 distances varying from 2.4 to 5.0 Å, with and without constrained optimizations.

Category 2. Water dimers with varying distance of O-H (O_1-H_{11}) separations from 0.95 to 1.0 Å.

Category 3. Water dimers with O_1–O_2 distances being fixed at 2.81, 2.86, 2.91, and 2.96 Å and "tilt angle", $H_{11}O_1O_2$, varying from 20 °to -10 ºat every 5 º. The "tilt angle" measures the deviation of the donor hydrogen from the O_1—O_2 direction.

Category 4. Smith dimer set [127] of the ten stationary points which were all fully optimized at MP2/aug-cc-pVTZ level. [128] It includes the global minimum, three first-order saddle points and six higher-order saddle points.

Category 5. Water cluster isomers from water trimer up to hexamer. All these clusters were all fully optimized at MP2/ aug-cc-pVDZ level.

Category 6. All water dimers and trimers from Category 5. Note dimers extracted from the ring-type clusters have same water dimers due to symmetry.

Total interaction energies were calculated using density-fitting MP2 method [129] implemented in Molpro [130] and the aug-cc-pV5Z basis set. Dipole moments, molecular polarizabilities, vibrational frequencies and intensities were computed at MP2/aug-cc-pVDZ level using Gaussian 03 program. [131] Energy decompositions through SAPT were conducted on all dimers, using the SAPT-2008 program. [132]

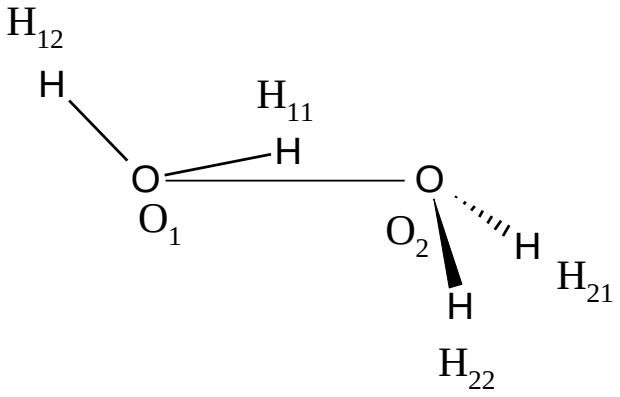

Figure 4. Sketch of the global minimum of water dimer.

Model parameterizations were carried out in the order shown in Table 5, from the top to the bottom. Parameterizations were done by minimizing the objective error functions

$$\chi^2\left(\vec{v}\right)=\sum_{i=1}^{N} w_i\left(E_i^{model}\left(\vec{v}\right)-E_i^{ref}\right)^2 \qquad (43)$$

, $\vec{v}$ is the vector of parameters to be determined and w_i is the weighting factor. Setting ideal weights for different structures and properties can be crucial for the success of the parameterization. E_i^{model} can be energy, gradient, dipole moment, or polarizability, and is calculated by the model. The non-linear least square fitting employed the genetic algorithm (GA). GA is an efficient approach for dealing with the multiple-minimum problem, which makes it an ideal optimization method for the problem of force-field parameterization.[133] GAlib, [134] a C++ generic algorithm library, was combined with the DPP2-F code to do the fitting. The original library was in single precision, so it was converted to double precision for this task. A typical GA optimization set-up uses a population of 500, crossover probability of 0.2, maximum iteration of 1000 and a mutation probability of 0.1.

The parameters of the DPP2-F model are listed in Table 6.

Table 5. The parameterization of the DPP2-F model. The model was fit in the order from the top to the bottom.

Energy term	Reference data	Parameters
E_{es}	E_{es}^{SAPT}	$\alpha_H^{pen}, \alpha_M^{pen}$
E_{pol}	Molecular polarizability	$\alpha_H, \alpha_M, g_M, g_H, \alpha_{DD}^{intra}$
	Dipole moment	$\alpha_{DD}^{inter}, \alpha_{CD}$
E_{ct}	$E_{ind}^{SAPT} - E_{pol}$	a_{ct}, b_{ct}
E_{disp}	E_{disp}^{SAPT}	$c_{OO}, \delta_{OO}, c_{OH}, \delta_{OH}, c_{HH}, \delta_{OH}$
E_{ex-rep}	$E_{total}^{MP2} - E_{intra} - E_{es} - E_{pol} - E_{ct} - E_{disp}$	$a_{OO}, b_{OO}, a_{HH}, b_{HH}, a_{OH}^0, c, d, b_{OH}$

Table 6. Listing of the parameters of the DPP2-F model.

Category	Parameters	Values	Units
Electrostatic	a_H^{pen}	2.1249	$Å^{-1}$
	a_M^{pen}	4.7901	$Å^{-1}$
Polarization	α_O	1.35	$Å^3$
	α_H	0.285	$Å^3$
	g_M	1.3361	-
	g_H	0.57124	-
	a_{DD}^{intra}	0.505	-
	a_{DD}^{inter}	0.0581	-
	a_{CD}	0.389	-
Charge transfer	a_{ct}	-988.344	kcal/mol
	b_{ct}	3.4155	$Å^{-1}$
Dispersion	c_{OO}	-277.21	kcal/mol $Å^6$
	δ_{OO}	31.92	$Å^{-1}$
	c_{HH}	-25.963	kcal/mol $Å^6$
	δ_{HH}	10.984	$Å^{-1}$
	c_{OH}	-131.49	kcal/mol $Å^6$
	δ_{OH}	3.7738	$Å^{-1}$
Exchange repulsion	a_{OO}	3435.23	kcal/mol
	b_{OO}	2.5184	$Å^{-1}$
	a_{HH}	7677.2	kcal/mol
	b_{HH}	3.7877	$Å^{-1}$
	a_{OH}^0	4561.88	kcal/mol

	c	3.27583	kcal/mol
	d	4234.8	kcal/mol
	b_{OH}	3.5953	$Å^{-1}$
Structural	q^0_{O-DMS}	-0.661984	-
	q^0_{H-DMS}	0.330992	-

4.0 MODEL TESTS AND DISCUSSIONS

4.1 ELECTROSTATIC INTERACTION ENERGY AND THE CHARGE PENETRATION EFFECT

The point-charge representation based on a finite-number of partial charges surfers from two limitations, as discussed in previous text. One is the short-range effect: when two molecules are close enough, their charge densities can overlap, and the shielding of the nuclear charge of each molecule by its own electron density decreases. This leads to an increased attraction, which is referred to as charge penetration energy. Without taking the charge penetration into account, conventional point-charge electrostatic interaction tends to underestimate the electrostatic interaction. As charge penetration is a short-range effect and is more pronounced when molecules are close to each other, this underestimation is more severe at short molecular distances. The other limitation is associated with the insufficiency of using a small number of point charges for accurate description of the molecular charge distribution or dipole moment surfaces. Error arises in the water molecules, so it may occur when molecules are close to each other, but can also cause trouble when the molecules assume certain configurations. Using more charge sites and higher-order multipole expansion are common remedies, but the benefits come at the expense of more complex implementation and computational cost.

The MP2 water dimer minimum has an O-O distance (R_{OO}) of 2.9 Å, but in ice and liquid water and even in water clusters, water molecules experience short R_{OO} to 2.7 Å. We have shown that water dimer optimized with many non-polarizable water models display R_{OO} at 2.7 Å, shorter than those from polarizable water models. The short-range trouble was partially solved by the error-canceling among the model parameterizations, which is usually absorbed by the nonbonded repulsion interaction part.

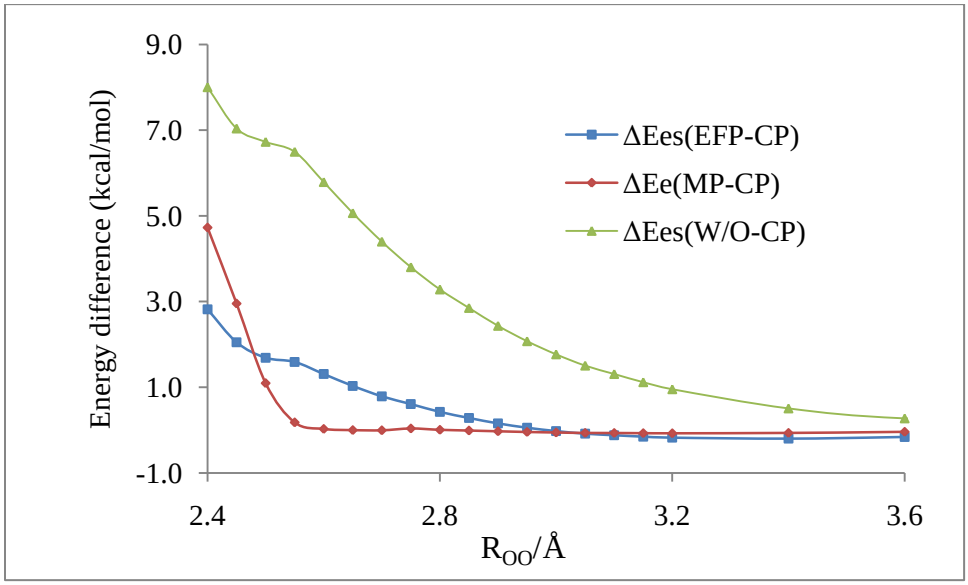

Figure 5. Energy difference between DPP2-F and SAPT electrostatic energies for water dimers with varying OO distances (R_{OO}). EFT-CP refers to Freitag-Gordon-Jensen EFP charge penetration scheme, whereas MP-CP refers to the Piquemal's modified-charge charge penetration method. Water dimers were optimized by fixing the O-O distances.

Figures 5 to 8 compare the electrostatic energies of point-charge electrostatic term augmented with and without charge penetration for different types of water clusters. The electrostatic energy of the DPP2-F model, E_{es}, contains the contribution from the point charge ($E_{es}^{point-charge}$) and charge penetration ($E_{es}^{charge-penetration}$),

$$E_{es} = E_{es}^{point-charge} + E_{es}^{charge-penetration} \qquad (44)$$

$E_{es}^{point-charge} = k\sum_{i,j}\frac{q_i q_j}{r_{ij}}$ is the point-charge electrostatic energy, as seen in the DPP and TTM2-R(F), though the values of the charges vary in response to the geometrical changes.

The difference between SAPT and $E_{es}^{point-charge}$ is denoted as $\Delta E_{es}\left(W/O-CP\right)$:

$$\Delta E_{es}\left(W/O-CP\right) = E_{es}^{point\text{-}charge} - E_{es}^{SAPT} \qquad (45)$$

We assume that $\Delta E_{elec}\left(W/O-CP\right)$ represents charge penetration effect only, although it obviously includes the non-charge penetration combination not described by the three point-charge model. Indeed, recent work from our group has shown that models with seven or nine point charges significantly reduce the $\Delta E_{es}\left(W/O-CP\right)$.

Figure 5 presents the electrostatic energies of the two charge penetration methods as a function of the R_{OO} in the water dimer. The penetration energy increases from 0.1 to 8 kcal/mol as R_{OO} shortens from 4.0 Å to 2.4 Å. The electrostatic energies calculated through the MP-CP approach are in excellent agreement with the SAPT electrostatic as R_{OO} are greater than 2.6 Å. The error, however, increases above 1 kcal/mol as the R_{OO} approaches 2.5 Å, and increases sharply to about 4.8 kcal/mol when R_{OO} is as short as 2.4 Å. The EFP-CP scheme is adopted in the DPP2-F model. It also systematically recovers partial charge penetration energies. The errors are about 0.19 kcal/mol for dimer minimum (R_{OO} at 2.91 Å) and 1.4 kcal/mol for the R_{OO} at 2.6 Å, both of which are greater than those close-to-zero errors using MP-CP. For the two hundred dimer structures we studied, the EFP-MP method gives a standard deviation of the electrostatic energy error of 0.573 kcal/mol, compared with 0.596 kcal/mol by the MP-CP method. If the

structures R_{OO} shorter than 2.6 Å are excluded, the standard deviation drops to 0.469 kcal/mol, about 40 percents greater than the 0.327 kcal/mol from the MP-CP scheme.

The DPP2-F model is still not sufficient to reproduce the charge penetration contribution for water molecules with O-O distances shorter than 2.6 Å. For such dimers, the DPP2-F electrostatic energies consistently deviate from SAPT electrostatic to the positive side, but less than 1 kcal/mol when O-O distances are greater than 2.65 Å. Without the charge penetration effect, however, the deviation is over 5 kcal/mol. At short separations the approximation of bare molecular charges at both the atomic and off-atomic sites with delta function distributions is no longer realistic. [112]

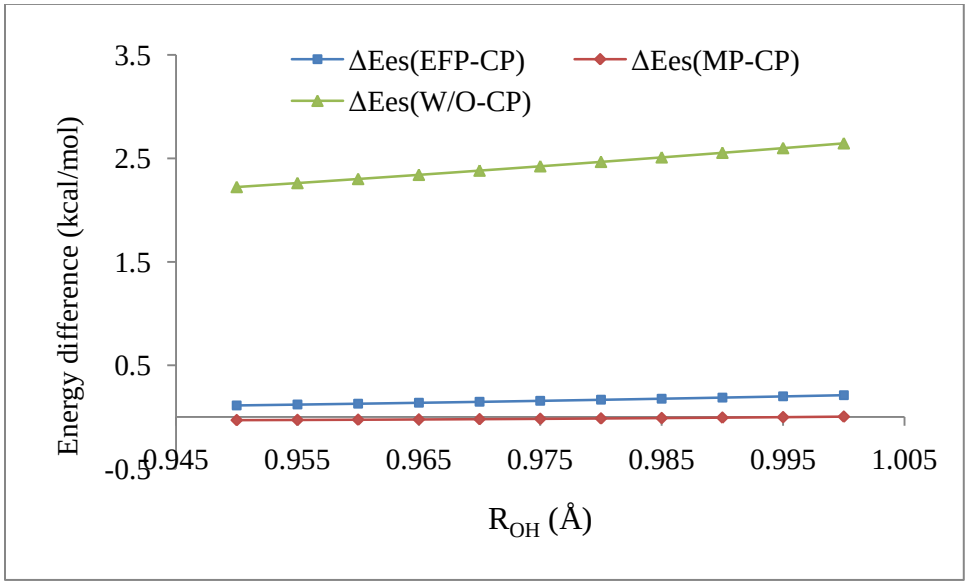

Figure 6. Energy difference between the DPP2-F and SAPT electrostatic energies for water dimers with respect to the O-H separations (Category 2 in the training set).

Figure 6 plots electrostatic energy of dimers as the donor OH distance increases from 0.95 to 1.0 Å. The charge penetration contribution is about 2.4 kcal/mol energy and grows slightly as the R_{OH} increases. Both penetration schemes perform well.

It would be useful to predict when the charge penetration effect is pronounced and how well the charge penetration damping scheme perform then. A general rule of thumb is, for the Cs dimer geometries, along the O-O direction, damping schemes work well as water molecules fall reasonably away from each other and R_{OO} is greater than 2.7 Å. This certainly is an oversimplified rule for different configurations, as demonstrated by the Smith dimer set in Figure 7. Several of these dimers pose special difficulty for the DPP2-F model. EFP-CP scheme improves the Smith dimer 7 to 10 significantly, compared with the MP-CP. Both schemes record large errors for dime 5 and 6. Since including these dimer structures in the training set and increasing their weight in the fitting do not improve the model performance for those dimers, the failure probably comes from the interplay between charge penetration functions and the three-point-charge representation.

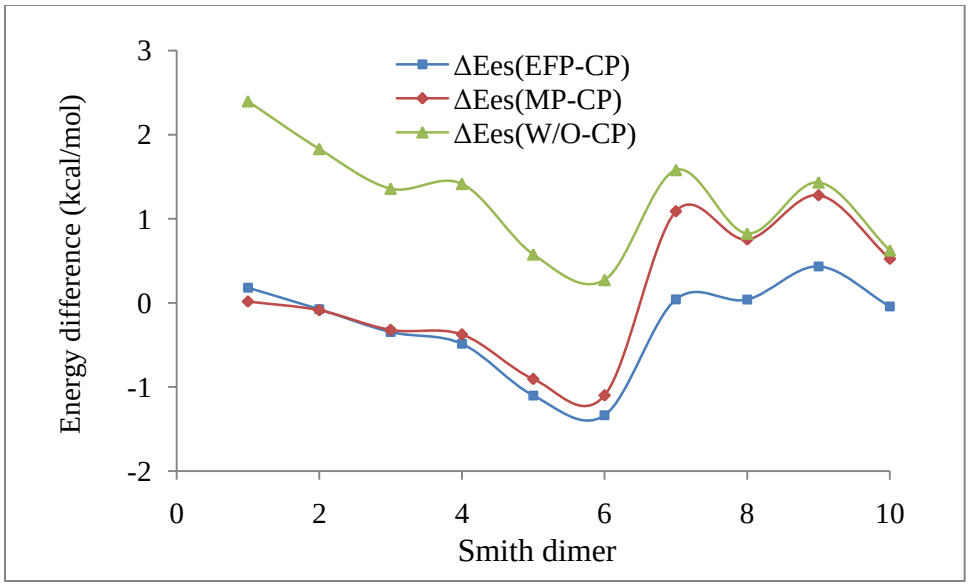

Figure 7. Energy difference between the DPP2-F and SAPT electrostatic energies for the Smith dimer set.

The causes of the differences between the DPP2-F model and SAPT electrostatic energies are due to the limitation of three point charge representation and the insufficiency of the damping scheme. According measured site-site radial distribution functions for water and ice by Soper, [135] the distances of OO, OH and HH are generally greater than 2.55, 0.75 and 1.15 Å, respectively. The probabilities of finding configurations with shorter site-site distances are very small. When an atom of one water molecule is at a reasonably distance to the atoms of another water molecule, the damping scheme produces electrostatic energies in good agreement with SAPT. When the atoms from different molecules get too close, large errors appear due to short OO, OH or HH separations.

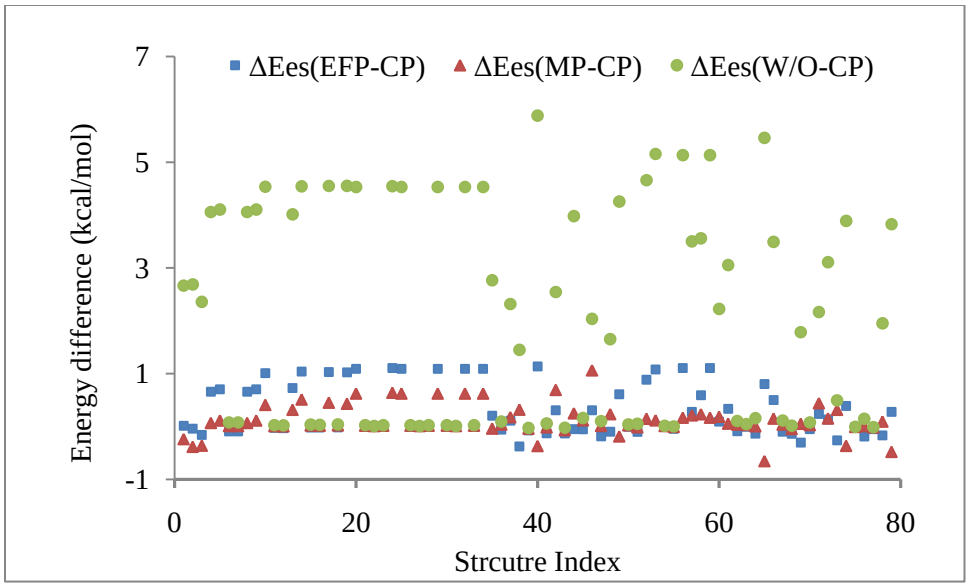

Figure 8. Energy difference between the DPP2-F and SAPT electrostatic energies for eighty water dimers taken from water clusters (Category 6 in the training set).

In Figure 8, the charge penetration contributions for dimer structures taken from $(H_2O)_3$, $(H_2O)_4$, $(H_2O)_5$ and $(H_2O)_6$ are plotted. In the current work, we limit our discussion to small water clusters. Further development of the model would include representative structures from some medium-size water clusters ($(H_2O)_n$, $20 \leq n \leq 40$), since the water configurations might be gradually changed due to the increasing polarization as the size of the clusters grow.

The two charge penetration schemes explored do not fully recover the penetration energy at very short O-O distances. The poor performance of the models under these distanced may still happen in MC/MD simulations, but at a reduced scale. Fortunately, in real bulk water and water clusters, water molecules rarely move so close to each other, these two methods both give reasonable electrostatic energies comparable to the SAPT values. The Gaussian electrostatic model (GEM),[136] a force field based on density fitting, resorts to Hermite Gaussian densities derived from *ab initio* calculations on molecules. It allows a direct inclusion of short-range

quantum effects by means of the computation of electrostatic and repulsion integrals. The penetration energies of Smith dimer set were excellently recovered by the approach.

Another limitation of applying the current damping scheme for charge penetration effect is that it only augments the energy calculation and does not bring the charge penetration effect into the dipole calculation.

4.2 ATOMIC POLARIZABILITIES AND THE POLARIZATION INTERACTION

The polarization term arises from the response of a water molecule to the electric fields arising from the surrounding molecules. As shown by many researchers, inclusion of many-body interactions is essential for accurately describing intermolecular interactions. The DPP2-F model, like most polarizable models, has the polarization part as the only energy term to capture the many-body effects. Differing from the approach used by the DPP2 rigid model, we fit to all polarization tensor elements through fitting to the molecular polarizabilities of sixty four water monomers and the dipole moments of water dimers.

Underlying the development of the DPP2-F model, we are interested not only in energies, but also in reasonable calculations of dipoles. The dipole moments computed by the DPP2-F model include contributions from the point charges and from the induced dipole contributions from the polarization term. Since the point charges are transformed from the PS-DMS and are believed to be accurate for isolated water monomers, there is not much incentive to modify them. The induced dipole, however, is explicitly computed in the self-consistent iteration scheme before the polarization energy is calculated.

Atomic polarizabilities are usually treated as constants. In the DPP2-F model, however, we describe them in term of simple functions of the point charges on each charge site to account for the molecular flexibility. Though the function is linear, the computed atomic polarizabilities included the non-linear dipole moment information embedded in the point charges. When the rigid body approximation is applied, the atomic polarizabilities then reduce to the equilibrium α_O^0 and α_H^0.

Table 7. Atomic polarizabilities determined using the Thole's original exponential form and modified exponential form of damping. GD is an abbreviation for geometry-dependent atomic polarizabilities. The DPP2-F model relates to modified exponential form w/GD. Its atomic polarizabilities have five parameters: $\alpha_O^0, \alpha_H^0, a_{DD}^{intra}, g_m$ and g_h .Note the DPP2-R is rigid model, but the parameters are used for the flexible water molecular configurations.

Damping	Thole's exponential form			Modified exponential form		
	DPP2-R	w/ GD	w/o GD	TTM-4F	DPP2-F	w/o GD
α_O^0/ Å^3	1.22	1.22	1.293	1.31	1.35	1.32
α_H^0 /Å^3	0.28	0.223	0.28	0.294	0.285	0.38
a_{DD}^{intra}	0.3	0.3	0.3	0.626	0.505	0.626
g_m	-	0.9926	-	-	1.336	-
g_h	-	-0.92445	-	-	0.5712	-
Error(%)	24	14.8	23.7	23.2	4.8	17.6

The fitting errors from using the charge dependent atomic polarizabilities and the two forms of exponential damping expression are compared in Table 7. The fitting error is defined as

$$Error = \left[\frac{\sum_{n=1}^{64} \left[\sum_{j \geq i}^{3} \sum_{i=1}^{3} \left(\alpha_{ij}^{model} - \alpha_{ij}^{MP2} \right)^2 \right]}{\left[64 \times \alpha_{MP2}^2 \right]} \right]^{\frac{1}{2}} \qquad (46)$$

It is a percentage of the MP2 water isotropic molecular polarizability (1.42 Å^3) , by summing up the square of differences of the six molecular polarizability components between the model and MP2. Sixty four monomer structures were included in the fitting and the geometries varied from 102.5 to 108.5 ^{o}for the bend angle and 0.9072 Å to 1.0572 Å for the O-H distances. The original exponential charge density expression (m = 3) was proposed by Thole. The DPP2-R rigid model has atomic polarizabilities of 1.22 Å^3 for oxygen and 0.28 Å^3 for hydrogen. It retains the induced dipole damping factor (α_{DD}^{intra}) 0.3 of the DPP model and does not distinguish intra- and inter-molecular interaction. By applying these parameters to the training set a total error of 24 % resulted. Refitting the oxygen and hydrogen atomic polarizabilities helped slightly, reducing the total error by 0.3 %, and leading to atomic polarizabilities 1.29 Å^3 for oxygen and 0.28 Å^3 for hydrogen. We then introduced the geometry dependency to the atomic polarizabilities, keeping the dipole damping (a_{DD}^{intra}) and refitting the four parameters: α_O, α_H , g_m and g_h . It cut the fitting error more to 14.8 %, and generated the equilibrium atomic polarizabilities, 1.22 Å^3 for oxygen and 0.223 Å^3 for hydrogen. The values are close to those from the DPP2-R model.

Inspired by Burnham's finding that raising the power exponent from m = 3 to m = 4 was necessary in order to match both the equilibrium monomer polarizability and the first order changes in polarizability as a function of nuclear displacements, we studied the modified exponential charge density damping m = 4. Employing the TTM4-F approach and parameters, but removing the charge-charge damping in the electrostatics for comparison (the energy

difference is negligible), we produced an error of 23.2 %, almost the same as that of the DPP2-R. It does not contradict with Burnham's result, though, in which only the equilibrium geometry is considered. Though the TTM4-F parameters did not give much improvement in term of total error for our test case, we confirmed that the modified charge density scheme improves the monomer molecular polarizability surface (also see Figure 9). When we simultaneously fit the five parameters, the fitting error was reduced to 4.8 %. The oxygen and hydrogen equilibrium atomic polarizabilities of 1.35 and 0.285 $Å^3$, respectively, are close to the 1.31 and 0.28 $Å^3$ values used in TTM4-F.

Figure 9 displays the isotropic molecular polarizabilities of the water with respect to the displacement of one hydrogen atom along the OH bond direction. The equilibrium molecular polarizabilities of the DPP2-F, TTM-4F and MP2 are very close, at about 1.42 $Å^3$. The slope from the MP2 calculations is the steepest, followed by the DPP2-F and TTM4-F models, whereas the DPP, DPP2-R and AMOEBA models seriously underestimate this slope. It is apparent that the modified charge density (m = 4) used by the DPP2-F and TTM4-F, nicely captures this steep relation, the slope of which is closely related to the functional expression of the Thole's damping scheme. The slope is insensitive to the atomic polarizabilities and intramolecular damping, the values of what could affect the value of the equilibrium molecular polarizability.

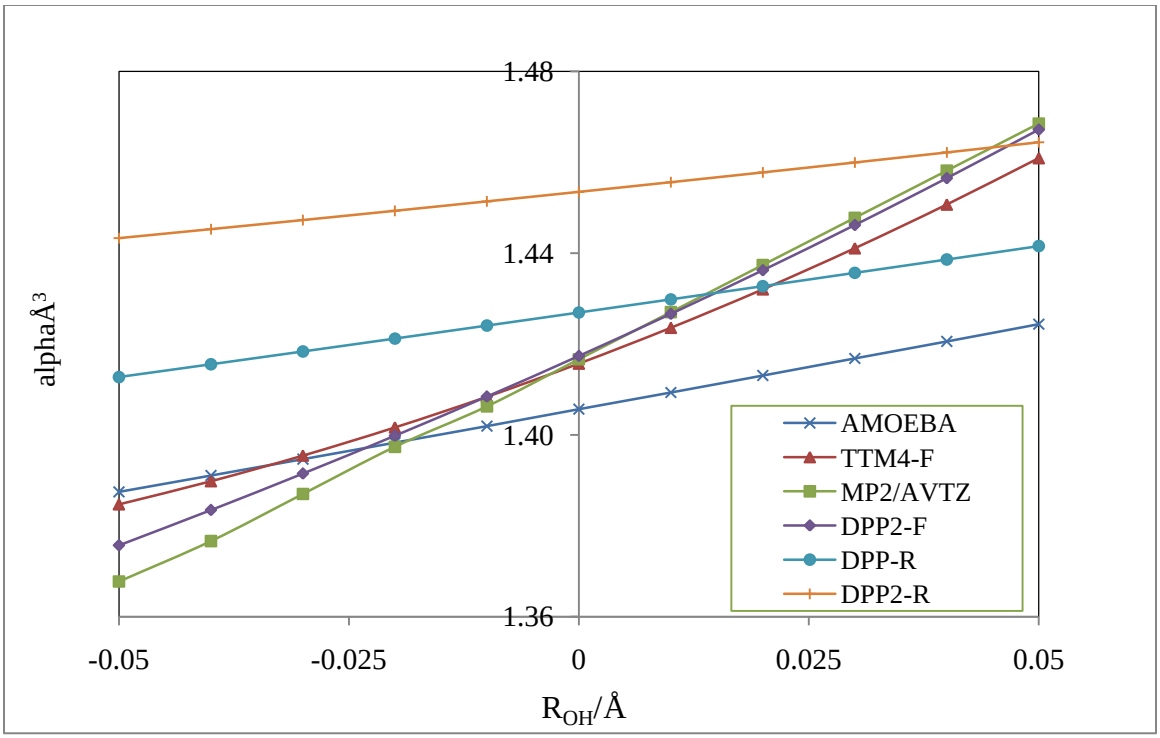

Figure 9. Variations of the molecular polarizability of water monomer with OH stretch. R_{OH} is the displacement of that hydrogen atom relative to its equilibrium position.

The atomic polarizabilities are of great significance for induced-dipole polarizable model. Several schemes had been proposed to compute them from quantum mechanics calculations. [137,138,139,140] These partition methods, however, are often arbitrary and non-transferable. In the induced dipole polarization approach, atomic polarizabilities were commonly taken from Thole's paper [50] and slightly modified for specific goals. Considering the original exponential damping functions, Thole determined the values of 0.837 $Å^3$ and 0.496 $Å^3$ for oxygen and hydrogen, and set the damping factor to 0.572 by fitting to the experimental polarizabilities of a dozen molecules. The AMOEBA water model used the same atomic polarizabilities but changed the damping factor to 0.39 in order to improve the water cluster energy calculations. This led to smaller equilibrium monomer polarizability of 1.408 $Å^3$. Xantheas and Burnham also employed

the same atomic polarizabilities in their TTM2-R(F) and TTM2.1-F models. However, they separated the charge-dipole and dipole-dipole damping factors (0.2 and 0.3 respectively) for better fits on water cluster energies. The DPP model farther weakened the charge-dipole damping from 0.2 to 0.23, in order to improve water hexamer isomer binding energies. A subtle inconsistency needs to be brought out. Thole parameterized the atomic polarizabilities on the three atomic centers of water. The TTM2/TTM2.1-F and DPP models are four-site models, thereafter, have different electrical fields on the atomic centers from those of Thole's. Considering the model geometry, the AMOEBA model is closer to Thole's than others models, though its electrostatic part contains higher-order multipole terms. So, it would not be surprising to see that atomic polarizabilities determined by Thole are not appropriate for the models with an off-atom site, like DPP, DPP2-R, and /DPP2-F. The atomic polarizabilities and damping factors used by AMOEBA model are similar to Thole's parameters. When they were substituted into the DPP 4-site model, the error is as great as 46.6 %, much more appreciable in magnitude than others.

The present scheme allows a systematic fitting of the polarization part. Though the atomic polarizabilities reported in Table 8, by using the Thole's original and the Burnham's modified damping functions are close in term of values, one should not take it for granted that the atomic polarizabilities can be transferable among different forms of damping scheme. Thole had considered a range of damping functions, and associated atomic polarizabilities vary considerably. The parameters of these damping schemes, together with many other approaches, [141, 142] can also be determined through the fitting scheme reported here.

Table 8. Comparison of atomic polarizabilities, inter- and intra-molecular damping factors (dimensionless) used in different water models.

Model	Thole's	TTM4F	AMOEBA	TTM2.1F	DPP-R	DPP2-R	DPP2-F
	m=3	*m*=4	*m*=3	*m*=3	*m*=3	*m*=3	*m*=4
α_O/Å^3	0.837	1.310	0.837	0.837	0.837	1.220	1.35
α_H / Å^3	0.496	0.294	0.496	0.496	0.496	0.280	0.285
a_{CD}	0.572	0.400	0.390	0.2	0.23	0.21	0.389
a_{DD}^{intra}	0.572	0.626	0.39	0.3	0.3	0.3	0.505
a_{DD}^{inter}	0.572	0.055	0.39	0.3	0.3	0.3	0.0581

The DPP2-F model has three damping factors in the polarization energy part: the charge-dipole (α_{CD}), the intramolecular dipole-dipole (α_{DD}^{intra}) and the intermolecular dipole-dipole (α_{DD}^{inter}) damping factors. The only damping factor that enters into monomer polarizability surface is α_{DD}^{intra} and it has been determined together with the atomic polarizabilities. The other two damping factors are associated with intermolecular interactions. They are determined as below.

4.3 DIPOLE MOMENT AND POLARIZATION INTERACTION

After the monomer polarization is established, only α_{DD}^{inter} and α_{CD} are left for the intermolecular polarization and they are obtained by matching the model dipole moments to MP2 dipole moments. The incentive of this strategy comes from four considerations. First of all,

when the point charges are decided, the polarization part is the only potential function that we can modify to improve the (induced) dipole calculation. Theoretically, the infrared intensity I_ν of the normal mode Q_ν is calculated according to

$$I_\nu = C\sum_{i=1}^{3}\left(\frac{\partial \mu_i}{\partial Q_\nu}\right)^2 \qquad (47)$$

where μ_i is dipole moment component, C is a conversion factor from atomic units to km/mol and $\frac{\partial \mu_{i=1,2,3}}{\partial Q_\nu}$ are the dipole derivatives with respect to normal coordinates. The quality of dipoles influences the vibrational spectroscopy and also the electron-water polarization interaction. Secondly, there is a lack of *ab initio* reference energy data for fitting. Although SAPT induction energies are available, they are more negative than the model polarization energies. Fitting to them by varying the two damping factors does not work. It could be an issue with the DPP2-F three-point-charge representation or the polarization damping approach. Thirdly, dipoles are vectors and have more components than single point energies to fit. The last consideration is that it allows us to explore the polarization effects in the large water clusters and liquid/solid states. In the present force field, the enhanced dipoles come solely from the induced dipole, due to the polarization from the global environment of other water molecules. Explicitly including this physics into parameterization will be very useful in extending the models from small water clusters to bulk systems.

Figure 10 plots the total dipoles computed from MP2 and various models for the dimer structures with respect to the hydrogen bonded internal O-H bond (R_{OH}). We move the hydrogen atom to but fix the positions of other atoms. Due to the formation of hydrogen bond with the oxygen in the other water, this OH bond is of primary interest in vibrational spectroscopy. For

water dimer (refer to Table 13), this is the strongest absorption. MP2 IR intensity for this mode is close to 300 (unit in Debye^2-Å $^{-2}$-amu^{-1}), about two and a half times that of the second most intense mode. For models using Thole's exponential damping scheme, i.e., Thole's, TTM2.1-F, DPP2-R and AMOEBA,

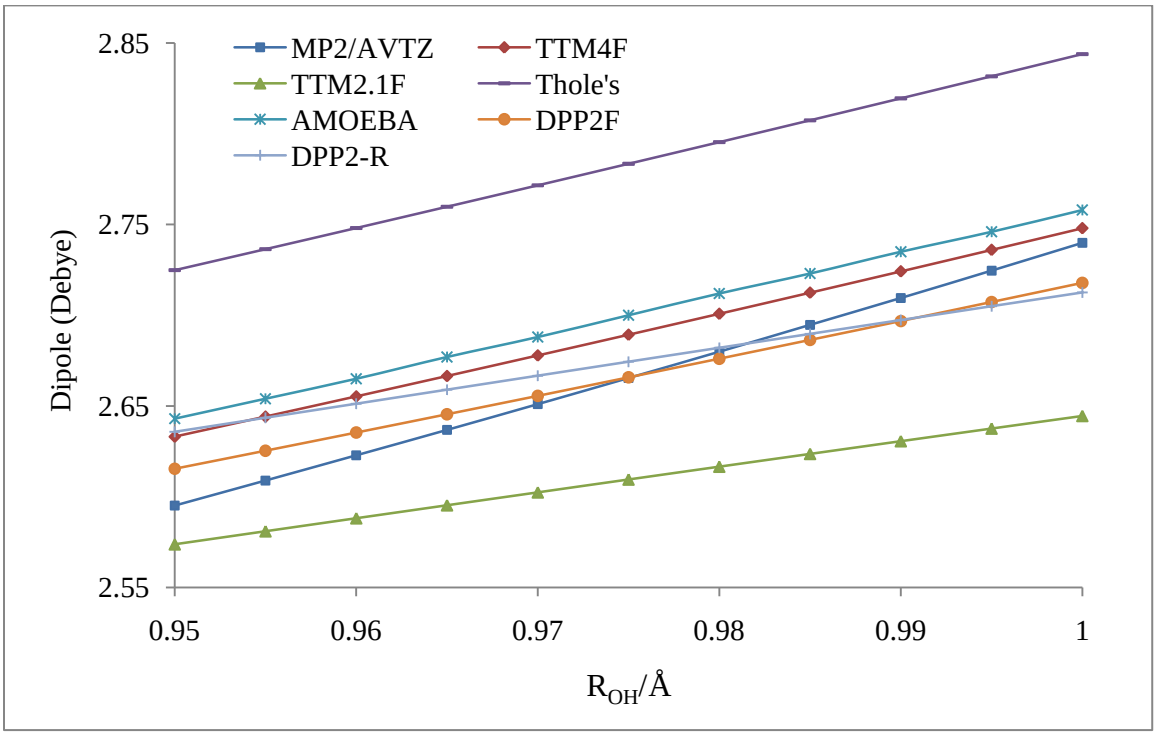

Figure 10. Variations of the dipole moments of the water dimer with respect to the hydrogen bonded internal O-H bond distances (R_{OH}).

, the calculated vibrational intensities of this OH stretch are less than 100, not much different from the intensities of free OH stretches. The TTM4-F model employs the modified exponential damping and has successfully pushes the intensity up to 200. In order to know how the vibrational absorption intensity affected by the total interaction potentials, we can examine the dipole and its derivative (slope) with respect to the R_{OH}.

The dipoles calculated by the DPP2-F model are in the best agreement with MP2 in Figure 10 and 11, followed by the TTM4-F and then AMOEBA models. The dipoles in Figure 10 depend linearly on the O-H separation. The results labeled "Thole's" in Figures 10 and 11, refers to using the Thole's atomic polarizabilities and damping parameter (0.572) in the four-site model. Because the "Thole's" and the TTM2.1-F models have the same polarizable sites, atomic polarizabilities and damping expression, it is included in these two figures to show how the damping factors affect the induced dipoles of water dimer. Clearly the values and the slope of dipoles are sensitive to the combination of the charge-dipole and dipole-dipole damping factors: the TTM2.1-F gives a more accurate dipole moment, while the "Thole's" approach leads to improved dipole derivative.

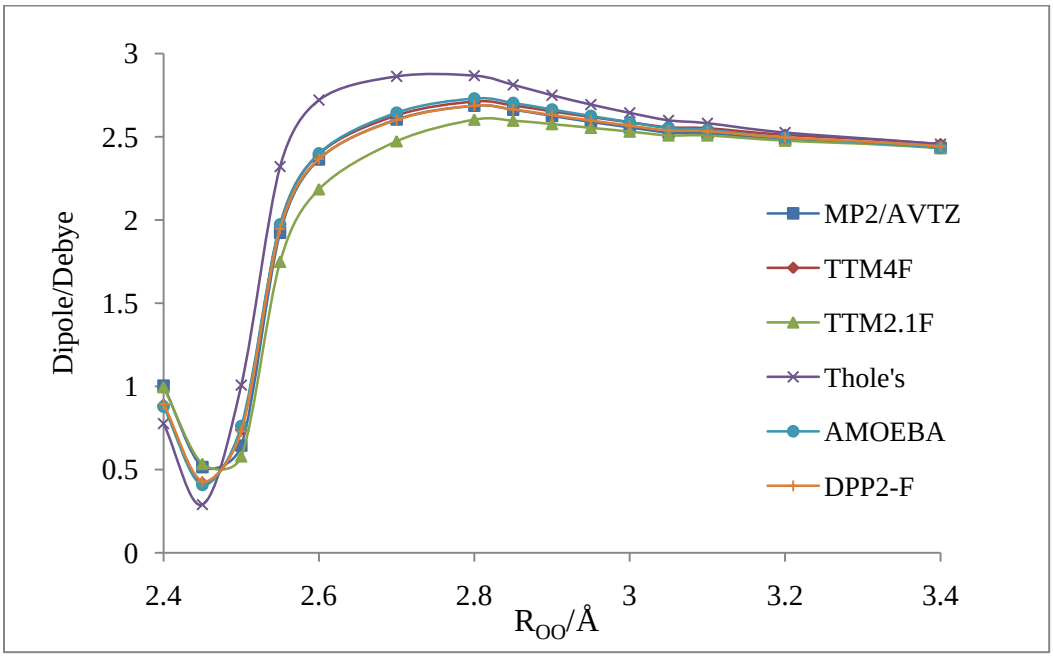

Figure 11. Variations of the total dipole moments of water dimers as a function on the OO distances.

DPP2-R is a rigid-body model. However, we plug its atomic polarizabilities and damping factors in flexible model framework, for comparison. As is shown in Figure 12, the DPP2-R displays the same slope as TTM2.1-F, both of which seriously underestimate the dipoles along the OH dimension. Since the DPP2-R and TTM2.1-F are four-site models, using the same damping expression, and their damping parameters are also close, (see Table 8) the difference of their intercepts and slopes might be caused by the choice of the atomic polarizabilities.

The calculated MP2 dipole derivative along the O-H coordinate is the steepest. This corroborates that the MP2 method gives the greatest O-H stretch intensity. The TTM4-F and the AMOEBA models yield similar slopes, but are flatter than that of MP2. Recall that the TTM4-F model has a modified form of charge density, which is different from the AMOEBA and DPP2-R/DPP/TTM2.1-F models. Similar approach is used in DPP2-F, which predicts a dipole derivative slightly smaller than TTM4-F, but greater than TTM2.1-F.

Several observations need be noted here. First, we see that the original exponential damping used in the models without an off-atom site, e.g. Thole's and AMOEBA model in the figure, also predicts the large dipole derivative, as well as the TTM4-F and DPP2-F models (m=4). The dipole derivative is also influenced by the atomic polarizabilities and all damping factors simultaneously. The DPP2-F model slightly underperforms the TTM4-F with regard to the dipole derivative in this case. Varying the two intermolecular damping factors did not improve the slope much. Unfortunately, none of these models exactly reproduce the dipole derivative of MP2. This clearly indicates a deficiency in all these models.

Second, the AMOEBA and Thole's model have similar dipole derivative, though the dipole calculated from the latter approach are way off from the MP2 dipole. Here AMOEBA differs from Thole's not only in the damping factors, and also in a subtle aspect, that AMOEBA

does not have *M*-site and is close to the real Thole's approach. With this and the previous discussion in mind, the three-point charge polarizable water model, with charges on hydrogen and oxygen atomic sites, using original Thole's charge density damping scheme, might still be able to yield satisfactory results in the polarization part.

The electric field should reflect the charge penetration effect, due to the associated charge redistribution. Allowing damped electrical fields into polarization term does not lead to much difference in dipole and polarization energies. So in the development of the DPP2-F model, the influence from the charge penetration on the static electrical field was neglected. This is supported by Figure 11 which shows that the dipoles calculated with the DPP2-F closely match those from MP2, as the O-O separation between the two water molecules staying greater than 2.7 Å. The TTM4-F and AMOEBA models give similar dipole moments as the DPP2-F model, Although the results from the DPP2-R and TTM2.1-F models are not as good as the DPP2-F, their values at the short distances (Table 9) agree better with MP2 than the DPP2-F and TTM4-F models,

Table 9. Variations of the dipole moments (debye) of water dimers (Cs symmetry) with different OO separations. Note in the "Tholes" model we uses Thole's exponential damping and parameters in the DPP2-F four-site model.

R_{OO}/Å	MP2/AVTZ	DPP2-F	TTM4-F	AMOEBA	Thole's	DPP2R	TTM2.1-F
2.4	1.00	0.89	0.89	0.88	0.78	0.97	1.00
2.45	0.52	0.43	0.42	0.41	0.29	0.49	0.53
2.5	0.64	0.73	0.74	0.76	1.01	0.67	0.58
2.55	1.92	1.95	1.97	1.97	2.32	1.88	1.75
2.6	2.36	2.37	2.40	2.40	2.72	2.32	2.18
2.7	2.60	2.60	2.63	2.65	2.86	2.58	2.47

4.4 CHARGE TRANSFER

Induction is an attractive contribution to the total molecular interaction. The SAPT induction energy for the equilibrium geometry of water dimer (O-H bond distance at 0.97 Å and O-O distance at 2.91Å) is about two times larger in magnitude as that of the model potential, as shown in Figure 12. The difference between SAPT induction and E_{pol} for dimer minimum is 1.4 kcal/mol. The DPP2-F polarization energies, E_{pol}, severely underestimate the negative SAPT induction components and the difference generally increases as the O-H distances (R_{OH}) increase (Figure 12) and the O-O distances (R_{OO}) shorten (Figure 13).

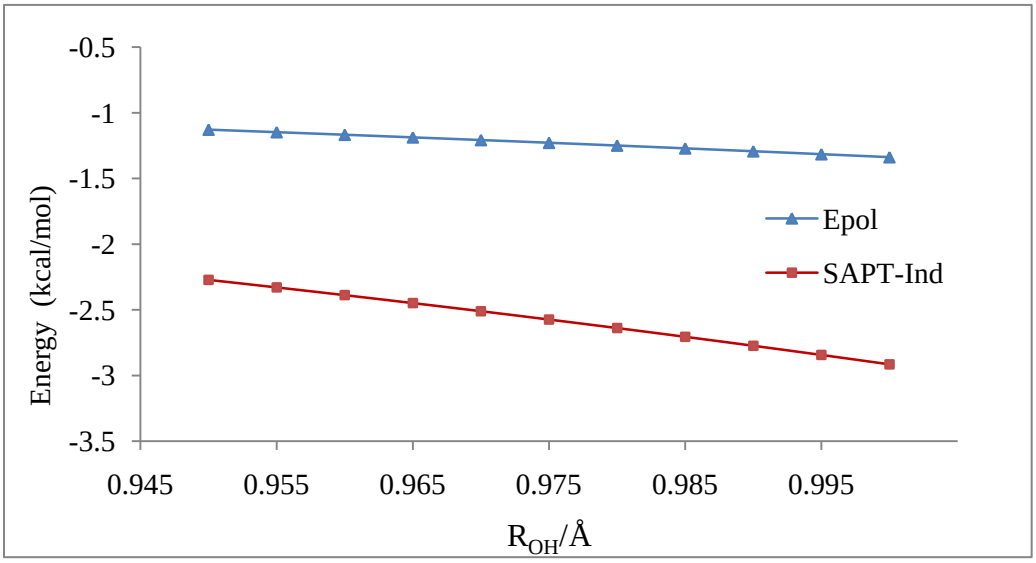

Figure 12. Comparison of the DPP2-F polarization energies and the SAPT induction energies for water dimers as a function of the OH distances.

In SAPT, the charge-transfer energy is normally absorbed into the induction energy. [143]To model this missing component, we follow what the DPP2-R did and include an extra

energy term, charge transfer term (E_{ct}), in the induction potential part. In DPP2-R, the charge transfer term has been matched to an ALMO EDA analysis [144] of the Hartree–Fock/aug-cc-pVTZ wave functions. Strictly speaking, the charge transfer is part of the induction term, so we fit the charge transfer term to the difference between SAPT induction and model polarization energies

$$E_{ct} = E_{ind}^{SAPT} - E_{pol} \qquad (48)$$

In this way, the sum of the model charge transfer and polarization is then comparable to the SAPT induction.

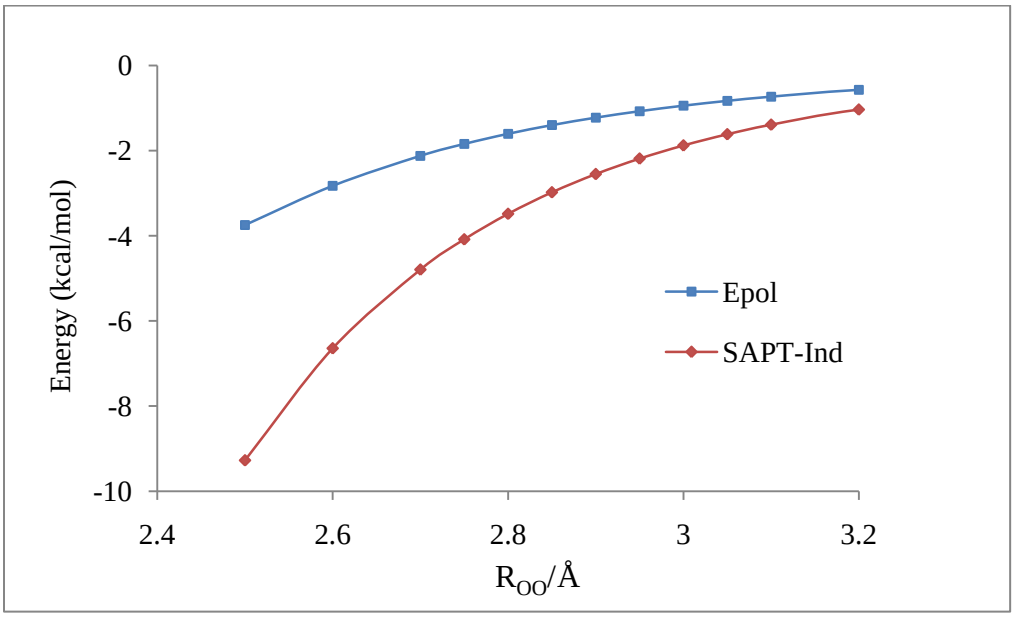

Figure 13. Comparison of the DPP2-F polarization energies and the SAPT induction energies for water dimers with respect to the O-O distances.

Commonly accepted in the field of experimental spectroscopy, the role of the charge-transfer energy in force fields is not straightforward. It is considered to be a part of the induction energy but the deconvolution of E_{ind}^{SAPT} onto E_{pol} and E_{ct} is not unique, because the magnitude of

E_{ct} is basis-set dependent. Owing to its short-range overlap dependent character, E_{ct} was either modeled by the atom-atom functional form similar to that of the repulsion energy, but attractive, or by the approach used in SIBFA.[145]

It remains a problem, whether the explicit exponential form charge transfer term really is necessary for a polarizable model to achieve a satisfactory description of the total interaction energy. In principle, the charge transfer between two water molecules uses the intermolecular oxygen-hydrogen exponential function,

$$E_{ct} = \sum_{OH} a_{OH} \exp\left(-b_{OH} R_{OH}\right) \qquad (49)$$

which also appears in the model exchange-repulsion expressions

$$E_{ex-rep} = \sum_{OH} a_{OH} \exp\left(-b_{OH} R_{OH}\right) + \sum_{HH} a_{HH} \exp\left(-b_{HH} R_{HH}\right) + a_{OO} \exp\left(-b_{OO} R_{OO}\right) \qquad (50)$$

The charge transfer contribution can then be considered as being implicitly represented by a concomitant reduction in the magnitude of exchange-repulsion energy, for the models without explicit charge transfer term. Furthermore, because the charge transfer is closely associated with the polarization and electrostatic energies, it surely leads to the change redistribution among different molecules. The use of the exponential function limits the augmentation by the charge transfer only at the energy level.

4.5 DISPERSION, EXCHANGE-REPULSION AND TOTAL INTERACTION ENERGY

Most water potentials have included one single repulsion and dispersion site for each water molecule generally centered on the oxygen atom. Lennard-Jones potential, and many of its variants have been employed to model the dispersion and exchange-repulsion together, for instance, the all-atom buffered 7-14 potential in AMOEBA and the series of R^{-n} of O-O pairs in the TTM4-F model.

Because the dispersion in the DPP2-F(R) models based on atom-atom R^{-6} terms satisfactorily produces the SAPT dispersion energies, the discussion below deals exclusively with the exchange repulsion.

Similar to the case of polarization, there are different ways to define the repulsion interaction for the model potential. One definition, used in models like SIBFA [146]and EFP [147], is the Hartree–Fock exchange–repulsion energy. Exchange repulsion with correlation correction is also available with the aid of SAPT. This approach allows for a systematic improvement of each term based on a physical dissection and actually was what we intended to do. However, as shown later, the error from each energy term can build up and leads to poor performance of the total interaction potential. We choose another common approach, used in NEMO [148] and DPP2-R, in which the repulsion is defined as a residue term, i.e.

$$E_{rep} = E_{total}^{MP2} - E_{\mathrm{int}ra}^{PS} - E_{es} - E_{pol} - E_{ct} - E_{disp} \qquad (51)$$

With this definition, the repulsion will also contain overlap corrections to the induction, dispersion, charge transfer and more importantly, electrostatic energies. The advantage of this approach is that errors inherent in each term can be effectively offset. More water cluster

structures beyond water dimers can be included in the fitting, because the MP2 binding energies would easily be computed. These benefits come at the expense of the transferability.

The DPP2-F model was constructed based on term-by-term fitting to reference *ab initio* data and the total interaction energies are expected to match MP2/aug-cc-pV5Z values. We look at the energy differences between the DPP2-F model and MP2 and examine carefully the source of these differences, by comparing the model energy contributions from each potential energy term and its corresponding SAPT values. It allows a close look on how well the commonly used energy functional forms perform and sheds valuable insights on the extent of error canceling.

The energy difference (deviations) of each component of the model from the comparable SAPT term, denoted as ΔE, is defined as

$$\Delta E_X = E_X^{model} - E_x^{SAPT}$$

with X representing electrostatic, induction, dispersion and exchange-repulsion.

The total energy difference between the DPP2-F model and the MP2, written as ΔE_{total}, is then the sum of all the deviations above and ΔE_{MP2}, the discrepancy between MP2 and SAPT.

$$\Delta E_{total} = \Delta E_{es} + \Delta E_{ind} + \Delta E_{disp} + \Delta E_{ex-rep} + \Delta E_{MP2} \qquad (52)$$

Since SAPT calculation only gives the intermolecular interaction energy, we define SAPT total interaction energy for a given structure, E_{total}^{SAPT}.

It consists of four SAPT interaction energy terms ($E_{es}^{SAPT}, E_{ind}^{SAPT}, E_{disp}^{SAPT}, E_{ex-rep}^{SAPT}$) plus intramolecular distortion contribution, which is approximately represented by the Partridge-Schwenke monomer energy (E_{int}^{PS}).

$$E_{total}^{SAPT} = E_{es}^{SAPT} + E_{ind}^{SAPT} + E_{disp}^{SAPT} + E_{ex-rep}^{SAPT} + E_{int}^{PS} \qquad (53)$$

The difference between SAPT total interaction energy and MP2 interaction energy is written as $\Delta E_{MP2} = E_{total}^{MP2} - E_{total}^{SAPT}$. They are generally no greater than 0.2 kcal/mol for those water dimers in the training set.

The total interaction energy differences between the DPP2-F model and MP2 for several classes of water dimer structures are presented in Figure 16-20. The deviations of the model electrostatics, induction, dispersion, and exchange-repulsion energies from the SAPT values are also included in these figures.

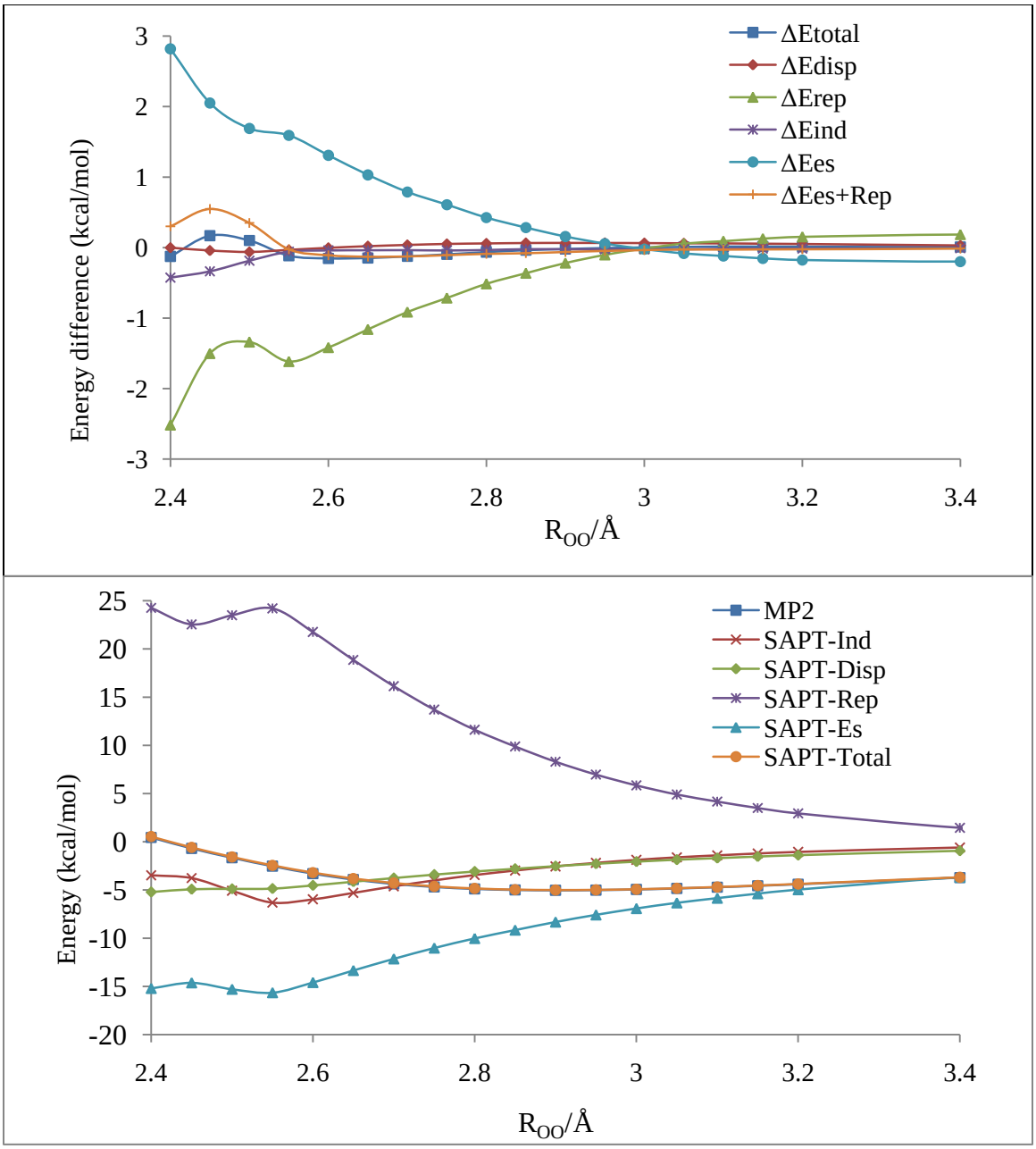

Figure 14. Energy differences between SAPT and the DPP2-F model (top) and energy contributions to the total interaction energies (bottom) for water dimers as a function of R_{OO}.

Figure 14 shows energy differences of the DPP2-F model for water dimers as a function of O-O distances (R_{OO}). For comparison, the total MP2 interaction energies, SAPT total interaction energies and the SAPT energy components are also included. The SAPT total energy

curve excellently overlaps with the MP2 curve. The reported dimer structures were constrained optimized for the given O-O distances and all still kept the Cs symmetry. When the two water molecules approach very close to each other (around 2.5 Å), the sharply increased repulsion forces the configurations of the water molecules take dramatic changes, leading to the humps of the curves at short R_{OO}. Dispersion from the model is in excellent agreement with SAPT. The differences are generally less than 0.2 kcal/mol. Deviation of induction energies is generally close to zero. It turns increasingly negative as the R_{OO} decrease to below 2.55 Å, but it is no greater than 0.3 kcal/mol when R_{OO} shortens to 2.4 Å.

Figure 14 (also Figure 15-18) clearly shows that the dispersion and induction interactions of the DPP2-F model perform well and match the SAPT dispersion and induction energies excellently. The deviations from these two energy term are generally negligible, compared with the errors of the total energies. The DPP2-F model electrostatic, being enhanced with the EFP charge penetration scheme, generally performs well, but it is still insufficient in reproducing the SAPT electrostatic energies for certain water clusters, like the dimer with very short R_{OO} and some Smith dimers. Fortunately the model exchange-repulsion expression generates errors in the opposite direction from the electrostatics. It underestimates the SAPT repulsion energy by 2.5 kcal/mol when two water molecules are 2.4 Å away (Figure 14), while in the meantime, the model electrostatic overestimates the SAPT electrostatic energy by 2.8 kcal/mol. The deviations from electrostatic and exchange-repulsion energies going to opposite directions, which happened for structures in all categories, encourage us to combine the electrostatic and repulsion into ΔE_{es+Rep} and include them in these figures. The difference between ΔE_{es+Rep} and ΔE_{total} shown in these figures is attributed to the errors build up from dispersion, polarization and charge transfer. The DPP2-F model performs very well in calculating the total interaction energies, when the R_{OO}

distances are longer than 2.55 Å, thanks to the excellent balance among the model repulsion, electrostatic, and all other energy components. As the separation between the oxygen centers decreases, errors for repulsion and electrostatic energies both exceed 2.5 kcal/mol; while $\Delta E_{es+Reps}$ is still below 0.5 kcal/mol.

The present three-point-charge, four-site representation, with EFP charge penetration, has augmented the electrostatic energies comparable to the SAPT electrostatic energies, but for many configurations, the errors are still appreciable. The errors introduced in the electrostatic part have to be balanced. By explicitly fitting the exchange repulsion part to the difference between reference *ab initio* energies and the sum of all other model energy terms, those deviations from the electrostatic energy and other terms, has been offset to a satisfactory extent.

Long-range interactions are due to electrostatics, polarization, and dispersion; while exchange repulsion, charge transfer, and charge penetration are considered to be short-range effect. In the DPP2-F model, charge transfer term has been parameterized to complement the polarization term in order to match the SAPT induction energies. The long-range interactions, along with the charge transfer are well produced in the models. What are left are the exchange repulsion and charge penetration, and they are seen to complement each other.

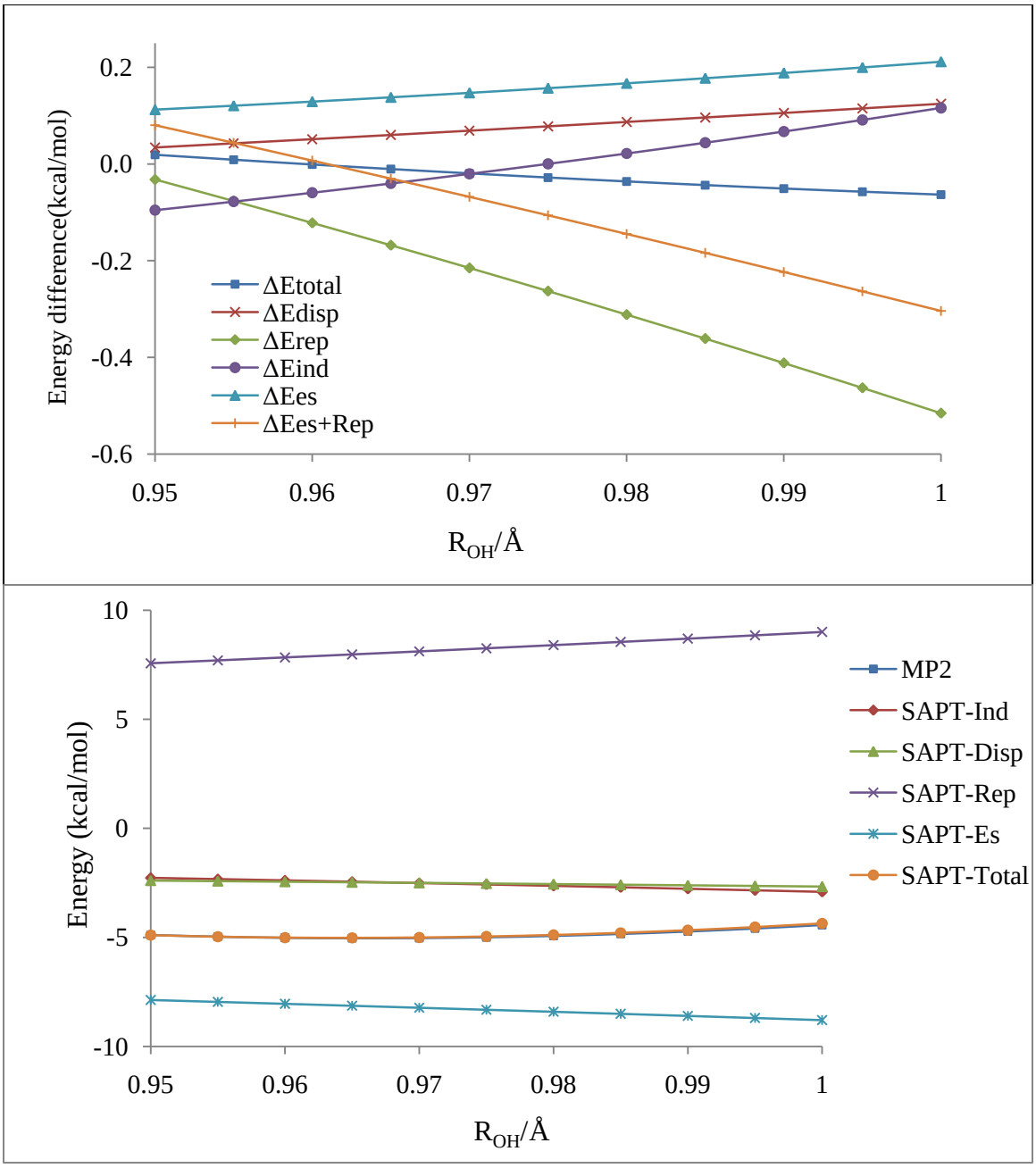

Figure 15. Energy differences between SAPT and the DPP2-F model (top) and energy contributions to the total interaction energies (bottom) for water dimers as a function of R_{OH}.

The interaction energy differences for water dimer with varying OH distances (R_{OH}) along the H-bonded OH bond are plotted in Figure 15. It allows the investigation on how well

the DPP2-F model potential energy functions perform on the dimer H-bonded OH stretch. The attractive-repulsive interaction of the TTM flexible model series acts only between O sites and thereafter would not differ as the ROH varies. Only the electrostatic and polarization energy change. The DPP2-F model has dispersion and repulsion interaction among all atoms form different water molecules. From the Figure 15, the DPPE-2 repulsion part has the greatest deviations from the SAPT values in order to balance the model. It underestimates the SAPT repulsion by 0.22 kcal/mol at the equilibrium R_{OH} and by 0.5 kcal/mol when the R_{OH} is 1.0 Å. The difference of total energy between the DPP2-F model and MP2 is close to zero as R_{OH} varies from 0.95 to 1.0 Å, indicating that the DPP2-F model performs very well for this OH stretch. We will show later, however, that the good description of the potential energies on the OH stretch is still not sufficient for a satisfactory prediction of the OH stretch frequency.

The "tilt' angle $\angle H_{11}O_1O_2$ (see Figure 16) is of great significance for the fitting of the exchange-repulsion interactions. Including structures with different angles in the fitting of the exchange-repulsion term is necessary for the model to do the geometry optimization reasonably. The angle serves a similar goal as the "flap angle" noted in the development of the DPP2-R and DPP models. [21,20].

Again some Smith dimers present troubles for the model, as shown in Figure 17. For the three structures with large total energy differences (dimer 4, 5, and 6), the contributions from the model dispersion and induction are small. The differences between the DPP2-F electrostatic and the SAPT values are -0.5, -1.1, and -1.3 kcal/mol, respectively. Repulsion term, trying to offset the electrostatics, however, severely overcorrects the model total energies and leads to total energy errors over 1.5 kcal/mol for these three configurations. Since these structures are similar to each other, all having a four-member ring with alternating O and H atoms, the

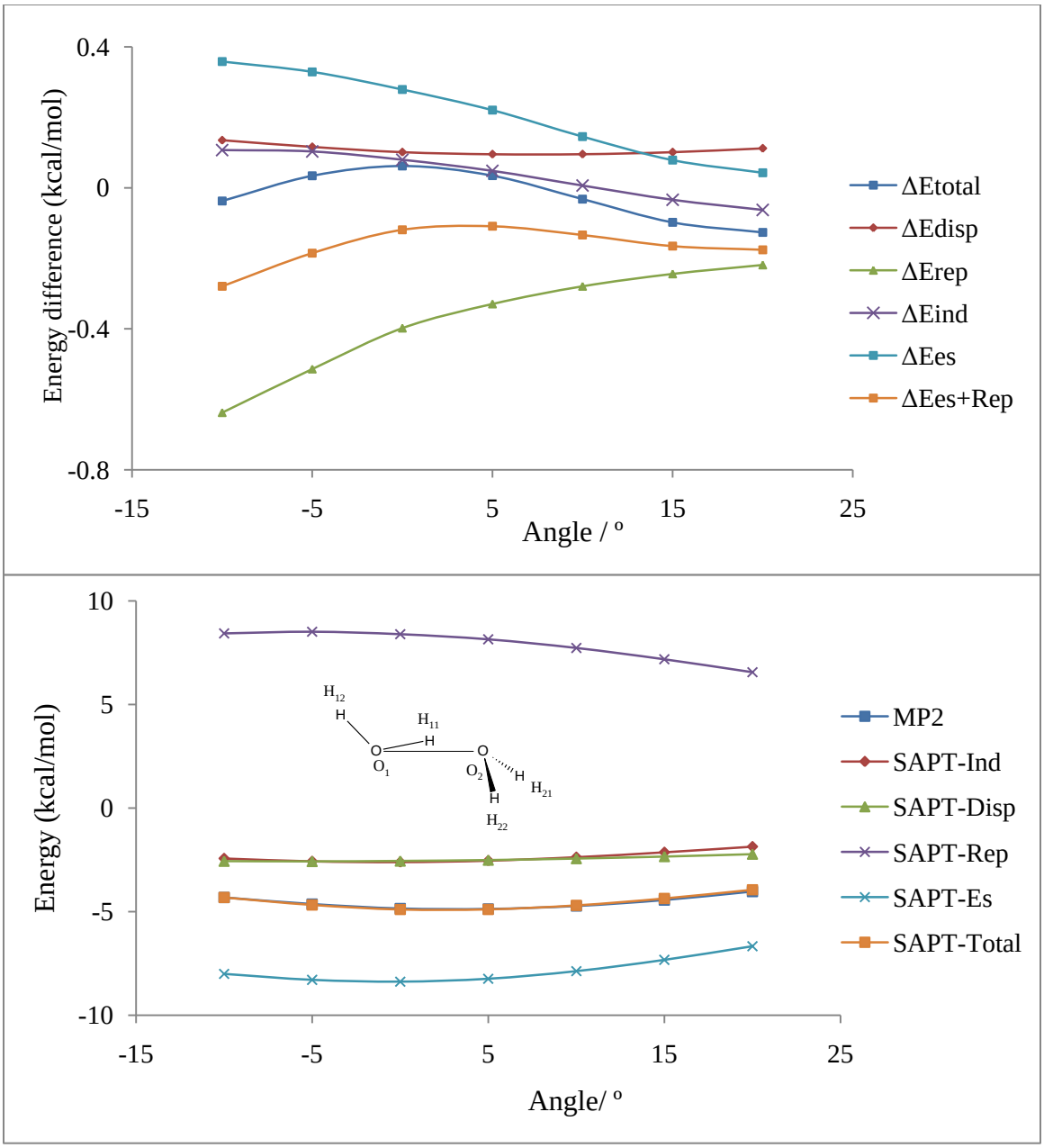

Figure 16. Energy differences between SAPT and the DPP2-F model (top) and energy contributions to the total interaction energies (bottom) for water dimers as a function of angle $H_{11}O_1O_2$. The OO distance is fixed at 2.91 Å. The equilibrium angle is 5.1 ºat the MP2/AVTZ level.

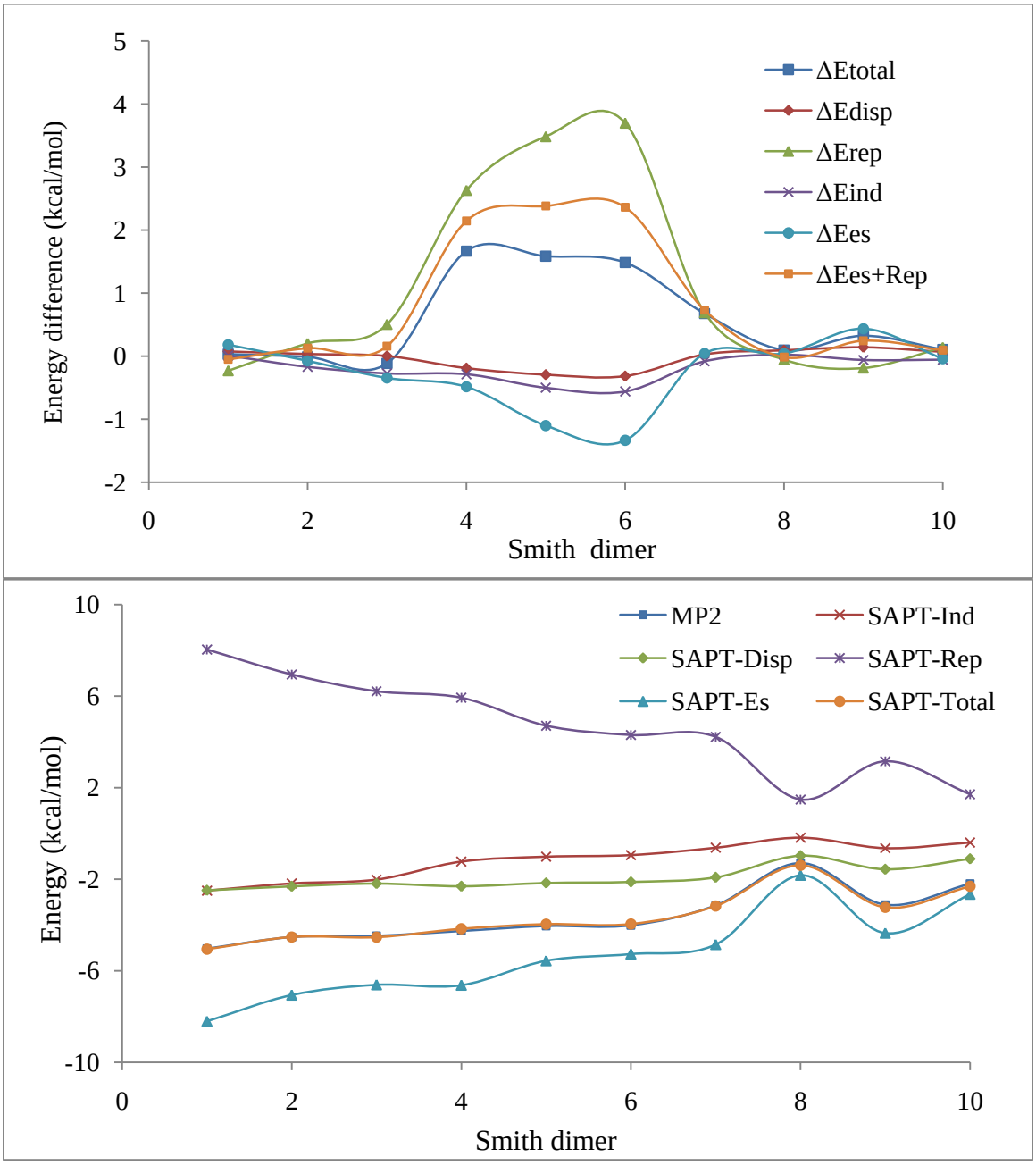

Figure 17. Energy differences between SAPT and the DPP2-F model (top) and energy contributions to the total dimer potential energies (bottom) for the ten Smith water dimers (index from 1 to 10). The structures of these dimers, abbreviated as S1 to S10, can be found in the reference 21. S1 is the water dimer minimum.

parameters for the current repulsion functions could be readjusted to improve the description of the total energies.

In the Table 10, the energies components for some representative water clusters are given. The DPP2-F model correctly optimizes the four hexamer isomers, but the relative energies differ from those of MP2. This is expected to be improved by reformatting the exchange-repulsion term in the future. The fraction of induction energy (the polarization plus charge transfer for the DPP2-F model), to the total electrostatic energies (the sum of the electrostatic and induction energies) is not sensitive to the cluster size, except for the dimer. Induction accounts for about 30% of the total electrostatic energies in these water clusters by DPP2-F, same as by the TTM4-F.

Table 10. Interaction energies (kcal/mol) for water cluster. Except W20 and W24, results of the small clusters are based on optimized geometries using each method. MP2 calculations use density fitting and aug-cc-pV5Z basis set.

	DPP2-F						TTM4F	MP2
	E_{pol}	E_{ct}	$E_{ex\text{-}rep}$	E_{es}	E_{total}	$E_{ind}/(E_{ind}+E_{es})$	$E_{pol}/(E_{pol}+E_{es})$	
W2	-1.26	-1.40	8.16	-8.16	-5.09	0.25	0.18	-5.03
W4 ring	-13.27	-8.95	52.81	-44.49	-27.26	0.33	0.31	-27.75
W6 ring	-23.90	-15.54	84.77	-69.74	-45.41	0.36	0.32	-45.08
W6 book	-22.17	-14.82	87.24	-73.07	-45.70	0.34	0.32	-45.73
W6 prism	-18.70	-12.89	84.49	-73.79	-45.43	0.30	0.32	-46.24
W6 cage	-20.11	-13.76	87.29	-74.68	-45.70	0.31	0.30	-46.19
W20	-71.71	-56.05	321.61	-285.29	-154.67	0.31	0.28	-
W24_A	-107.57	-70.43	411.64	-357.08	-205.45	0.33	0.32	-
W24_B	-112.48	-73.11	432.60	-379.15	-223.27	0.33	0.31	-

In Figure 18 we look at dimer structures from representative small water clusters. Presenting the energies in this way conveys effectively how the model perform at the two-body level for each water clusters. Though ΔE_{es+Rep} is generally small and seldom exceeds 0.4 kcal/mol, many dimer structures have charge penetration errors as large as 1.1 kcal/mol. These positive deviations from the electrostatic interaction are nicely offset by the repulsion energies.

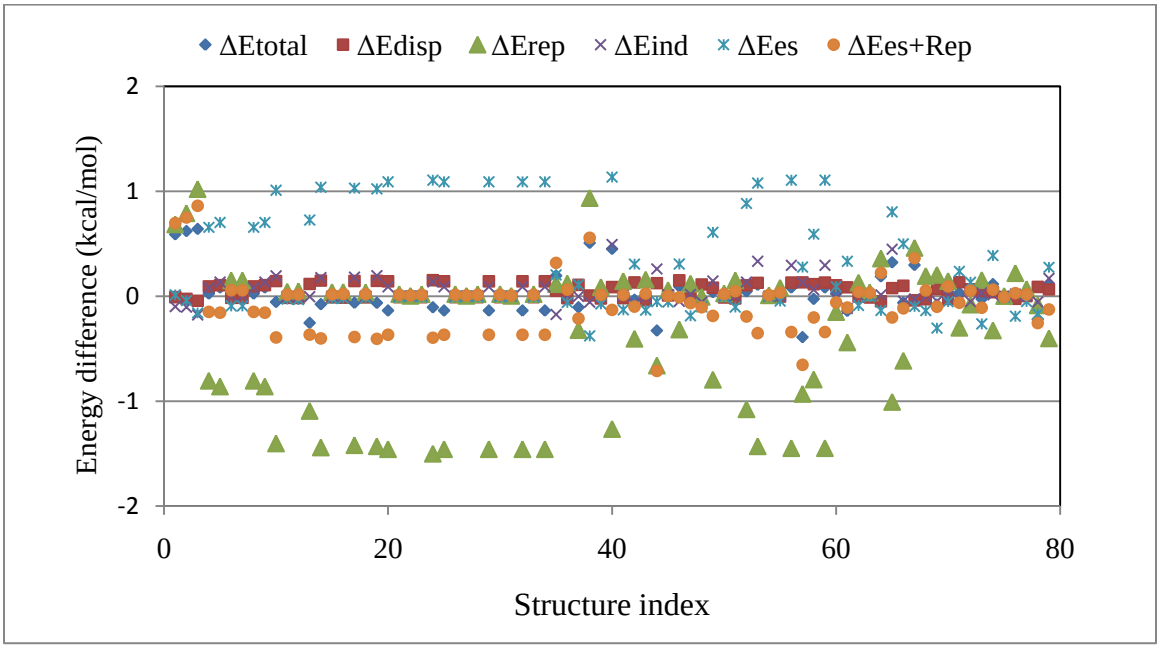

Figure 18. Energy differences between SAPT and the DPP2-F model for water dimers taken from $(H_2O)_n$ (n =3-6).

Table 11 summarizes some key contributions to the total interaction energy and their distance dependencies. [26] As can be seen, the two short-range effects come from the charge penetration and the exchange repulsions, and their balance has been excellently demonstrated in the water dimers we have examined.

Table 11. Energy components of the total interaction energy and their distance- dependency.

Fundamental component	Energy	Additive ?	R dependence	Range
Electrostatic	E^1_{es}	yes	$R^{-1}, R^{-2}, R^{-3}, \ldots$	long
	E^1_{penetr}	yes	$\exp(-aR)$	short
Induction	E^2_{ind}	no	R^{-4}, R^{-6}	long
Exchange-repulsion	$E^1_{exch-rep}$	yes	$\exp(-aR)$	short
Dispersion	E^2_{disp}	yes	$R^{-6}, R^{-8}, R^{-10}, \ldots$	long
	E^3_{disp}, E^4_{disp}	no	R^{-9}, R^{-12}	long
Higher order terms	-	no	-	-

4.6 VIBRATIONAL SPECTROSCOPY AND THE DPP2-F MODEL

The DPP2-F model produces monomer harmonic frequencies of 3945.4 and 3833.8 cm^{-1} for the asymmetric and symmetric stretches and 1649.5 cm^{-1} for the bending mode, respectively (Table 12). The results are same as those of TTM4-F and TTM2-F because they all use the Partridge–Schwenke PES/DMS. The frequencies and intensities are very close to CCSD(T)/aug-cc-pVTZ calculations.

Table 12. Vibrational frequencies (cm^{-1}) and intensities ($Debye^2$-$angstrom^{-2}$-amu^{-1}) of water monomer. CCSD(T) frequencies and intensities were calculated with CFOUR program [149].

CCSD(T)/aug-cc-pVTZ		MP2/aug-cc-pVDZ		MP2/aug-cc-pVTZ		Patridge-Schwenke	
Freq	Int	Freq	Int	Freq	Int	Freq	Int
1641.4	71.2	1622.3	67.4	1628.4	71.7	1649.5	72.8
3838.5	3.4	3803.3.0	4.1	3821.9	5.6	3833.8	4.4
3942.4	56.0	3937.5	67.0	3947.7	75.5	3945.5	62.3

Table 13 gives the frequencies and intensities obtained from *ab initio* methods and the model potential calculations. The vibrational mode with the lowest OH frequency, 3718 cm^{-1} (MP2) and 3731 cm^{-1} (CCSD(T)), corresponds to the H-bonded OH stretch (the O_4-H_5 in Figure 19). The OH bond distance increases as the hydrogen atom forms intermolecular H-bond with the oxygen atom in another water molecule. The formation of the H-bond (O_4-H_5···O_1) is characterized with the vibrational frequency redshift of the OH stretch (O_4-H_5), compared with free OH stretches (O_4-H_6) in the water molecule. The AMOEBA and the TTM4-F models both predict the decrement of the H-bonded OH frequency, but to a much greater extent: to 3664 cm^{-1} with TTM4-F and to 3630 cm^{-1} with AMOEBA. The DPP2-F model, gives a frequency of 3750 cm^{-1}, slightly higher than the CCSD(T) result.

Table 13. Vibrational frequencies (cm^{-1}) and intensities ($Debye^2$-$angstrom^{-2}$-amu^{-1}) of water dimer.

CCSD(T)/AVTZ	MP2/AVTZ		AMOEBA	TTM4-F		DPP2-F	
Freq	Freq.	Int.	Freq.	Freq.	Int.	Freq.	Int.
1647	1629.1	87.1	1594.9	1630.2	58.7	1637.0	81.4
1667	1650.1	36.7	1611.8	1677.6	58.0	1674.8	46.5
3731	3718.3	297.3	3630.4	3663.8	199.8	3749.9	144.2
3805	3813.6	11.1	3649.5	3833.2	12.4	3833.6	13.7
3891	3915.5	114.8	3725.6	3921.5	72.0	3917.4	90.1
3910	3935.1	97.5	3753.2	3942.3	96.6	3943.1	85.0

The vibrational frequencies and intensities of hexamer ring from MP2 and models are tabulated in Table 14. Due to the symmetry, the hexamer ring isomer has a simple spectrum; but it shows the influence of the H-bond on the vibrational spectroscopy of clusters. The strongest absorption (3422 cm^{-1}) in the MP2 spectrum is assigned to the H-bonded O-H stretch. It redshifts about 300 cm^{-1} compared with H-bonded OH stretch in water dimer (3720 cm^{-1}). The DPP2-F model has vibrational frequency ranking comparable to those of MP2, especially for the OH stretch regions (frequencies greater than 3000 cm^{-1}). It, however, only predicts a redshift of 114 cm^{-1}, compared with the DPP2-F dimer spectrum, much smaller than that of MP2. Among the three models, only TTM4-F has the redshift with a good agreement with MP2, while TTM2.1-F does not reflect the frequency change.

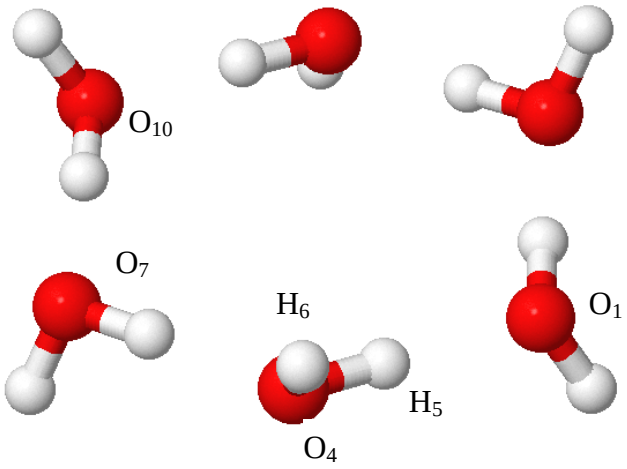

Figure 19. Structure of the water hexamer ring.

The H-bonded OH stretch is associated with a strong vibrational intensity. MP2 produces an enhancement as high as 8.8 times for hexamer ring, in contrast to in the dimer spectra, while the DPP2-F and TTM4-F both give at 6.8 times. Recall that the TTM4-F and DPP2-F improve the description of the dipole derivative of the internal OH stretch, but they still underestimate the MP2 value.

The DPP2-F model correctly predicts the vibrational hydrogen bond redshift, but it severely underestimates the magnitude of the frequency change. Since the TTM4-F model is one of the very few polarizable water models that give the characteristic redshifts of the OH stretches, it is studied along with DPP2-F model in order to elucidate the problem.

Table 14. Vibrational frequencies (cm^{-1}) and intensities ($Debye^2$-$angstrom^{-2}$-amu^{-1}) of water hexamer ring calculated from MP2 and water models.

Ring							
DPP2-F		MP2		TTM4F		TTM2.1F	
Freq	Int	Freq	Int	Freq	Int	Freq	Int
1665	0	1636	89	1664	0	1668	92
1665	0	1648	0	1667	65	1668	90
1666	115	1648	0	1667	65	1668	8
1666	115	1679	82	1676	0	1672	0
1668	46	1679	82	1676	0	1672	0
1669	0	1697	0	1685	80	1676	32
3601	0	3350	0	3379	0	3700	0
3636	986	3422	2606	3412	1391	3712	284
3636	986	3422	2606	3413	1391	3712	284
3674	0	3477	0	3437	0	3726	0
3674	0	3477	0	3438	0	3727	0
3690	73	3495	142	3446	179	3733	56
3932	246	3888	204	3955	0	3951	171
3933	0	3888	0	3955	155	3951	5
3933	0	3888	0	3955	155	3951	12
3934	174	3889	146	3957	0	3952	29
3934	174	3889	147	3957	0	3952	141
3935	0	3889	0	3958	266	3952	110

Table 15. Atom-atom distances (Å) and angle (°) of water hexamer ring isomer (S6 symmetry). The structure is optimized with each method. Index refers to Figure 19.

	O_1-O_4	O_1-O_7	O_1-O_{10}	O_1-H_5	O_4-H_5	O_4-H_6	$H_5O_1O_4$
MP2	2.7204	4.6843	5.4170	1.7343	0.9864	0.9646	1.0592
TTM4-F	2.7730	4.7040	5.4604	1.7891	0.9843	0.9523	0.7842
DPP2-F	2.7205	4.6183	5.3605	1.7459	0.9750	0.9552	1.3836
TTM2.1-F	2.7456	4.6063	5.3631	1.7742	0.9714	0.9538	0.9229

Table 15 provides the structural information of the water hexamer ring (shown in Figure 19) optimized using MP2 and flexible water models. The ring assumes S6 symmetry so that the neighboring water dimers are same and all have close-to-Cs-dimer structures. These dimers are more compact than MP2 water dimer minimum: their closest OO separation (O1-O4) is 2.72 Å, compared with 2.91 Å in MP2 dimer minimum. The OO separations calculated from the DPP2-F model gives the closest match to MP2 value, while the other two TTM models slightly predict further separations. O_4-H_5 and O_4-H_6 are the H-bonded OH and free OH, and their bond distances are strongly associated with their vibrational frequencies. The equilibrium O-H distance measured in gas phase water molecule is 0.957(8) Å, for which MP2 produces a greater value of 0.966 Å. With regards to water dimer, MP2 values for O_4-H_5 and O_4-H_6 are 0.9686 and 0.9604 Å for donor water, with the other free O-H in acceptor water (O_1H_2 and O_1H_3 in Figure 21) at 0.9623 Å. As for the hexamer ring, MP2 calculations produce a separation of 0.9864 Å for the H-bonded O_4-H_5, about 0.021 Å greater than the free stretch of O_4-H_6. The increase of the bond length clearly reflects the effect of the hydrogen bond between the hydrogen atom and other water molecule. Among the models, the TTM4-F model gives an O_4-H_5 distance at 0.9843 Å, closely matching the MP2 value, despite the fact that the bond elongation from O_4-H_6 to O_4-H_5 is 0.032 Å, more considerably greater than that of MP2.

Table 16. Vibrational frequencies (cm^{-1}) and intensities ($Debye^2$-$angstrom^{-2}$-amu^{-1}) of water hexamer cage, book and prism calculated from MP2 and the DPP2-F model.

Cage				Book				Prism			
DPP2-F		MP2		DPP2-F		MP2		DPP2-F		MP2	
Freq	Int	Freq	Int	Freq	Int	Freq	Int	Freq	Int	Freq	Int
1660	85	1639	110	1660	31	1641	30	1653	102	1636	174
1679	87	1648	73	1664	62	1644	98	1672	130	1649	36
1687	34	1661	60	1670	23	1654	69	1684	83	1655	74
1692	87	1674	45	1675	90	1664	40	1701	24	1674	16
1697	70	1682	24	1680	48	1678	22	1731	80	1690	99
1732	22	1696	34	1719	53	1707	19	1740	22	1709	49
3568	157	3224	748	3574	80	3276	162	3580	206	3197	861
3626	263	3442	639	3621	797	3346	1987	3648	241	3438	719
3646	238	3483	552	3646	275	3422	633	3668	200	3535	226
3680	124	3533	531	3666	80	3519	315	3692	102	3565	486
3689	184	3591	415	3688	216	3571	829	3715	25	3667	155
3726	45	3671	143	3710	59	3587	164	3737	66	3677	257
3768	211	3724	317	3793	254	3731	449	3761	91	3754	59
3796	217	3762	419	3922	93	3878	88	3797	170	3772	453
3921	100	3878	79	3926	91	3879	75	3807	191	3805	192
3930	88	3880	94	3929	132	3884	74	3936	108	3880	78
3941	195	3883	90	3930	95	3884	100	3941	100	3884	87
3941	26	3895	88	3934	91	3889	99	3945	121	3885	101

As shown before, the TTM4-F model gives appreciable O-H redshift associated with the hydrogen bonding, in magnitude similar to MP2, while the DPP2-F and TTM2.1-F models fail to fully produce this vibrational frequency change. It is surprising, that DPP2-F model producing a 0.02 Å increment from the free O-H to the H-bonded O-H, similar to that calculated by MP2, failed to capture the vibrational frequency change. In comparison, the TTM4-F model

produces a greater increment of 0.03 Å. It raises the question on how much information one can glean from the O-H separations to tune the model for vibrational analysis.

The DPP2-F vibrational spectra of the other three hexamer isomers are summarized in Table 16, together with the MP2 results. MP2 spectra have high-intensity H-bond stretches, and their frequencies move to below 3400 cm^{-1} and can even reach 3200 cm^{-1}. The OH stretches computed from the MP2 redshift roughly to 600 cm^{-1}. The present DPP2-F model accounts for part of the H-bond effects but fails to produce the large vibrational redshift, giving about 300 cm^{-1} frequency changes. The predicted hydrogen-bonded OH stretches are still rigid-like and not flexible enough. This happens to most of the flexible water models. The TTM4-F model, however, has an excellent description of this mode, and the author attributes that to the improved polarization part. As the DPP2-F model has a similar polarization expression, we speculate that some other factors might be equivalently important. In the meanwhile, vibrational intensities computed with the DPP2-F model are still not comparable to MP2. Though they are determined by the potential energy and forces in a sophisticated way, the induced dipole calculation still need be improved.

Table 17. Neighboring O-O separations (Å) and H-bonded O-H distances (Å) in the water hexamer ring. For index, refer Figure 19.

Struct.	W1	W2	W3_Ring	W4_Ring	W5_Ring	W6_Ring
O_1-O_4	-	2.9077	2.8038	2.7476	2.7279	2.7205
O_4-H_5	0.9659	0.9686	0.9778	0.9851	0.9867	0.9864

With many-body energies present, producing a close-form potential energy function for water clusters is very difficult. [150,151] Systematic and consistent evaluation of the performance of

different water models suffers from the choice of the training structures and the method of parameterization.

Table 17 lists the OO separations and the intramolecular O-H bond distances of neighboring water dimers in some $(H_2O)_n$ rings. As n increases from 3 to 6, these dimers assume structures increasing closer to Cs symmetry and the OO separations decrease from 2.804 to 2.721 Å. It has been discussed above that the shorter the OO separation, the larger the error in the electrostatic energy. Fortunately, for clusters with five- or six-member ring, the exchange-repulsion energy excellently offset the errors accumulated from other potential energy terms. The dimers in $(H_2O)_3$, however, deviate much from the Cs symmetry. For such structures, DPP2-F repulsion term does not balance well with the electrostatic energy and others. Clusters with three-member rings, i.e. hexamer prism, are not well described by the DPP2-F model.

The nature of the hydrogen bond in term of classical force field is not straightforward. The strength of the hydrogen bond formed is intuitively believed to be best correlated with the acidity of the hydrogen atom and the basicity of the atom with the unshared electron pair on the oxygen atom. The acidity is surely influenced by point charge bone on each charge site due to the change of the equilibrium water geometry, and also the local and global polarization effects. However, the vdW interaction (or dispersion plus repulsion) also plays a significant role. Because hydrogen bonding is distance- and angle-dependent, anisotropic potential energy is more ideal. According to the survey of the functional expressions for the repulsion, given in Table 18, so far most flexible water model rely heavily on the interaction of O-O pair, though their expressions are similar to each other.

Table 18. List of the expressions related to the dispersion and repulsion interactions used in flexible models.

Model		Interaction type	Comments
SPC-Fw	$\sum_{OO}\left[\frac{A}{r_{OO}^{12}}+\frac{B}{r_{OO}^{6}}\right]$	O-O vdW	No polarization
TTM2-F	$\sum_{OO}\left[\frac{A}{r_{OO}^{12}}+\frac{B}{r_{OO}^{10}}+\frac{C}{r_{OO}^{6}}\right]$	O-O vdW	Thole's scheme
TTTM3-F	$\sum_{OO}\left[\frac{\varepsilon}{1-6/\lambda}\left[\frac{6}{\lambda}\exp\left(\lambda\left(1-\frac{r_{OO}}{\sigma}\right)\right)-\left(\frac{\sigma}{r_{OO}}\right)^{6}\right]\right]$	O-O vdW (Buckingham exp-6)	Thole's scheme
TTM4-F	$\sum_{OO}\left[\frac{A}{r_{OO}^{16}}+\frac{B}{r_{OO}^{14}}+\frac{C}{r_{OO}^{12}}+\frac{D}{r_{OO}^{10}}+\frac{E}{r_{OO}^{8}}+\frac{F}{r_{OO}^{6}}\right]$	O-O vdW	Modified Thole's scheme
DPP2-F	$\sum_{i<j}\left[A\exp\left(-Br_{ij}\right)\right]+\sum_{i<j}\left[\frac{C}{r_{ij}^{6}}f\left(r_{ij}\right)\right]$	All-atom dispersion and ex-repulsion	Modified Thole's scheme
AMOEBA	$\sum_{i<j}\varepsilon_{ij}\left(\frac{1.07}{r_{ij}^{*}+0.07}\right)^{7}\left(\frac{1.12}{r_{ij}^{*7}}-2\right)$	All-atom Buffered 14-7 potential	Thole's scheme
POL5	$\sum_{OO}\left[A\exp\left(-Br_{OO}\right)-\frac{C}{r_{OO}^{6}}\right]$	O-O vdW	Fluctuating charge approach

It is interesting to explore to what extent the excellent prediction of the H-bonded OH stretch redshift given by the TTM4-F model is due to the its dispersion-repulsion interaction potential. We substitute the DPP2-F polarization with TTM4-F's. First, we create two models: "Model_CT", in which the charge transfer term is fit using the same approach as the DPP2-F; and "Model_NoCT", in which the charge transfer term is removed. Comparing the dimer vibrational spectra of these two models shows that explicitly including the charge transfer does not affect the vibrational redshift and the associated intensity. Secondly, in the model

"Model_NoCTCP", we remove both charge transfer and charge penetration but keep all-atom repulsion and dispersion.

Table 19. Calculated vibrational frequencies (cm^{-1}) and intensities ($Debye^2$-$angstrom^{-2}$-amu^{-1}) of water dimer. Models tested below were parameterized in the same way. See the text for details.

MP2/AVTZ				Model-CT	
freq	int			freq	int
1629.1	87.1	⇨		1634.1	67.8
1650.1	36.7			1670.9	49.0
3718.3	297.3			3760.4	169.9
3813.6	11.1			3834.1	10.6
3915.5	114.8			3920.2	101.3
3935.1	97.5			3944.0	101.4
				⇩	
TTM4F		CCSDT/AVTZ		Model-NoCT	
freq	int	freq	int	freq	int
1630.2	58.7	1647	-	1628.4	67.7
1677.6	58.0	1667	-	1670.2	49.1
3663.8	199.8	3731	-	3764.6	164.6
3833.2	12.4	3805	-	3846.1	14.7
3921.5	72.0	3891	-	3920.9	105.1
3942.3	96.6	3910	-	3957.3	103.8
				⇩	
Model-NoCTCP-vdw		Mode-NoCTCP-6		Model-NoCTCP	
freq	int	freq	int	freq	int
1633.4	61.6	1633.2	60.1	1630.2	62.7
1673.6	58.2	1659.8	55.5	1670.1	52.3
3693.7	172.8	3789.4	169.0	3745.6	182.9
3833.7	11.7	3834.8	9.5	3840.2	13.2
3920.7	74.9	3932.8	111.8	3922.8	96.4
3943.3	94.7	3944.0	101.6	3950.2	103.0

The frequencies thus-generated are quite similar to the model "Model_NoCT", suggesting that charge penetration effect does not lead to the OH stretch redshift in water dimer either. We then reduce the 8-parameter DPP2-F repulsion term to 6-parameter DPP2-R type repulsion and build the model "Model_NoCTCP_6". This change affects only the frequency of the H-bonded OH stretch, causing a 40 cm^{-1} blueshift. Frequencies of other modes are insensitive to the change of the repulsion expression. As the last step, we replace the all-atom dispersion and repulsion with the TTM4-F's polynomial expression. The model, "Model_NoCTCP_vdw", same as the TTM4-F model in most of the term, differs at (i), parameters for the vdW terms and (ii), the charge-charge damping in the TTM4-F electrostatics is removed. It produces a dimer spectrum very close to the TTM4-F, though for the hydrogen-bonded OH, the corresponding frequency is 3694 cm^{-1}, about 30 cm^{-1} higher in frequency than the TTM4-F model. The major difference in the frequencies is closely related to the parameters in the dispersion-repulsion expression, due to different fitting practices.

The vibrational spectroscopy results of these models are displayed in Table 19. Instead of increasing complexity to the model potentials, we start from the DPP2-F type potential and move toward the TTM4-F model. The evidence suggests that the success of the TTM4-F model in predicting the vibrational redshift of water clusters is somehow associated with the OO type potential used in the TTM4-F, instead of all-atom asymptotic repulsion and dispersion. Given the fact that adding more energy terms leads to improved potential energy calculation, this might seem counterintuitive that the vibrational spectrum does not improve much.

In Figure 20 we list representative flexible and rigid (in parentheses) water models studied. The electrostatic interaction of non-polarizable models, i.e. SPC and TIP4P, are gradually partitioned into energy components such as the electrostatic, charge penetration,

polarization, and charge transfer in the polarizable water model DPP2-F, as we move down from the top. In the meanwhile the nonbonded vdW interaction is separated into dispersion and repulsion part. Excluding the intramolecular potential, we place attractive interactions on the left-hand side, whereas the repulsive interactions on the right-hand side. The discussion is limited to induced dipole polarizable models, though one needs be aware of the availability of other approaches. The figure clearly shows that there is only one "repulsive" contribution in all of these models, some are in the form of vdW, and others are the repulsion potential term. The increasing complexity is exclusively associated with the attractive interactions.

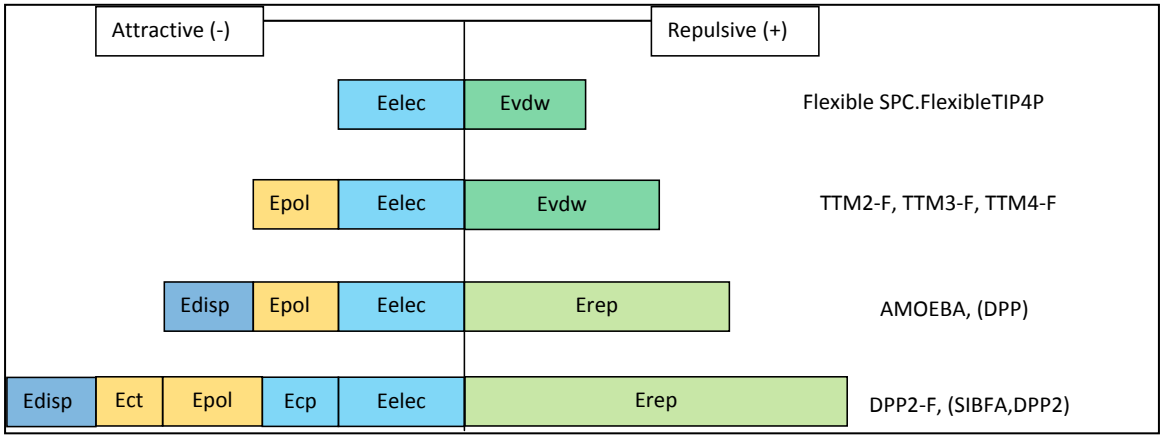

Figure 20. Energy terms employed in representative flexible water models. The models in parentheses are rigid body model. Intramolecular energy potential is neglected.

The point charges used for the electrostatics do not differ too much in most polarizable models, so the magnitude of the electrostatic energies, which is directly related to point-charges, is fairly stable among different point-charge water models. The polarization energies reported from different models, interestingly, vary but to a modest degree. The charge transfer and charge penetration effects are somehow arbitrary. This figure gives a rough sense of magnitude of these

energy contributions. The repulsive energies from the models at the bottom can be several times larger than those in the models on the top or in the middle. Surprisingly, similar functional forms are being used for this term in all these models.

Though the models on the bottom are more mathematically appealing, make more physical sense, and also on the right direction, performance for modeling water systems may not justify the extra efforts. We hypothesize that the error canceling in the models on the top side can significantly contribute satisfactory modeling.

5.0 CONCLUSION AND FURTHER DIRECTION

DPP2-F, a polarizable flexible water model, is presented in this work. The potential function consists of an intramolecular potential and six intermolecular interaction components, namely electrostatic, charge penetration, polarization, charge transfer, dispersion and exchange-repulsion. The intramolecular flexibility is achieved through the predetermined water molecule PES reported by Partridge and Schwenke. The partial point charges for hydrogen and *M*-site are transformed from their DMS subroutine. About three hundred water dimers have been analyzed using SAPT energy decomposition scheme and the respective energy components are used as reference data. All intermolecular energy terms are fit, to SAPT components, except the exchange repulsion, which is determined by fitting the total potentials to the MP2 interaction energies.

The model produces an excellent molecular polarizability surface through employing the geometry dependent atomic polarizabilities and the modified exponential induced dipole damping scheme. It also gives an improved dipole derivative of the dimer hydrogen-bonded OH stretch. The DPP2-F electrostatics and exchange-repulsion, for many water dimers, show appreciable deviations from the SAPT values, but these deviations tend to offset. The nice balance leads to an excellent description of interaction energies of water clusters.

When used to study vibrational spectroscopy of water clusters, the DPP2-F model correctly predicts vibrational redshift of the H-bonded OH stretch that arises from the formation of hydrogen bond, but underestimates the magnitude of the frequency change and associated vibrational intensity. By tracking the success of another flexible polarizable model TTM4-F in predicting the frequency redshift, we suggest that the exchange repulsion play an important role in the model development. The major issue with the DPP2-F model is that the repulsion part performs poorly for some structures and leads to too rigid hydrogen-bonded OH bonds, because the repulsion term is parameterized to absorb the errors from the electrostatic energies. Results from the group indicate that the electrostatic deviations from SAPT comes most from the three-point charge representation and introducing seven or nine point charges greatly improve the electrostatic energies. The further work will integrate the multiple charge approach into the flexible model. [152]

APPENDIX A

ACCURATE ENERGY CALCULATION FOR WATER CLUSTERS ANIONS

Water clusters have varying abilities to bind free electrons. As a rule of thumb, within the context of the Born-Oppenheimer approximation, water cluster can bind an excess electron to form so called dipole-bound anion if the collective dipole moment exceeds a critical value about 1.62 D. [153] However, some water clusters with near zero net dipole moments are also able to bind an excess electron, through dispersion interactions. It has been widely accepted that dispersion-type interaction between the excess electron and the tightly-bound valence electrons of water makes a considerable contribution to the electron binding energy (EBE) for certain clusters. Accurate *ab initio* calculation of excess electron-water clusters interaction requires high-level electronic correlation methods and carefully-chosen large basis set. [154]

Energies of water clusters anions, is the energy of neutral water cluster minus the contribution of EBE.

$$E_{(H_2O)_n^-} = E_{(H_2O)_n} - EBE \qquad (54)$$

The more positive the EBE, the higher the ability that water clusters have in binding the excess electron. Though water cluster tend to form as more hydrogen bond in the network as possible, the strong excess electron distortion is also an important consideration.

During the past decade, the Jordan group has been actively working on developing excess electron-water interaction potential. The quantum Drude oscillator approach was formulated, [155, 156] modeling the dynamical response of the electrons of the water monomers to the excess electron are by associating each monomer with a classical Drude oscillator. EBEs of the excess electron can be obtained by solving one-electron Schrödinger equation. The Drude model Hamiltonian, H_{Drude} ,is given as follows in terms of atomic units,

$$H_{Drude} = -\frac{1}{2}\nabla^2 - \sum_{i=1}^{N_{charge}} \frac{q_i}{r_i} + V_{rep}\left(a_{rep}\right) + \sum_{i=1}^{N_{OSC}} \left[-\frac{\hbar^2}{2m_D}\nabla_{osc}^2 + \frac{1}{2}k_D \sum_{j=1}^{3} R_{ij}^2 \right] + q_D \sum_{i=1}^{N_{OSC}} \frac{r_i \cdot R}{r_i^3} f\left(r_i, b_{e-Drude}\right) \quad (55)$$

It includes the excess electron kinetic energy, the interaction of the excess electron with the point charges, the short-range repulsion and exchange interactions between the excess electron and the valence electron distributions of the monomers (V_{rep}), kinetic and potential energies of Drude oscillators, and the coupling between the excess electron and the Drude oscillators. Detailed discussions can be found in literature. [157] The approach for evaluating the energy associated with H_{Drude} , referred to as Drude/CI method, [158] and is the single-plus-double-excitation configuration interaction (CI) approximation, where the double excitations are restricted to configurations that involve simultaneous excitation of the excess electron and of one of the Drude oscillators.

The Hamiltonian of the Drude model contains two free parameters, a_{rep} and $b_{e-Drude}$, in the repulsive potential V_{rep} and in the electron-Drude oscillator coupling term, respectively. The

a_{rep} parameter scales the repulsive potential and is chosen so that for water hexamer AA (Figure 1), the EBE from the model potential calculation without the Drude oscillators matches the Koopmans' theorem (KT) [159] EBE from a large basis set *ab initio* Hartree-Fock calculation on the neutral molecule. The $b_{e-Drude}$ parameter is used to tune the damping of the electron-Drude coupling term and is chosen so that the EBE of the water hexamer AA, calculated using the Drude/CI method, reproduces that from large basis set *ab initio* CCSD(T) calculations.

The CCSD(T) EBEs of the water clusters were calculated with Molpro, [160] using Dunning's aug-cc-pVDZ basis set. [128] A floating site, with five S and four P diffuse basis functions, unless explicitly specified, is placed on the center of mass. The basis function exponents decrease by 3.32.

The Polarization Model (PM3) evolved from the quantum Drude approach. Instead of turning to Drude oscillators for simultaneous excitations of oscillators and excess electron, the correlation effects between the excess electron and the electrons of water monomers are recovered via a polarization potential function V_{pol} , associated with each monomer. The Hamiltonian H_{PM3} is thus simplified to:

$$H_{PM3} = -\frac{1}{2}\nabla^2 - \sum_{i=1}^{N_{charge}} \frac{q_i}{r_i} + \sum_{i=1}^{N_{dipole}} \frac{\mu_i \cdot r_i}{r_i^3} f(r_i) + V_{rep}(a_{rep}) + \sum_{i=1}^{N_{pol-site}} V_{pol}(r_i, b_{pol}) \qquad (56)$$

which includes electron kinetic energy, excess electron-point charge, excess electron-induced dipoles interaction, repulsive potential and polarization potential terms.

The repulsive core scaling factor is the same as that in Drude/CI model, and has been determined. The other parameter $b_{pol.}$ appears in the polarization potential and is determined in

the same way as $b_{e\text{-}Drude,}$ i.e., by matching the AA hexamer's CCSD(T) EBE. To avoid the numerical integration, $V_{pol}(r)$ with known b_{pol} is then fit to six d-type Gaussian functions.

3.3. Results and Discussion.

Table 20 lists the parameters for the Drude/CI and PM3 approaches. Two sets of parameters are used, one is fit to *ab initio* values of the rigid AA hexamer and the other set is fit to the *ab initio* EBE of flexible AA hexamer. Since the excess electron-water potential is based on the rigid neutral water model, parameterizing it to flexible water configuration provides a simple way to approximate the EBEs of the water clusters with relaxed monomers.

Table 20. Parameters for the excess electron-water interaction potentials. Units for *ab initio* EBEs of KT and CCSD(T) are meV.

		Drude/CI		PM3		
		Flex	Rigid	Rigid	Flex	Original
ab initio	KT	259.1	232.7	232.70	259.1	261
	EBE/CCSD(T)	466.90	422.4	422.40	466.9	470
Parameter	a_{rep}	9.24300	6.38700	6.38700	9.24300	6.32100
	$b_{e-Drude}$	0.31650	0.46910	-	-	-
	b_{pol}	-	-	0.067012	0.054791	0.091460

The EBEs of six water hexamer anions [157] calculated from the model, using the two sets of parameters, are compared with available CCSD(T) results in Figure 21. Flexible structures generally have EBEs about 10-15% higher than their rigid counterpart, due to the preferable accommodation of the excess electron from the adjusted bond distances and angles.

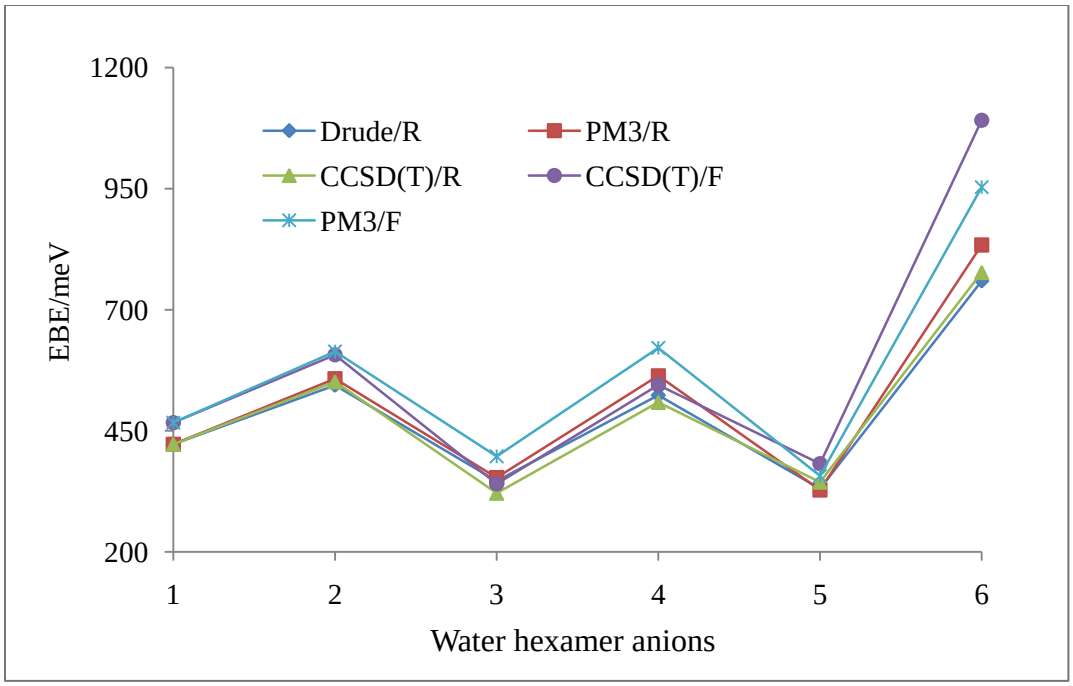

Figure 21. Comparison of EBEs of water hexamer anions. R and F refer to rigid and flexible set of parameters for Drude/CI and PM3 (polarization model) or structures for CCSD(T). These water anion structures are optimized at the MP2 level.

Since the PM3 model can be derived from the Drude/CI model under the adiabatic approximation, its accuracy then should be assessed on how close it can match Drude/CI model. Note that PM3 allows much faster evaluation of the energies and gradient, and is not as restricted by the system size as Drude/CI. [161]

An updated version of the "Table 1" [157] is give as Table 21. Drude/CI approach has proved to give very satisfactory EBEs for the small water clusters studied. Accurate *ab initio* results for large water cluster anions were not available until very recently. At the time of writing, these approaches are being evaluated by the group. With the results available, the Drude/CI approach provides a very reliable way to predict the binding of excess electrons to the "reasonable" neutral water clusters.

Table 21. Dipole moments (debye) and Electron Binding Energy (meV) contributions for various $(H_2O)_n^-$ clusters.

		Drude						
	dipole/D	Es+rep	ind	disp	PT2	CI	PM3	CCSD(T)
W2	4.0	6.1	0.4	8.4	14.9	33.8	34.4	41.1
6A	9.4	184.2	25.4	116.0	325.6	422.4	422.4	422.4
6B	8.5	201.3	40.4	167.2	408.9	544.0	557.6	551.2
6C	9.2	136.3	18.8	92.5	247.7	346.3	353.5	321.2
6D	0.0	62.2	49.1	260.2	371.5	523.6	563.7	508.9
6E	12.2	168.1	12.4	85.1	265.6	330.6	327.9	344.0
6F	0.1	-4.1	0.0	8.9	4.8	759.4	833.7	777.0
20A	24.9	567.3	80.1	226.1	873.5	1012.7	1044.0	-
20B	18.8	432.4	76.9	205.4	714.6	852.0	883.4	-
20C	14.5	252.2	57.6	168.3	478.1	617.1	647.4	-
20D	14.2	183.7	39.7	136.3	359.7	497.0	527.7	-
20E	2.0	-4.2	0.0	1.4	-2.8	26.9	44.6	-
20F	0.0	7.0	0.6	79.0	86.6	315.4	350.0	-
24A	0.0	-5.1	0.0	1.0	-4.1	679.1	916.6	-
24B	0.0	-4.9	0.0	1.3	-3.5	56.2	87.7	-
24C	0.0	-4.9	0.0	1.3	-3.6	319.4	530.5	-
24D	0.0	-4.8	0.0	1.7	-3.1	904.0	1165.7	-
24E	0.0	-2.7	0.0	12.8	10.2	195.9	221.3	-
W45A	10.3	170.7	1286.7	1170.2	2627.7	2308.7	2708.5	-
W45B	19.2	689.3	181.8	327.4	1198.5	1391.3	1475.5	-

For the twenty six clusters, the results of PM3 generally match those from Drude/CI. The PM3 method, however, tends to systematically overestimate the EBEs compared with Drude/CI, and this is more apparent when EBEs are greater than 1000 meV and the water clusters strongly bind the excess electron. It remains unclear why this overestimation happen, though we speculate that Drude/CI gives correct answer but PM3 deviates from it.

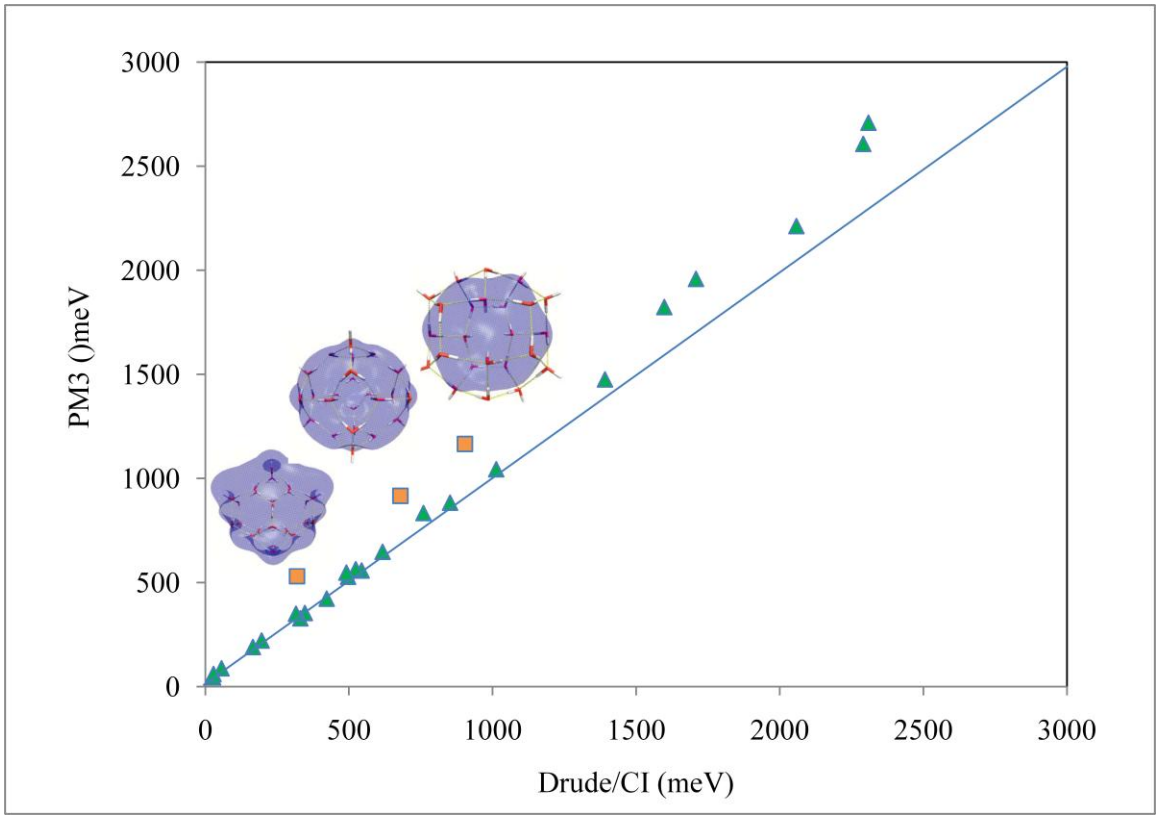

Figure 22. Electron-binding energies (EBEs) of the $(H_2O)_n^-$ n =2–45 clusters calculated using the PM3 and the Drude/CI approach. Those water clusters with EBEs greater than 1200 meV have sizes greater than n = 24. The three colored structures, in the increasing order of the EBEs, are W24C, W24A, and W24D.

Although large water clusters may bind the excess electron weakly, larger EBEs are closely attributed to the greater size of the water clusters. The three colored structures on the Figure 22, in the increasing order of the EBEs, W24C, W24A, and W24D, have a more pronounced divergence between PM3 and Drude/CI. W24A attracts most of our interest because of its high symmetry.

Considering the prohibitive cost of computing the EBE of W24a anion, we have extracted $(H_2O)_8^-$, $(H_2O)_{12}^-$ and $(H_2O)_{16}^-$ clusters from the W24A and examined their EBEs given by the PM3 and Drude/CI. For the W24A and its sub-clusters, the total dipole moments are all zero.

The Drude/CI method predicts an EBE of 670 meV for W24A, while PM3 gives a greater number of 917 meV. The strong ability to bind the excess electron comes mainly from the dispersion effect. Surprisingly, the issue inherent in W24A, the one with a 336 meV difference between PM3 and Drude/CI to an EBE in the magnitude of 670 meV, does not happen in these smaller sub-clusters.

In the hope of modeling the problem in W24A, we create a cubic-type $(H_2O)_8^-$.The fictitious structure has eight oxygen atoms sitting on the vertexes of a cube and one hydrogen atom of each water molecule pointing toward the diagonal oxygen atom. The dimension of the cluster is controlled by adjusting the side length of the cube. The configuration was similar to the water hexamer Kevan structure. [162] As the dimension of the cube reduces, and the clusters become more compact, the excess electron is being bound by the cluster increasingly stronger. As shown in Figure 26, the CCSD(T) EBE jumps from 890 meV to 1875 meV as the cube side length decrease from 5 Å to 2.5 Å. The large EBEs of the cubic $(H_2O)_8^-$ are "man-made" and the clusters are very high in energy. Shall we look at the EBE-size plot in Figure 1, the measured cluster with EBEs as high as 1.8eV has around 50 water molecules.

When the cube side length is no less than 3 Å, Drude/CI gives electron binding energies very close to the CCSD(T) method. PM3, not surprisingly, overestimates the EBE and the absolute deviation of the EBE is appreciable for the cluster at 3 Å. As we reduce the dimension of the cube to 2.5 Å, we have a Drude/CI EBE of 1170 meV, 700 meV lower than that of CCSD(T). When the cube side length decreases below 3 Å, the Drude/CI approach no longer reliably describe the excess electron-water interaction. The failure of Drude/CI approach there is not hard to understand, given the limitation of the point-charge model in treating short-range effects. It remains unclear why the DVR approach gives a close agreement with the Drude/CI.

Figure 23 also indicates that the polarization model using DVR basis set, closely reproduces the Drude EBEs. DVR and Gaussian basis function are equivalent when both are complete and flexible enough for the water cluster anion, the former one is more promising in studying electron-water interaction and used by many groups.

We conclude this session by rethinking of the W24A anion: what causes the appreciable difference in the EBE between the Drude/CI and PM3 approaches. Many factors, such as the point-charge electrostatics, induced dipole iteration scheme, and lack of mutual polarization between excess electron and water, [163]all can be the causes. In spite of the problem in the case of W24A, the agreement between the Drude method and polarization model EBEs is most encouraging.

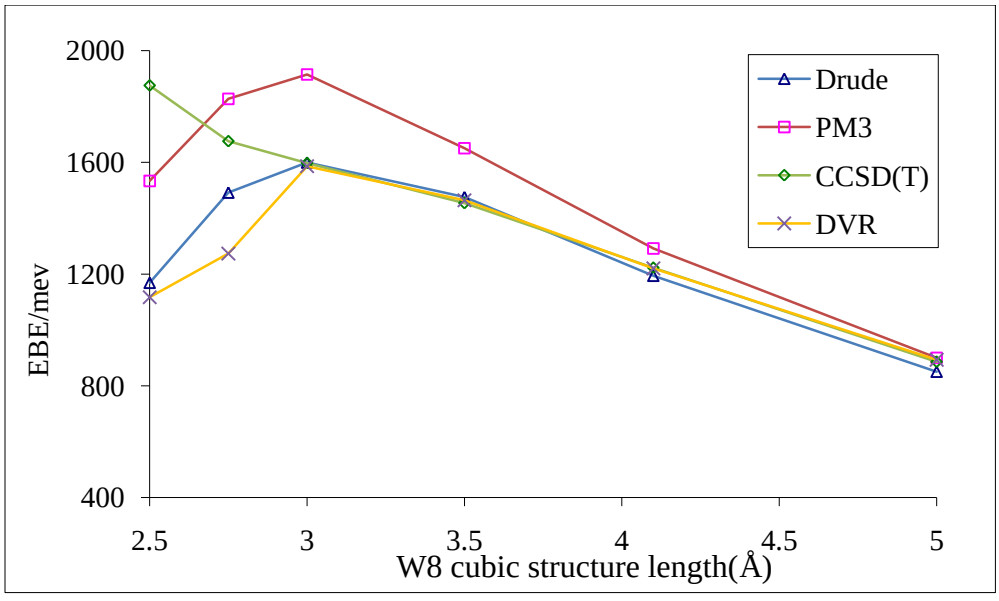

Figure 23. EBEs of the cubic water octamer anion with different side lengths.

APPENDIX B

VIBRATIONAL SPECTROSCOPY OF PROTONATED WATER DIMER $(H_5O_2)^+$

I have conducted the Car-Parrinello MD simulation of protonated water dimer and the results have been published in: *J. Phys. Chem. A* **2009**, 113, 7671–7677.

Calculation of the Vibrational Spectra of $H_5O_2^+$ and Its Deuterium-Substituted Isotopologues by Molecular Dynamics Simulations

Martina Kaledin*

Department of Chemistry and Biochemistry, Kennesaw State University, Kennesaw, Georgia 30144

Alexey L. Kaledin and Joel M. Bowman

Department of Chemistry, Emory University, Atlanta, Georgia 30322

Jing Ding and Kenneth D. Jordan

Department of Chemistry, University of Pittsburgh, Pittsburgh, Pennsylvania 15260

In this work, we present infrared spectra of $H_5O_2^+$ and its $D_5O_2^+$, $D_4HO_2^+$, and $DH_4O_2^+$ isotopologues calculated by classical molecular dynamics simulations on an accurate potential energy surface generated from CCSD(T) calculations, as well as on the BLYP DFT potential energy surface sampled by means of the Car-Parrinello algorithm. The calculated spectra

obtained with internal energies corresponding to a temperature of about 30 K are in overall good agreement with those from experimental measurements and from quantum dynamical simulations.

I. Introduction

Protons (H^+) and hydroxide ions (OH^-) exhibit anomalously high mobility in aqueous media compared to other ions such as sodium (Na^+) and chlorine (Cl^-),[164] indicating that their transport occurs via mechanisms other than simple ionic diffusion. The nature of the excess proton and its transport mechanism and spectroscopic signatures in aqueous solutions have been the subject of extensive debate for many years.[165,166,167] Much of this discussion has centered around H_3O^+ and $H_5O_2^+$ that are the ion cores of the so-called Eigen [168] and Zundel [169] forms of the cations, respectively. The Eigen designation is generally reserved for the $H_9O_4^+$ entity with the H_3O^+ hydronium core. Fluctuations between these species mediate the Grotthuss mechanism [170] for proton transport.

Over the past few years, vibrational spectra have been obtained for mass-selected inert gas atom tagged $H^+(H_2O)_n$ ions with *n* ranging from 2 to 8. [171,172,173,174,175,176,177,178] These spectra have provided evidence for both Zundel and Eigen ions, as well as for species whose spectra are intermediate between those of Eigen and Zundel ions.[176] Particularly noteworthy is the appearance of a doublet in the region (~1000 cm^{-1}) of the shared proton stretch in the measured vibrational predissociation spectra of the $H_5O_2^+$ Ne and $H_5O_2^+$ Ar Zundel ions.[177] This doublet has proven especially challenging theoretically,[177,179] and it was first successfully characterized theoretically by Meyer and co-workers [180,181] using the multiconfigurational time-dependent Hartree (MCTDH) method[182] and accurate *ab initio* potential energy and dipole moment surfaces

from Bowman and co-workers.[183] These calculations revealed that the doublet arises from a resonance between the shared proton O-H-O stretch and a combination state involving one quantum of the O-O stretch and two quanta of the water wag.

Unfortunately, it is difficult to apply the MCTDH method to larger protonated clusters due to the prohibitive computational costs of generating accurate potential energy surfaces from *ab initio* calculations and of doing the quantum dynamics calculations. As a result, there is considerable interest in establishing the applicability of more approximate methods for calculating the vibrational spectra of $H^+(H_2O)_n$ clusters and other highly anharmonic species. This leads naturally to the question as to whether spectra calculated from the dipole autocorrelation function evaluated using "*ab initio* molecular dynamics" (AIMD) simulations can recover the key spectral features of such challenging systems. In the AIMD approach the energies, forces, and dipole moment functions for the sampled configurations are calculated "on the fly" using electronic structure methods. This approach has been used in several prior studies to obtain the vibrational spectrum of $H_5O_2^+$.[179,184,185,186], However, with one exception, these simulations were performed at internal energies, corresponding to temperatures of 80 K or higher, which are likely much higher than those of the Ne or Ar atom tagged clusters studied experimentally. The calculated spectrum reported in ref 186 does not provide clear-cut evidence of the doublet in the region of the shared proton asymmetric stretch, while that reported in ref 184, calculated at an internal energy content corresponding to T = 300 K, displayed considerable structure in this region. In a recent paper, Kim and co-workers reported the results of AIMD simulations of $H_5O_2^+$ carried out at an internal energy corresponding to T = 50 K.[185] The resulting IR spectrum does display a doublet in the vicinity of the shared proton. It should also be noted that MD simulations carried out at an internal energy corresponding to T = 100 K on an *ab*

initio CCSD(T) potential energy surface [183] do display a doublet in the shared proton stretch region.[180] In the present study, we report vibrational spectra of $H_5O_2^+$ and several of its D-substituted isotopologues, calculated using AIMD simulations as well as using MD simulations on the CCSD(T) potential energy and MP2-level dipole moment surfaces of Bowman and co-workers.[183] Internal energies corresponding to temperatures as low as 30 K are considered. It is demonstrated that for T = 30 K both sets of classical simulations give vibrational spectra, including the shared proton stretch region, in overall good agreement with experiment.

II. Computational Details

The AIMD simulations were carried out using the Car-Parrinello (CPMD) algorithm,[187,188] together with the BLYP density functional method,[189,190] the norm-conserving Troullier-Martins pseudopotential,[191] and a plane-wave cutoff of 120 Ry. Cluster boundary conditions were applied using the method of Martyna and Tuckerman.[192] A time step of 3 au (~0.073 fs) and a fictitious electron mass of 400 au were employed. The production runs were carried out for 170000 steps in the microcanonical ensemble, following 30000 step equilibration periods using the Nosé-Hoover thermostat.[193,194,195] Rotational corrections [196]were applied every 20 steps. The first 20000 steps of the microcanonical trajectories were discarded, and the remaining steps were used to compute average temperatures and spectra. The CPMD simulations on $H_5O_2^+$ were carried out for internal energy contents corresponding to temperatures ranging from 1 to 200 K, while those for the various D-substituted isotopologues were carried out only for internal energies corresponding to T = 30 K. The T = 1 K simulations were carried out as a check on possible errors caused by the use of the 400 au fictitious electron mass.[197] The IR

absorption spectra were calculated from the Fourier transform of the dipole-dipole time correlation function, applying the harmonic quantum correction factor.[198,199]

$$Q = \frac{\beta\hbar\omega}{1-\exp\left[-\beta\hbar\omega\right]} \quad (58)$$

Due to the considerable computational effort required to perform the CPMD simulations, each reported spectrum was obtained by averaging over one long-time trajectory. The CPMD simulations were carried out using the CPMD program (version 3.11.1).[200] Given the importance of both diagonal and off-diagonal anharmonicities in the vibrational spectrum of $H_5O_2^+$, it is not clear a priori whether the BLYP functional describes the potential energy surface (PES) sufficiently accurately to properly account for the Fermi resonances observed in the experimental vibrational spectrum. For this reason, MD simulations on $H_5O_2^+$ and its D-substituted isotopologues were also carried out using the CCSD(T) PES and MP2 dipole moment function of Bowman and co-workers. In the ensuing discussion this approach will be referred to as MD/CCSD(T).

The MD/CCSD(T) simulations of $H_5O_2^+$ and its D-substituted isotopologues were carried out in the NVT ensemble with internal energies corresponding to T = 30 and 50 K. For each temperature, 100 separate MD simulations were run. The initial velocities were sampled from the usual thermal distribution. Metropolis sampling was employed to select the initial geometries. In this sampling 200 steps were sufficient to obtain the thermal distribution for the initial geometries, as reported in our previous paper.[179] A total of 100 (real-time) trajectories with these initial conditions were carried out for 16 ps, employing a time step of 0.25 fs. To achieve convergence of the phase space integration with only 100 trajectories, the dipole correlation function from each trajectory was also time averaged over the length of the propagation as

discussed in ref 16. The resulting spectra yield a 2 cm^{-1} resolution. Additional details of the calculation of the spectra for the MD/CCSD(T) procedure can be found in section 2.1. For comparative purposes, the vibrational frequencies of $H_5O_2^+$ and its D-substituted isotopologues (Table 22) and intensities were also calculated in the harmonic approximation using the potential energy and dipole moment surfaces of Bowman and co-workers.[183]

Table 22. Harmonic vibrational frequencies (cm^{-1}) of $H_5O_2^+$ and its D-Substituted isotopologues. Computed using the CCSD(T)-determined potential energy surface.[179]

$H_5O_2^+$	$D_5O_2^+$	$DH_4O_2^+$(int)	$DH_4O_2^+$(ext)	$D_4HO_2^+$(int)	$D_4HO_2^+$(ext)
170	121	170	156	121	131
339	248	311	307	261	257
471	339	444	447	350	363
532	389	488	482	407	423
554	420	547	534	423	439
630	593	626	627	593	608
861	627	692	846	786	647
1494	1084	1173	1449	1219	1104
1574	1145	1244	1487	1303	1158
1720	1257	1675	1663	1522	1280
1770	1298	1707	1740	1584	1508
3744	2694	3743	2753	2695	2699
3750	2703	3750	3747	2703	2752
3832	2811	3832	3794	2811	2811
3832	2811	3832	3832	2812	3793

III. Results and Discussion

A. Effects of Temperature on the Calculated Spectra.

Before presenting the results of this subsection, it is worth noting some fundamental differences between classical and quantum calculations of spectra. At T = 0 K the former reproduce harmonic spectra in both line positions and intensities, whereas exact quantum spectra can (and generally do) display significant deviations from harmonic spectra due to diagonal and coupled anharmonic effects. As the temperature increases classical spectra also differ from

harmonic spectra due to the classical response to anharmonic effects. In general, the expectation is that classical and quantum spectra do not describe these anharmonic effects equivalently; however, the dearth of comparisons between exact quantum and classical spectra at nonzero temperatures precludes making quantitative statements about their differences. Thus, when comparing classical, quantum, and experimental spectra, especially at low temperatures, it is important to keep this in mind.

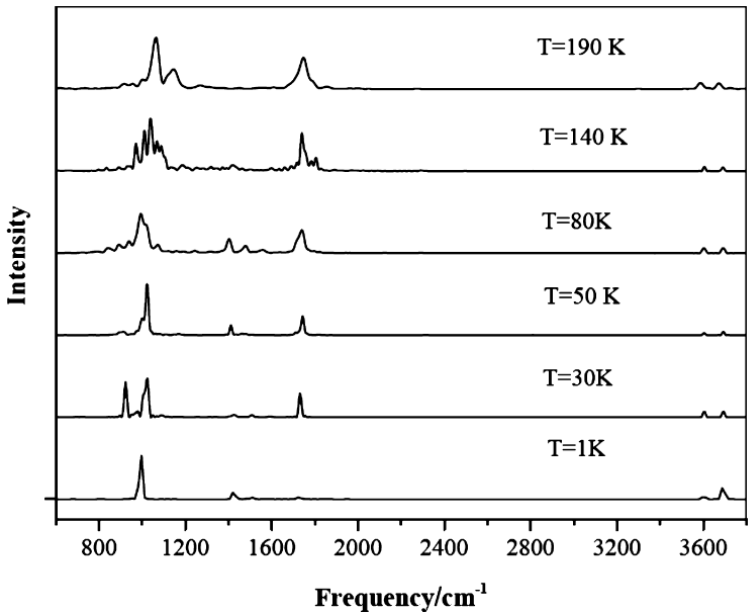

Figure 24. CPMD IR spectra of $H_5O_2^+$ for temperatures ranging from 1 to 200 K.

Figure 24 reports the IR spectra of $H_5O_2^+$ calculated using the CPMD method for temperatures ranging from 1 to 200 K. The energy scale for these spectra has been multiplied by 1.029, which brings the energies of the calculated peaks in the T = 1 K spectrum into close agreement with the harmonic spectrum calculated using the Hessian and the same electronic structure method. This scaling approximately compensates for the unphysical red shifts caused by the use of a 400 au effective electron mass and is applied to all CPMD spectra reported in this

paper. In contrast to the spectrum calculated for T = 1 K, that calculated for T = 30 K gives a pair of lines of comparable intensity near 1000 cm^{-1}, with a splitting of about 100 cm^{-1}, in close agreement with the experimental predissociation spectrum of $H_5O_2^+$ Ne,[177] which is reproduced in Figure 26. At T = 50 K the doublet in the calculated spectrum is still discernible although the lower energy feature has an intensity less than 1/10 that of the higher energy feature. As the temperature is increased further, the doublet structure disappears, and the calculated spectrum evolves into a broad structure spanning about 200 cm^{-1}. Although the temperatures of the clusters characterized experimentally are not known, it is clear that the Ne tagged cluster must be very cold, otherwise the Ne atom would be lost prior to photon absorption. With the caveats of the first paragraph of this subsection in mind, the results presented in Figure 24 suggest that the temperature of the Ne tagged $H_5O_2^+$ cluster is near 30 K, a conclusion also recently reached by McCoy and co-workers (for the Ar atom tagged cluster). [201] These results suggest that the failure of previous AIMD simulations to provide clear-cut evidence for a doublet near 1000 cm^{-1} is a consequence of the much higher temperatures employed.

Figure 25 displays the IR spectra of $H_5O_2^+$ calculated from MD/CCSD(T) simulations at T = 30 and 50 K. Overall, the resulting spectra are in close agreement with those obtained at the same temperatures using the CPMD method with the BLYP functional. The main difference between the spectra calculated using the two MD approaches is that in the MD/CCSD(T) simulations the doublet near 1000 cm^{-1} occurs about 70 cm^{-1} more to the red and, thus, in poorer agreement with experiment. However, it should be noted that the harmonic frequency for the shared proton stretch is about 100 cm^{-1} lower for the CCSD(T) PES than for the BLYP PES (861 vs 982 cm^{-1}, respectively) and that anharmonic corrections increase the shared proton stretch frequency by over 100 cm^{-1}. [184] Thus, it appears that the better agreement with experiment of the

frequencies in the shared proton stretch region of the spectrum calculated using the CPMD method is fortuitous, being the result of the DFT calculations with the BLYP functional giving too high a value for the harmonic frequency of the shared proton stretch.

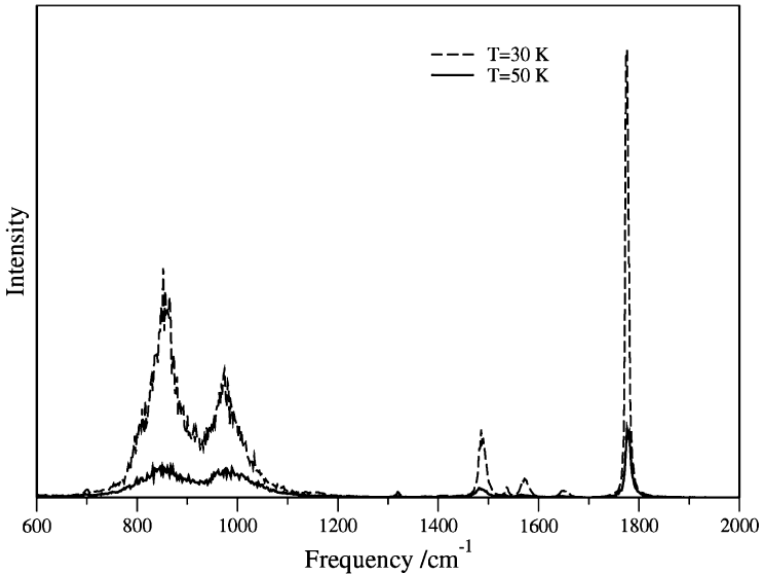

Figure 25. Temperature dependence of the MD/CCSD(T) IR spectrum for $H_5O_2^+$, T = 30 K (dashed line), T = 50 K (solid line).

The relative intensities and widths of the two features comprising the shared proton doublet are different in the two MD approaches. For example, for the T = 30 K simulations, the two peaks are of comparable intensity in the CPMD simulations, whereas the lower energy peak is about twice as intense as the higher energy peak in the simulations using the CCSD(T) PES. At T = 50 K the two peaks are of comparable intensity in the MD/CCSD(T) simulation but differ by over an order of magnitude in intensity in the CPMD simulations. We note further that the doublet in the region of the shared proton stretch is still discernible in the spectrum obtained from the MD/CCSD(T) simulations at T = 100 K and reported.. The differences in the widths are most likely due to the fact that the CPMD calculations are microcanonical whereas the

MD/CCSD(T) calculations are canonical; however, differences in the electronic description of the H^+ coupling could also contribute.

In spite of the shortcomings, discussed above, the success of the MD simulations at recovering the shared proton doublet is most encouraging, as is the overall good agreement between the results of the two MD approaches since the CPMD method can be applied to much larger clusters than can MD simulations on high-quality predetermined *ab initio* potentials. In the remainder of the paper, we focus on the results obtained from the T = 30 K simulations, although, on the basis of the MD/CCSD(T) results for $H_5O_2^+$, it is possible that the inert gas atom tagged clusters studied experimentally are somewhat warmer than this.

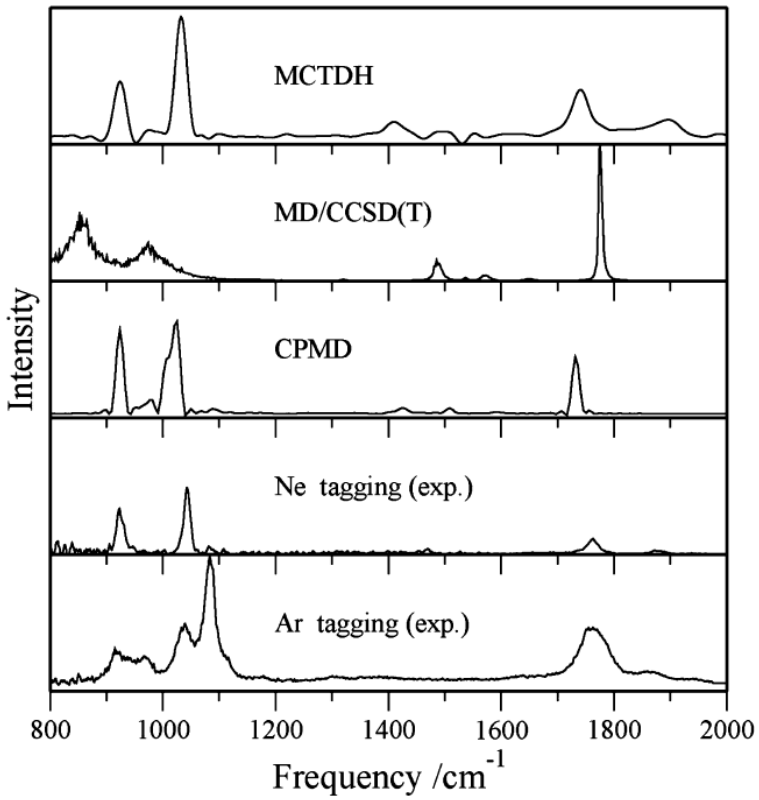

Figure 26. Comparison of the $H_5O_2^+$ MD/CCSD(T), CPMD, and MCTDH (0 K) [180,203] simulations of the IR spectrum and $H_5O_2^+$RG (RG) Ar, Ne) experimental observations.[201,202,177]

B. Comparison of Measured and Calculated Spectra.

In addition to $H_5O_2^+$ Ne and $H_5O_2^+$ Ar, experimental predissociation spectra have also been reported for the Ar tagged complexes of $D_5O_2^+$, $D_4HO_2^+$, and DH_4O_{2+} (in this case only in the spectral region above 2200 cm^{-1}). [201,202] In the latter two cases, multiple isomers are possible as the minority species (H or D) can be located in the shared position between the O atoms or in one of the free hydroxy sites and, in addition, the Ar atom can bind to any of the free OH (OD) groups. Earlier theoretical analyses [201] have shown that, due to zero-point energy (ZPE) differences, the energetically favored isomers are $D_4HO_2^+$(int) and $D_4HO_2^+$(ext), where the "int" and "ext" labels indicate the isomers with the minority species (H or D) located in the shared proton position and as a free OD (OH), respectively. In other words, in the mixed isotopologues, the vibrational zero-point energy contributions favor locating a H atom in the shared proton site.

i. Free OH (OD) Stretch Region of the Spectra.

The experimental vibrational predissociation spectrum of $H_5O_2^+$ Ne has two strong transitions split by about 100 cm^{-1} in the free OH region. In agreement with experiment, both the T = 30 K CPMD and MD/CCSD(T) simulations and the harmonic frequency calculations on $H_5O_2^+$ give two transitions, split by about 100 cm^{-1}, due to the asymmetric and symmetric stretch modes of the water molecules. These results indicate that the Ne atom does not significantly perturb the $H_5O_2^+$ ion core. On the other hand, the predissociation spectrum of $H_5O_2^+$ Ar differs significantly from that of $H_5O_2^+$ Ne in the free OH stretch region of the spectrum. This is a consequence of the "strong" binding of the Ar atom to one of the H atoms, leading to a sizable red shift of the associated stretch vibration. The influence of the Ar atom on the free OH (OD) spectra of $H_5O_2^+$ and its D-substituted isotopologues is well accounted for by harmonic

frequency calculations on the Ar tagged ions.[177] For this reason, in the ensuing discussion of the vibrational spectra of $H_5O_2^+$ and its D-substituted isotopologues, we focus on the more challenging lower frequency region.

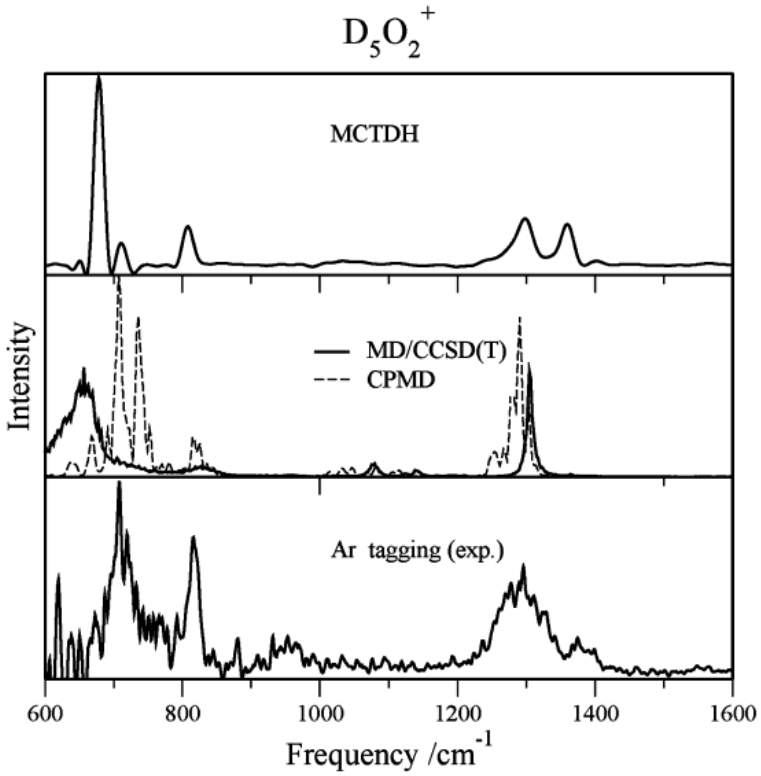

Figure 27. Computed IR spectra of $D_5O_2^+$ at the MD/CCSD(T) and CPMD levels of theory with corresponding MCTDH (0 K) spectra [203] and Ar predissociation spectra [201].

ii. Bending Region of the Spectra.

Figures 26-28 report the low-frequency spectra of $H_5O_2^+$, $D_5O_2^+$, $D_4HO_2^+$, and $DH_4O_2^+$ obtained from *T* = 30 K MD/CCSD(T) and CPMD simulations, 0 K MCTDH calculations,[180,181,203] and Ar- atom predissociation measurements. [201,202,177] Figure 29 shows calculated spectra for $DH_4O_2^+$. For $H_5O_2^+$, Figure 26 also includes the Ne atom predissociation spectrum. For $DH_4O_2^+$ and $D_4HO_2^+$, MD results are reported for both the "exterior" and "interior" isomers, while MCTDH results are available only for the interior isomers. For each isotopologue

the spectra obtained using the two MD approaches are in fairly good agreement, and for that reason, we focus on the results obtained using the MD/CCSD(T) approach.

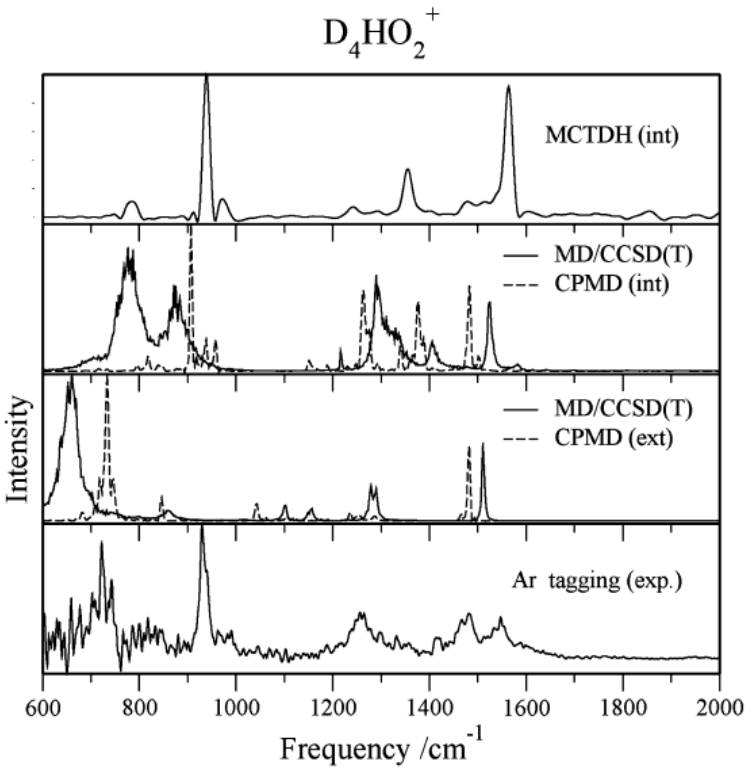

Figure 28. IR spectra of mixed H/D isotopologues $D_4HO_2^+$ calculated using the MD/CCSD(T) and CPMD methods with hydrogen in both interior and exterior positions. The corresponding MCTDH (0 K) spectra [203] are shown only for the interior isomer. The presented experimental spectra are for $D_4HO_2^+$ Ar.

The vibrational predissociation spectra of all isotopologues considered display more structure in the bending regions than would be expected on the basis of the harmonic frequency calculations. Specifically, the predissociation spectra of $H_5O_2^+$ Ne, $H_5O_2^+$ Ar, and $D_5O_2^+$ Ar each display two peaks in the bending regions, and that of $D_4HO_2^+$ Ar displays background structure throughout the 1170-1650 cm^{-1} range, with three peaks superimposed on the broad structure. As will be discussed below, we believe the additional bands in the spectra arise from Fermi

resonances and possibly also the presence of both interior and exterior isomers in the case of $DH_4O_2^+$ and $D_4HO_2^+$. Indeed, McCunn et al. presented evidence that both isomers contribute to their experimental Ar-tagged spectra. [201,202]

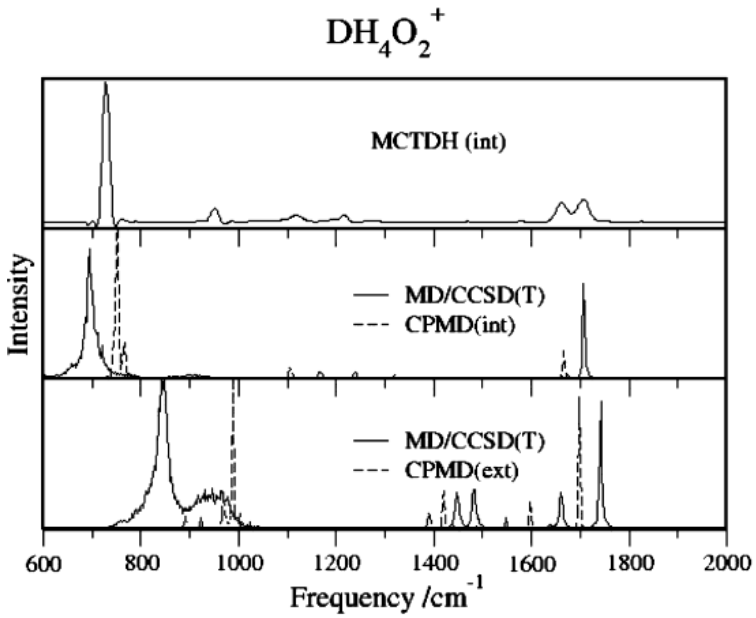

Figure 29. IR spectra of mixed H/D isotopologues $DH_4O_2^+$ calculated using the MD/CCSD(T) and CPMD methods with deuterium in both interior and exterior positions. MCTDH simulations (0 K)[203] are shown only for the interior isomer.

For $H_5O_2^+$ and $D_5O_2^+$ the experimental predissociation spectra display broad bands centered near 1760 and 1300 cm^{-1}, respectively, with weak shoulders about 100 cm-1 to the blue of the intense features. The MD/CCSD(T) simulations on $H_5O_2^+$ and $D_5O_2^+$ give strong transitions near 1780 and 1300 cm^{-1}, respectively, very close to the corresponding harmonic frequencies for the bending vibrations reported in Table 22. We conclude, therefore, as did Meyer and co-workers on the basis of analysis of the results of their MCTDH calculations, that the strong transitions near 1760 and 1300 cm^{-1} are due to the HOH and DOD bending vibrations, respectively. Interestingly, the weak satellite bands that show up in the measured spectra ~110

cm^{-1} to the blue of the bending transitions and which are absent in the MD spectra are recovered in the MCTDH calculations. This appears to be a shortcoming of the MD calculations. In the case of $H_5O_2^+$, Meyer and co-workers assigned the satellite band to a combination state dominated by one quantum in the shared proton stretch and two quanta in the water-water stretch. The peak to the blue of the bending transition of $D_5O_2^+$ was not assigned by Meyer and co-workers, although they did note that it does not correspond to a combination band involving shared proton stretch and water-water stretch.

The measured predissociation spectrum of $D_4HO_2^+$ displays moderately strong bands near 1260, 1480, and 1520 cm^{-1} and a weak feature near 1400 cm^{-1}. The MD/CCSD(T) simulations on the more stable $HD_4O_2^+$(int) isomer give six features in the bending region (strong features at 1300 and 1525 cm^{-1}, medium strength transitions at 1400 and 1330 cm^{-1}, and very weak transitions at 1230 and 1580 cm^{-1}). The 1230, 1300, 1525, and 1580 cm^{-1} features in the MD/CCSD(T) spectra fall close to the harmonic frequencies for the bend and shared proton perpendicular vibrations. On this basis, we conclude that the 1230 and 1300 cm^{-1} transitions from the MD/CCSD(T) simulations are due to the DOD bending vibrations and that the two higher energy transitions are due to the perpendicular motion of the shared proton. The MCTDH calculations on $D_4HO_2^+$ (int) give two strong transitions near 1355 and 1560 cm^{-1}, with the former being due to a bending mode and the latter to a combination band involving one quantum of the shared proton stretch and one quantum of the water-water stretch. The MCTDH calculations also give several weak unassigned features in the 1200-1550 cm^{-1} range.

The calculated spectra for $DH_4O_2^+$ in Figure 29 show significant differences for the interior and exterior isomers. The MD/CCSD(T) and CPMD simulations of the higher energy $DH_4O_2^+$ (int) isomer give a single strong transition near 1710 cm^{-1}, close to the 1740 cm^{-1} HOH

bending frequency found in the harmonic calculations. The MCTDH calculations on $DH_4O_2^+$ (int) predict a doublet of roughly equal intensity peaks near 1660 and 1720 cm^{-1}. The 1660 cm^{-1} feature in the MCTDH spectrum is associated with the water bend, and the 1720 cm^{-1} feature with a combination band involving one quantum of the shared D^+ stretch plus two quanta of the water-water stretch. This doublet is not captured by the classical simulations. The MD/CCSD(T) and CPMD calculations for the lower energy $DH_4O_2^+$ (ext) isomer display intense features near 1700 cm^{-1}, with a number of satellite features between 1400 and 1650 cm^{-1}; these are in rough accord with the harmonic frequencies of this isomer. (MCTDH calculations were not reported for this isomer.) If both isomers play a role in the Ar tagging experiment, as suggested by experimental results published in the OH/OD stretch regions of the spectrum,[202] then the present calculations suggest a rather complex spectrum in this region.

iii. O-H-O (O-D-O) Asymmetric Stretch Region of the Spectra.

We now turn our attention to the vibrational spectra in the shared proton stretch region. As noted in the Introduction, the experimental predissociation spectrum of $H_5O_2^+$ Ne (Figure 26) displays a doublet (peaks at 928 and 1047 cm^{-1}) in the shared proton stretch region. In going from $H_5O_2^+$ Ne to $H_5O_2^+$ Ar each member of the doublet in the former is "split" into a pair of doublets. Since none of the calculations (discussed below) on the bare ion show this pair of doublets, we conclude that they are induced by the Ar atom, rather than being intrinsic to $H_5O_2^+$. The Ar atom interacts much more strongly with the $H_5O_2^+$ ion than does the Ne atom (as is apparent from the spectra in the free OH stretch region), and since the inert gas atom preferentially binds to one of the dangling H atoms, this results in a greater degree of symmetry breaking in the Ar case.[177] Thus, we speculate that the extra structure in the shared proton

asymmetric stretch region of the spectrum of $H_5O_2^+$ Ar is a consequence of the mixing with what would otherwise be dark overtone states involving the water-water stretch and water wag.

Both the MD/CCSD(T) and MCTDH calculations on $H_5O_2^+$ give two strong features in the region of the shared proton stretch, with energies of 850 and 980 cm^{-1} and 910 and 1025 cm^{-1}, respectively, in good agreement with the experimental results for $H_5O_2^+$ Ne. As noted above, the underestimation of the energies of the features from the MD simulations could be the result of an incomplete recovery of the anharmonicity of the potential energy surface. The 850 cm^{-1} band found in the MD/CCSD(T) simulations falls very close to the harmonic frequency for the shared proton stretch, which suggests that the lower energy component of the MD doublet is likely to be dominated by shared proton stretch motion. Indeed, this is confirmed by the driven MD simulations of Kaledin et al.[179] On the other hand, the lower energy component of the doublet in the MCTDH calculations derives primarily from a combination state involving one quantum of the water-water stretch and two quanta of the water wag, while the higher energy member of the doublet is dominated by the shared proton stretch. For such strongly perturbed states, these differences between the assignments based on classical and quantum calculations are not surprising.

Consider next the spectra of $D_5O_2^+$ shown in Figure 27. The vibrational predissociation spectrum of $D_5O_2^+$ Ar displays intense features near 705 and 810 cm^{-1}, which are about 250 cm^{-1} to the red of the corresponding doublet in the predissociation spectrum of $H_5O_2^+$ Ne. The doublet structure in the region of the shared proton stretch is recovered by the MD/CCSD(T) and MCTDH calculations, with bands near 650 and 830 cm^{-1} in the former and near 680 and 805 cm^{-1} in the latter. The 650 cm^{-1} band in the MD/CCSDT(T) spectrum is close to the harmonic frequency (Table 22). In the MCTDH calculations, the lower energy band has as its dominant

component the shared proton stretch and the higher energy band is primarily due to the combination state, comprised of one quantum of the water-water stretch and two quanta of the wag. Both sets of calculations predict the lower energy band to be much more intense than the higher energy band, whereas the difference in intensity is only about 1.5:1 in the experimental spectrum. This difference in the relative intensities in the calculated and measured spectra of the higher energy peak in the measured spectrum is likely due to the presence of the Ar atom in the experimentally probed ions.

In the case of $D_4HO_2^+$ Ar, the experimental spectrum, shown in Figure 28, displays in the shared proton stretch region two strong bands of nearly equal intensity at 720 and 930 cm^{-1} as well as a weak feature near 800 cm^{-1}. On the basis of simple considerations, the 720 cm^{-1} band might be expected to be due to the exterior (H in the exterior) and the 930 cm^{-1} band to the interior (H on the interior) isomer. For $D_4HO_2^+$ (int) the MD/CCSD(T) calculations give a doublet at 775 and 885 cm^{-1}, slightly to the red of the doublet calculated for $H_5O_2^+$, and in good accord with experiment. The MCTDH calculations on $D_4HO_2^+$ (int) give a strong peak at 930 cm-1 in excellent agreement with experiment, but the feature near 775 cm^{-1} does not correspond as well with the experimental feature at 720 cm^{-1}. Analysis of the MCTDH wave functions shows that the intense peak has as its major component the shared proton stretch, and that the weak 775 cm^{-1} feature is due to a combination band involving one quantum of the water-water stretch and two quanta of the wag. The MD/CCSD(T) simulations on the exterior isomer give a single intense line at 660 cm^{-1}, close to that calculated for $D_5O_2^+$. This intense feature is not seen in the calculated spectra of $D_4HO_2^+$ (int); however, it may correspond to the spectral congestion seen in the region between 600 and 700 cm^{-1}. Comparison of the calculated and experimental

spectra is clearly complicated by the possible presence of both isomers and perturbation of the associated spectra by the Ar atom, as noted by McCunn et al. [201,202]

Finally, we consider the calculated spectra of $DH_4O_2^+$, shown in Figure 29. The spectrum of $DH_4O_2^+$(int) for both the MD/CCSD(T) and MCTDH calculations gives a single intense transition near 700 cm^{-1}, at essentially the same location as for the shared proton stretch in the harmonic calculations. The MD/CCSD(T) spectrum for the lower energy $DH_4O_2^+$(ext) shows a doublet feature that is blue-shifted relative to the intense peak for $DH_4O_2^+$ (int). This feature is not found in the CPMD spectrum, and thus, it will be interesting for future experiments and perhaps new MCTDH calculations for $DH_4O_2^+$ (ext) to explore this region of the spectrum.

IV. Conclusions

The present investigation shows that classical MD simulations at a temperature of 30 K qualitatively reproduce many of the key features in the experimental vibrational predissociation spectra of $H_5O_2^+$ and its D-substituted isotopologues. Most strikingly, the MD simulations give Fermi resonance doublets in the region of the shared proton stretch of $H_5O_2^+$, $D_5O_2^+$, $D_4HO_2^+$, and $DH_4O_2^+$. In the latter two cases, the more stable isomer, i.e., the one with H^+ "in the middle", appears to dominate the experimental spectrum; it is clear from both experiment and the present calculations that the less stable isomer is present in the experimental spectra. Without a quantitative measure of the relative contributions of the two isomers, it is difficult to make a quantitative comparison between the experimental and calculated spectra. A further complication in comparing the calculated and measured spectra of $H_5O_2^+$ and its isotopologues is that the calculations have been performed for the bare ions, and the experimental spectra have been obtained by predissociation of attached inert gas atoms. Only for $H_5O_2^+$ are experimental results

available for a Ne atom tag. For the other isotopologues the vibrational predissociation spectra have been measured with the more strongly perturbing Ar atom tag.

Overall the spectra obtained form the CPMD simulations using the BLYP density functional method are similar to those obtained from the MD simulations using the CCSD(T) potential energy surface, which is encouraging as AIMD simulations using DFT functionals are applicable to much larger clusters. Comparison of the spectra from the MD simulations to those from the MCTDH calculations does show several significant differences, particularly with regard to the relative intensities of some of the bands. These differences appear to be due primarily to the low-temperature MD simulations underestimating diagonal anharmonicities which are especially important for the shared proton stretch and wag vibrations of $H_5O_2^+$ and its isotopologues.

APPENDIX C

VIBRATIONALLY INDUCED INTERCONVERSION OF H-BONDED $NO_2^- \cdot H_2O$ ISOMERS WITHIN $NO_2^- \cdot H_2O \cdot AR_M$ CLUSTERS

Results have been published in: *J. Phys. Chem. A* **2009,** 113, 975–981.

I have carried out the theoretical calculations.

Vibrationally Induced Interconversion of H-Bonded $NO_2^- \cdot H_2O$ Isomers within $NO_2^- \cdot H_2O \cdot Ar_m$ Clusters Using IR-IR Pump-Probe through the OH and NO Stretching Vibrations

Rachael A. Relph, Ben M. Elliott, Gary H. Weddle, and Mark A. Johnson*

Sterling Chemistry Laboratory, Yale University, P.O. Box 208107, New Haven, Connecticut 06520

Jing Ding and Kenneth D. Jordan*

Department of Chemistry, University of Pittsburgh, Pittsburgh, Pennsylvania 15260

We introduce a method based on sequential application of vibrational predissociation spectroscopy to explore the high-amplitude rearrangements available in a small H-bonded complex that is vibrationally excited within a larger Ar cluster. The weakly bound Ar atoms play

the role of a solvent in mediating the energy content of the embedded system, ultimately quenching it into local minima through evaporation. We demonstrate the approach on the NO_2^- H_2O binary hydrate, which is known to occur in two nearly isoenergetic isomeric forms. The scheme involves three stages of mass separation to select a particular NO_2^- H_2O Ar_m parent ion cluster prior to vibrational excitation and then isolate the NO_2^- H_2O Ar fragment ions for interrogation using resonant vibrational predissociation with a second infrared laser. The initial vibrational excitation selectively energizes one of the isomers through one of its characteristic resonances while the predissociation spectrum of the NO_2^- H_2O Ar fragment encodes the distribution of isomers present after Ar evaporation. Isomerization from the front- to backside form is found to occur upon excitation of the NO stretch near 1200 cm^{-1}; although the reverse reaction is not observed upon excitation of the NO stretch, it is observed upon excitation of the higher-energy OH stretching fundamental near 3000 cm^{-1}. We discuss these observations in the context of the calculated isomerization energetics, which focus on the minimum energy structures for the isomers as well as the transition states for their interconversion.

I. Introduction

Vibrational predissociation spectroscopy of mass-selected ion clusters is emerging as the method of choice for the structural characterization of ion-solvent complexes, where weakly bound messenger species such as Ar atoms are used to record absorption in an action mode via mass loss.[204] This has been particularly useful in elucidating the structures of the hydration shells around simple ions, with the halide ions representing a classic case in which all six of the fundamentals associated with X^- H_2O have been observed experimentally.[205,206,207,208,209,210] In many cases, however, the strength and directionality of the H-bond leads to many isomeric

structures in the ionic hydrates, $A^{-/+}(H_2O)_n$.[211,212,213,214] This circumstance has presented a complication in spectroscopic studies attempting to characterize minimum energy structures because one is routinely faced with sorting out extra bands that arise from anharmonic effects (Fermi resonances, combination bands, etc.) of a particular isomer from the heterogeneous contributions of distinct species. To address this complexity, we have recently developed a general method for obtaining isomer-specific spectra within the context of a mass-selective, predissociation-based variant of two-dimensional IR spectroscopy.[215] With the vibrational signatures of the various isomers in hand, we are now in an excellent position to exploit this knowledge to explore significant features on the extended potential energy landscape, such as barriers to isomer interconversion. In this context, the occurrence of the isomers becomes an advantage because they provide benchmarks that reveal the range of the excursions available from various starting points on the surface. We report here an extension of our IR-IR hole burning method12[215] to monitor vibrationally induced isomerization within a size-selected Ar cluster. In essence, the attached Ar atoms play the role of solvent in that they mediate the energy content of a tightly bound core ion complex through intra- and intermolecular vibrational relaxation IVR and ultimately quench the clusters into local minima by evaporative cooling. This scheme can be viewed as an Ar-cluster variation on the collisionally mediated photoisomerization method developed for neutral complexes by Zwier and co-workers[216] over the past several years. The significant differences in its application to ionic clusters are that in the clusters, quenching occurs by Ar evaporation rather than through bimolecular collisions, and predissociation is used instead of resonant multiple photon ionization to carry out the spectroscopic characterization of the isomers present after excitation. We demonstrate the

method on the NO_2^-·H_2O binary cluster, which occurs in two low energy isomeric forms that were spectroscopically characterized in our earlier report.[215]

The strategy of our approach is illustrated schematically in Figure 30, which depicts the situation at play in NO_2^-·H_2O. The two isomers have the calculated structures (B3LYP [217,218, 219] [220]/aug-cc-pVDZ [221,222]) indicated at the bottom of the figure. Isomer A is the "backside" form in which the water molecule docks primarily to one oxygen atom on NO_2^- in a single ionic H-bonding arrangement such that the "free" H atom is oriented toward the N atom. Isomer B is the so-called "frontside" form, in which the water molecule attaches each of its hydrogen atoms to the oxygen atoms on the NO_2^- ion in a double H-bonded configuration. In this photoisomerization scheme, a particular isomer is selectively excited through one of its characteristic vibrational transitions within a mass-selected NO_2^-·H_2O·Ar_m cluster. This energized cluster then undergoes IVR, ultimately leading to photoevaporation of one or more weakly bound Ar atoms ($n_{evap} \approx h\nu/\Delta H_{evap}$ (Ar)), which is the essential feature of the popular "tagging" approach for obtaining mass-selective vibrational spectra of ions.[204, 223] Here we are interested in the case in which the vibrationally excited core ion can undergo isomerization before the energy is lost to evaporation, a process described by the following kinetic scheme:

$$^{I,II}[NO_2^-\bullet H_2O]\bullet Ar_m + h\nu^{I}_{pump} \rightarrow {}^{I}[NO_2^-\bullet H_2O]^{\dagger}\bullet Ar_m \xrightarrow{k_{evap}} {}^{I}[NO_2^-\bullet H_2O]\bullet Ar_{m(I)} + (m-n(I))Ar \quad (1a)$$

$$\xrightarrow{k_{isom}} {}^{II}[NO_2^-\bullet H_2O]^{\dagger}\bullet Ar_m \xrightarrow{k_{evap}} {}^{II}[NO_2^-\bullet H_2O]\bullet Ar_{n(II)} + (m-n(II))Ar \quad (1b)$$

where the superscripts I and II denote the two NO_2^-·H_2O isomeric cores, $h\nu^{I}_{pump}$ indicates that the pump laser is tuned to a resonance associated exclusively with isomer I, and (m - n(I)), (m - n(II)) denote the number of Ar atoms lost upon formation of the quenched isomers I and II, respectively. The initial NO_2^-·H_2O·Ar_m cluster is chosen to contain a sufficiently large number (m)

of attached Ar atoms such that at least one Ar atom remains attached after the photofragmentation induced by the pump laser. This is important because one can then monitor the predissociation spectra of the primary photofragments,

$$^{I,II}[NO_2^- \cdot H_2O] \cdot Ar_{n(I,\,II)} + h\nu_{probe} \rightarrow {}^{I,II}[NO_2^- \cdot H_2O] + n(I,\,II)Ar \qquad (2)$$

as a means of establishing the isomer distribution present in the fragment ion ensemble. Although not illustrated above, it is clearly also possible that isomerization can occur during the course of Ar evaporation.

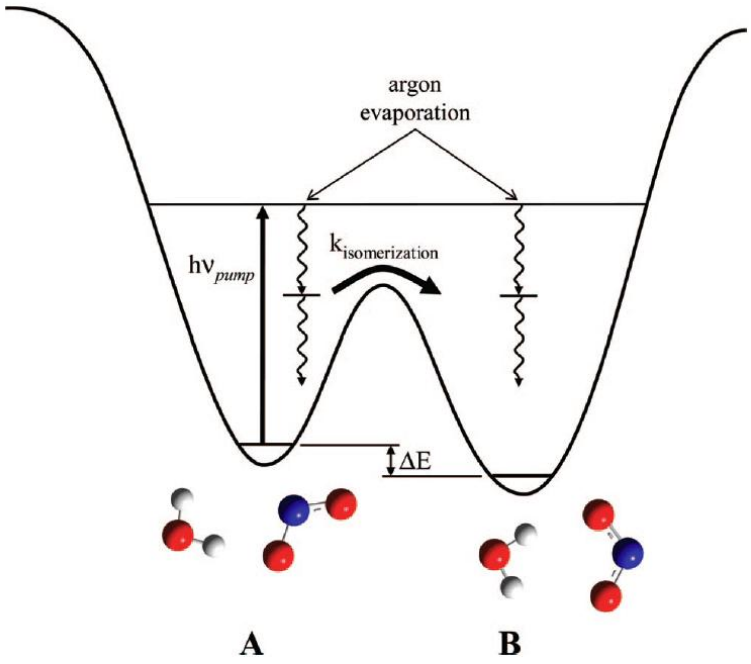

Figure 30. Schematic illustration of the Ar cluster-mediated approach to vibrationally induced intracluster photoisomerization. Isomer-selective vibrational excitation is carried out by a fixed frequency pump laser ($h\nu_{pump}$), which is sufficiently energetic to photoeject several Ar atoms. When the parent cluster is chosen such that at least one Ar atom remains on the daughter ions, the isomeric composition of these fragments can be established by obtaining their vibrational predissociation spectra (after mass selection) with a second infrared laser.

Photoisomerization in this regime thus requires that the isomerization rate (k_{isom}) is sufficiently fast to compete with the evaporation rate of the weakly bound Ar atoms.

A key requirement of this approach is that k_{isom} is sufficiently fast to compete with evaporative energy loss, k_{evap}. Although one anticipates that IVR within a strongly H-bonded complex will be fast compared to the rate of Ar evaporation, these rates are not generally known in ion clusters.[224,225] As such, one of our primary goals in this study is to clarify whether isomerization can be observed in this intracluster regime. We will demonstrate that efficient interconversion does, indeed, occur between the NO_2^--H_2O isomers; moreover, this transformation occurs in a fashion that depends strongly on the vibrational mode excited and, thus, the energy delivered to the cluster. This dependence is considered in the context of the calculated transition states for migration of the water molecule around the NO_2^- anion.

II. Experimental Details

Figure 31 outlines the protocol of the pump-probe approach. Two tunable infrared lasers intersect a pulsed ion beam at two of the three mass-selective, transient foci of the mass spectrometer, which are created using two pulsed fields and a reflectron. To implement this capability, the Yale double-focusing, tandem TOF photofragmentation spectrometer [226] was lengthened by about 1.5 m to accommodate a coaxial, pulsed acceleration region (located about 50 cm beyond the pump laser intersection at the first transient focus (F1)), followed by a second reflectron, R2. These features enable mass separation of the species created by the first laser at a second transient focus (F2), where a second tunable IR laser interrogates photofragments created by the pump laser. Fragments produced by the probe laser are then isolated using reflectron R2, which has an MCP ion detector (D2) located at the resulting third focal point. The overall

assembly is equivalent to an MS3 fragmentation experiment in the parlance of analytical mass spectrometry.

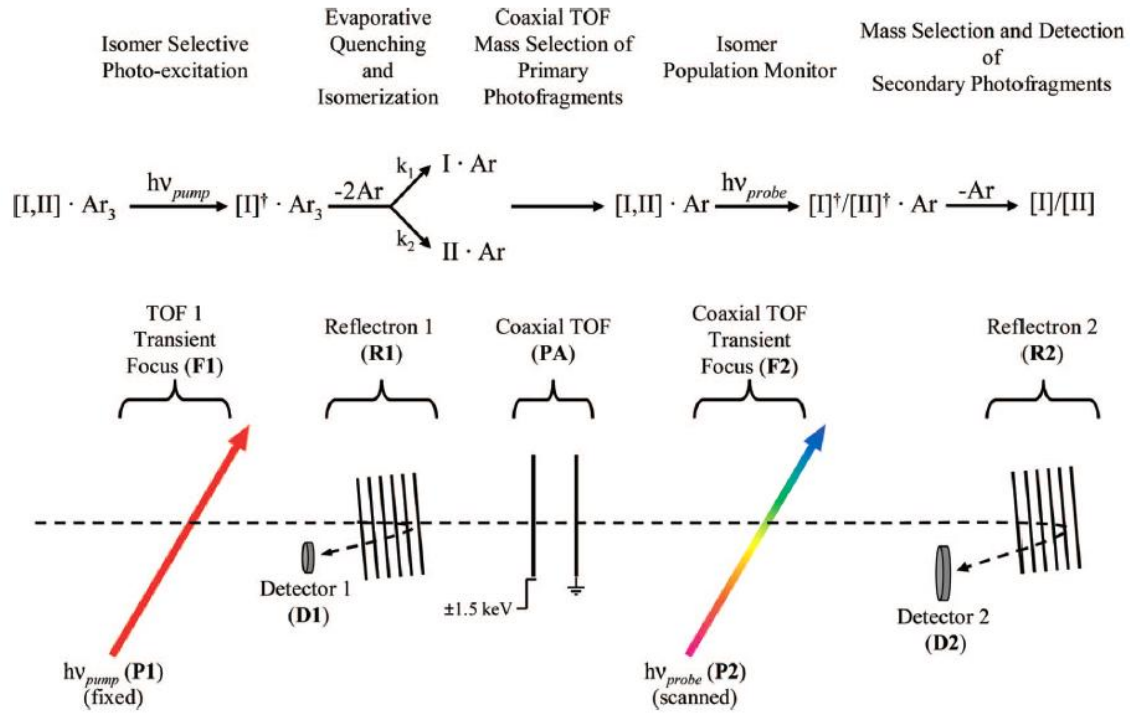

Figure 31. Outline of the experimental sequence of events used to carry out Ar-mediated, intracluster photoisomerization. An ion packet containing a mixed ensemble of isomers is mass-selected in the first stage of a time-of-flight (TOF) mass spectrometer, where a fixed frequency pump laser (P1) is tuned to a transition of one of the isomers and injects this species with vibrational energy, $h\nu_{pump}$. This interaction is optimized by monitoring the fragments on reflectron R1 with detector D1. After optimization, R1 is turned off, allowing the parent and daughter ion packets to pass without discrimination. If isomerization occurs, argon evaporation quenches the excited cluster into minima corresponding to the different isomeric forms. To characterize the isomer composition in the fragment ions, they are isolated from the parents remaining after pump excitation in a second (coaxial) TOF stage of mass selection using a pulsed acceleration (PA) region. A second tunable IR laser (the probe laser, P2) intersects the fragment ion packet at the transient focus of the second TOF stage. The predissociation spectrum arising from the scanned probe laser is recovered by detecting the resulting Ar loss detector D2 after a third stage of TOF mass selection using reflectron R2.

When carrying out the measurement, the pump laser is tuned to an isolated band assigned to one of the $NO_2^- \cdot H_2O$ isomers, and the efficiency of the excitation is maximized by monitoring the resulting photofragments on detector D1 with reflectron R1. R1 is then switched off, sending the remaining parent and photofragment ions together down the drift tube. This mixed mass ion packet is then separated by a pulsed, coaxial field, labeled PA in Figure 31, which is switched on just after the ion packet enters the region between the grids (7 cm separation). The grid closest to the ion source is typically pulsed from ground to -1.5 kV, with the remaining electrode held at ground. As such, the kinetic energies of all ions in the packet are increased by ~1.5 keV. Parent and daughter ions from the pump laser are thus separated in this second TOF step, and the probe laser is timed to selectively intercept the daughter fragment created in the first predissociation event that retains one Ar atom (eq2). Scanning the probe laser recovers the predissociation spectrum of these fragments, and the resulting bands reveal its isomeric composition.

The $NO_2^- \cdot H_2O \cdot Ar_m$ clusters were generated by entraining [227] NO_2 and H_2O on the low-pressure side of a pulsed supersonic expansion of Ar that was ionized with a 1 keV counterpropagating electron beam. The laser pulse energies used in this work were ~10 mJ in the 2800-3800 cm^{-1} range, and 0.3-0.6 mJ in the 1000-2000 cm^{-1} range, where the latter region was obtained by secondary conversion in $AgGaSe_2$. [228, 229] The reported spectra result from the accumulation of 10-30 scans.

III. Results and Discussion

We illustrate the method through its application to the $NO_2^- \cdot H_2O$ cluster ion, which is fortuitously prepared with comparable yields of the back- and frontside isomers (A and B in Figure 30, respectively) in the ionized free-jet cluster source.[215] The vibrational predissociation spectrum of the $NO_2^- \cdot H_2O \cdot Ar$ cluster, presented in Figure 32a, thus consists of two overlapping

patterns. In discussing the assignments of the various bands, we make use of the results of reference [215] where ion-dip spectroscopy was used to separate the contributions of the two isomers. The contributions from each isomer are indicated in color, with blue representing the backside isomer and red indicating bands from the frontside isomer. The bands above 2500 cm^{-1} are derived from the OH stretching vibrations. The backside species contributes the strong ionic hydrogen-bonded (IHB) OH stretch ($\nu_{OH}^{IHB}(back)$) at 2975 cm^{-1} along with a weaker nonbonded OH stretch ($\nu_{OH}^{free}(back)$) near 3700 cm^{-1}. The backside isomer also contributes a broad feature near 3200 cm^{-1}, which may be a combination band involving the 2975 cm^{-1} fundamental and an ion-water molecule stretching vibration (calculated at the B3LYP/aug-cc-pVDZ level to occur at 242 cm^{-1}). The OH stretching pattern of the frontside species consists of a long progression of peaks evolving to higher energy relative to a band origin at 3250 cm^{-1}, with a characteristic spacing of about 90 cm^{-1}. We have previously discussed [211,230] the origin of this pattern in the context of combination band structure involving the OH stretching fundamentals with the rocking motion of the water molecule between the two oxygen atoms of NO_2^-. Qualitatively, the progression can be viewed in a Franck-Condon picture, where the shapes of the vibrationally adiabatic potentials for the rocking motion are strongly dependent on the number of quanta in the OH stretching vibration. This leads to displaced potentials for the rocking mode levels in going from $v_{OH} = 0$ to $v_{OH} = 1$ (in a local mode description), which in turn gives rise to overlap of the ground vibrational state with many v_{rock} levels upon excitation of the OH stretching fundamental.

The lower energy region of the predissociation spectrum is dominated by sharp bands arising from the NO stretches, where each isomer contributes two such bands. Most convenient for this study are the two very close bands near 1200 cm^{-1}, where the lower-energy 1203 cm^{-1}

band is due to the backside isomer and the higher energy 1230 cm^{-1} band arises from the frontside isomer. This leads to a favorable situation in which one can manipulate the isomer populations by tuning the pump laser between these two closely spaced transitions.

IIIA. Theoretical Details and Expectations.

To aid in the assignment of the spectra and in interpreting the isomerization dynamics, we have carried out an exhaustive search for stationary points on the NO_2^- -H_2O potential energy surface at the MP2 [231]/aug-cc-pVDZ level of theory. The QST3 procedure [232] was employed to locate the transition state structures. For each stationary point identified, the vibrational frequencies were calculated in the harmonic approximation, again using the MP2/ aug-cc-pVDZ method, to confirm the nature of the stationary points. The geometries of the minima were also optimized, and the harmonic vibrational frequencies were calculated at the B3LYP/aug-cc-pVDZ level of theory. Although the frequencies from the two sets of calculations are quite similar, the two theoretical methods give very different IR intensities, particularly for the NO stretch bands, with the results from the B3LYP calculations being in closer agreement with experiment. B3LYP calculations on the isolated NO_2^- ion reveal that the symmetric NO stretch lies higher in frequency than the asymmetric NO stretch, in agreement with experiment.[233] The opposite ordering of these two vibrations is found with the MP2 method, presumably due to the inadequacy of the Hartree-Fock reference configuration for describing the diradical character of NO_2^-. For this reason, the B3LYP results have been used in analyzing the spectra. Figures 32b and c report the calculated (B3LYP/aug-cc-pVDZ, scaled, harmonic) vibrational spectra for the frontside and backside isomers, respectively. Overall, the measured fundamentals are recovered quite well at the harmonic level for this method, with the most significant difference being the greater number of lines in the experimental spectra resulting from anharmonic couplings.

Both the B3LYP/aug-cc-pVDZ and MP2/aug-cc-pVDZ calculations predict the frontside isomer to be about 240 cm^{-1} more stable than the backside isomer after correction for vibrational zero-point energies. We also carried out single-point MP2/aug-cc-pVTZ, CCSD(T)[234,235,236,237,238]/aug-cc-pVDZ, and multireference MP2 (MRMP2) [239]/aug-cc-pVDZ calculations on the two low-energy minima, employing the MP2/aug-cc-pVDZ geometries. (The MRMP2 calculations employed the two references needed to account for the diradical nature of NO_2^-) The B3LYP and MP2 calculations were carried out with the Gaussian 03 program,[131] and the CCSD(T) and MRMP2 calculations were carried out using Molpro.[130] The adoption of the more flexible basis set proves to have a negligible effect on the relative energies of the front and backside isomers. On the other hand, the CCSD(T) and CASMP2 calculations favor the frontside isomer by 417 cm^{-1}, as compared to by 240 cm^{-1} in the MP2 or B3LYP calculations. It is clear from these results that the frontside and backside isomers of $NO_2^- \cdot H_2O$ are close in energy.

If the energy ordering of the two isomers from the calculations described above is indeed correct, then the energy threshold for backside-to-frontside isomerization would be lower than that for the reverse reaction. It is therefore of interest that the experimental results presented below are consistent with a lower threshold for the frontside-to-backside process, raising the possibility that the observed rates reflect the detailed dynamics underlying the relative k_{isom} and k_{evap} rates.

The potential energy surface describing even a simple situation, such as the $NO_2^- \cdot H_2O$ interaction, is surprisingly complex, but the calculations suggest that the key reaction pathway is that shown in Figure 33. This path is essentially passage of the water molecule around one of the oxygen atoms in NO_2^- with concomitant rotation of one of the hydrogen atoms. The transition

state structure is calculated to lie 1163 and 919 cm^{-1} above the frontside and backside isomers, respectively. (These numbers are based on MP2 calculations.)

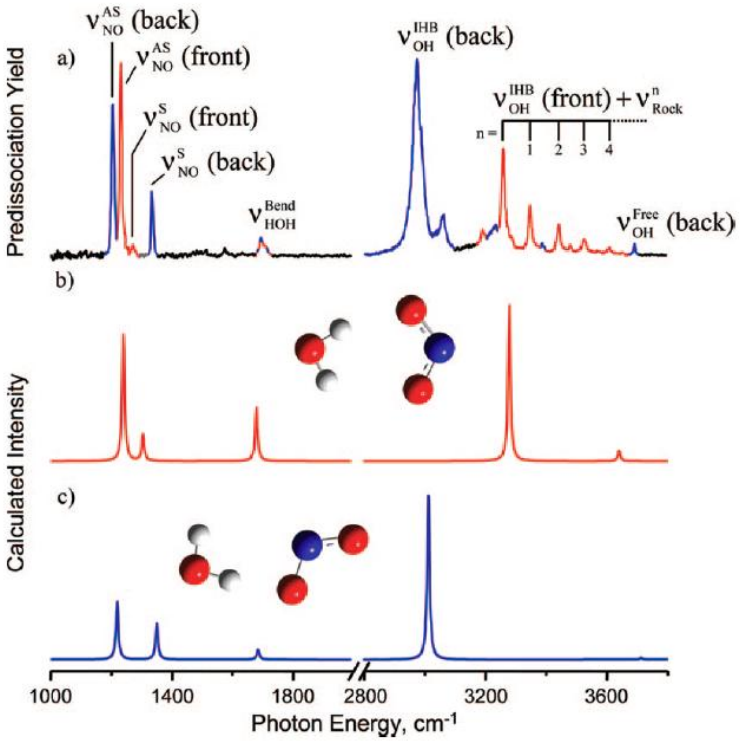

Figure 32. Vibrational predissociation and calculated (harmonic, B3LYP/aug-cc-pVDZ) spectra of $NO_2^- \cdot H_2O \cdot Ar$ in the NO stretching and OH stretching regions [215]: (a) nonisomer selective predissociation spectrum with those peaks belonging to the frontside isomer in red and those for the backside isomer in blue, (b) calculated spectrum of the frontside isomer, and (c) calculated spectrum of the backside isomer. Structures indicate the calculated minimum energy geometries.

IIIB. Isomer Conversion through the NO Stretching Modes.

We begin by investigating whether the isomers can undergo interconversion upon excitation of the ~1200 cm^{-1} NO stretching vibrations, which should provide internal energy just above the calculated barrier for the path in Figure 33. Previous studies have established that photofragmentation of Ar-tagged clusters at this energy is dominated by the loss of two Ar

atoms.[227,240,241] We therefore focus on the $NO_2^- \cdot H_2O \cdot Ar_3$ parent ion, which should preferentially yield the $NO_2^- \cdot H_2O \cdot Ar$ fragment ion upon excitation of the NO stretching vibrations of either isomer in the absence of isomerization. Experimentally, we observe $NO_2^- \cdot H_2O \cdot Ar$ to be the dominant fragment upon excitation of either isomer. The presence of the Ar tag allows us to determine the isomeric composition of this photofragment by predissociation spectroscopy. To maximize the signal in the isomer analysis step, we probed the fragment ions in the OH stretching region where high laser power is available in the 3000-4000 cm^{-1} range.

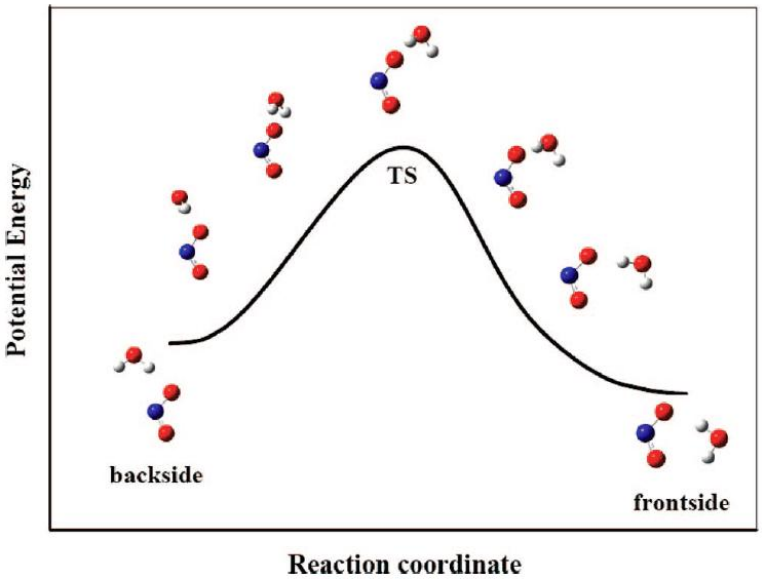

Figure 33. Reaction path for isomerization of $NO_2^- \cdot H_2O$. The TS was located using the QST3 method, as described in the text, and the reaction paths from the transition state to the two minima were established using the reaction path following method. The calculations are at the MP2/aug-cc-pVDZ level of theory.

Figure 34 presents the predissociation spectra of the $NO_2^- \cdot H_2O \cdot Ar$ fragment ions, where the top trace corresponds to excitation of the frontside isomer at 1230 cm^{-1} (indicated by the arrow in the Figure 34a inset), and the bottom trace results from excitation of the backside

isomer through its 1203 cm^{-1} band (arrow in Figure 34b inset). The main qualitative message from this experiment is that the isomeric parentage is largely maintained upon excitation in this energy range. In fact, the lower trace, corresponding to selective excitation of the backside isomer, contains no bands attributable to contamination from the frontside isomer. The scan in Figure 34b is thus the most definitive spectrum of this species yet recorded, with all features previously assigned to the backside isomer using double resonance being present. Although photoisomerization starting from the backside species is not observed through the NO stretches, this observation illustrates a powerful (if unanticipated) use for the double resonance method as a means with which to isolate the linear action spectrum of a particular isomer. That is, once the fragment ion is created in a pure isomeric form with an Ar tag, its spectrum can be obtained using predissociation in a low laser power regime, as opposed to the saturated conditions that are intrinsic to the hole-burning approach.

We next turn to the photoexcited frontside isomer through its NO stretching transition at 1230 cm^{-1} (arrow in Figure 34a inset). This is a more interesting result than that obtained for the backside isomer in that, although the characteristic progression is evident as expected for the frontside pattern, there are two additional peaks toward the low-energy side, labeled α and β in Figure 34b, that were very weak (α) or absent (β) in the $NO_2^- \cdot H_2O \cdot Ar$ spectrum (top trace in Figure 32) when this ion was extracted as a parent directly from the ion source. In addition, there is a small feature at 2975 cm^{-1}, the location of the strong band associated with the backside isomer, suggesting that isomer interconversion can be induced in this direction.

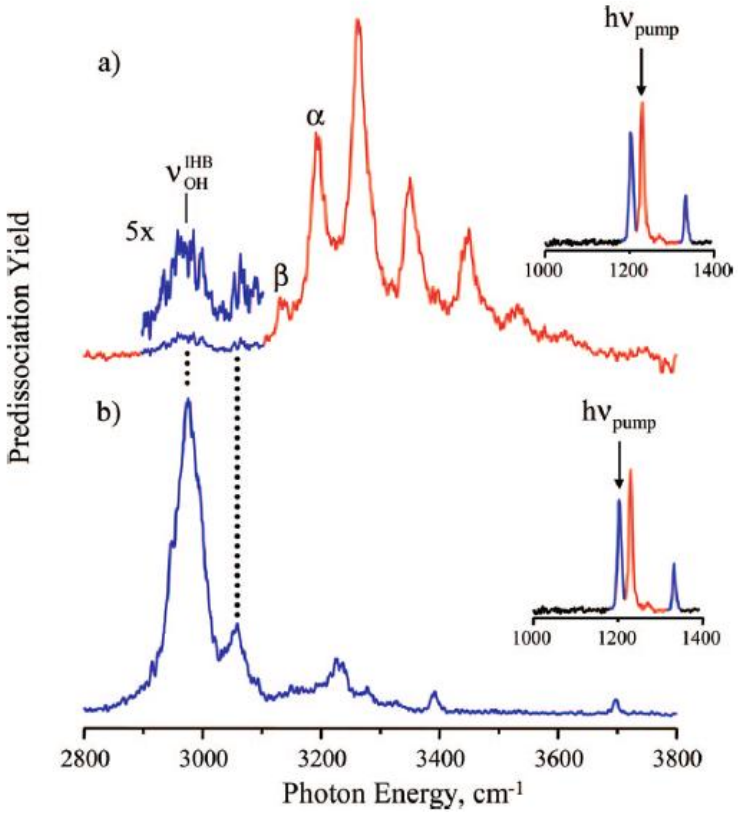

Figure 34. Argon predissociation spectra of the primary photofragment, $NO_2^- \cdot H_2O \cdot Ar$, produced from photoexcitation of $NO_2^- \cdot H_2O \cdot Ar_3$ with $h\nu_{pump}$ at (a) 1230 cm^{-1}, a frontside isomer transition, and (b) 1203cm^{-1}, a backside isomer transition, as indicated in the insets. For the frontside isomer in part a, features assigned to hot bands are labeled α and β and represent transitions to $\nu'_{rock} = 0$ from excited ν_{rock} levels in the OH ($\nu = 0$) level. See the vibrationally adiabatic potential discussion in the text. The presence of the backside ν_{OH}^{IHB} transition at 2975 cm^{-1} in part a indicates a small amount of conversion from frontside to backside, whereas the lack of any frontside features in part b indicates that excitation of the NO stretch does not induce conversion from the backside form to the frontside.

Interestingly, the spacing between the enhanced peaks (α and β) as well as between α and OH stretching fundamental at 3250 cm^{-1} is about 65 cm^{-1}, which is even lower in energy than that (~90 cm^{-1}) displayed by the main progression associated with the rocking mode of the water molecule. Recall that the Franck-Condon mechanism for the ($0 \rightarrow \nu'_{rock}$) progression involves

large displacements of the vibrationally adiabatic potentials describing the water-rocking motion upon OH stretching excitation.[230] In this context, a natural explanation for the new bands is that they are due to ($\nu''_{rock} \rightarrow 0$) hot bands in this mode, which gain oscillator strength through the same Franck-Condon mechanism.[230] Activity in the ≈65 cm^{-1} quantum is plausible, because photoexcitation of $NO_2^- \cdot H_2O \cdot Ar3$ at 1200 cm_{-1} does induce a small branching into the three Ar atom loss channel, and thus, the $NO_2^- \cdot H_2O \cdot Ar$ fragment likely retains internal excitation on the order of the Ar binding energy, which is roughly 400 cm^{-1}. It is worth noting that such a convenient internal energy monitor is rare in cluster work.[242,243] Of course, we expect the internal energies of both isomers created as photofragments to be similar, since they are both governed by the evaporative ensemble ansatz.[244] The spectrum of the backside isomer (Figure 34b), on the other hand, is similar to that displayed by the backside $NO_2^- \cdot H_2O \cdot Ar$ isomer extracted from the source (Figure 32a, bands presented in blue). These seemingly disparate observations are seen to be internally consistent, however, when one considers the fact that the backside isomer does not exhibit the strong anharmonic coupling needed to yield significant oscillator strengths for the transitions with large changes in soft mode quanta, as is the case for the frontside complex.

Summarizing the results in the NO stretching region, we find the backside isomer to survive photoexcitation and remain intact in the fragment ions, which yields a novel and useful method for obtaining isomer-selective spectra. The frontside isomer also largely survives excitation through the NO stretching transition but yields new bands in the photoproduct that likely arise from internal excitation in the $NO_2^- \cdot H_2O \cdot Ar$ fragments. There is, in addition, a small feature in the fragment spectrum that occurs in the band location expected for the backside structure, indicating that front-to-backside isomerization can be induced by excitation in the 1200 cm^{-1} range.

IIIC. Isomer Interconversion through the OH Stretching Modes.

The absence of interconversion from back- to frontside isomers upon NO stretch excitation would seem to imply that the barrier for this process is >1200 cm^{-1}. However, on the basis of the calculations, we believe it to be more likely that the rate of Ar evaporation is faster than that for isomerization in this direction, which presents an intrinsic limitation to this method. It is also the case that the evidence for conversion from the front- to backside isomer rests on a rather weak band near 3000 cm^{-1}, and it would be useful to identify a regime where the isomerization reaction is both efficient and unambiguously established through the spectroscopic diagnostics. Since the relative rates should depend on the internal energy content, we extended the study to explore excitation through the higher energy OH stretching modes. The nature of our approach dictates that we must also work with a larger number of attached Ar atoms in the $NO_2^- \cdot H_2O \cdot Ar_m$ parent ion, however, because we expect an average of five Ar atoms to be lost upon excitation of the cluster in the vicinity of the OH stretching transitions. We therefore focused this aspect of the study on the $NO_2^- \cdot H_2O \cdot Ar_6$ cluster because the dominant photo fragment ion should retain a single Ar atom, which is required for spectroscopic interrogation of the product. Interestingly, there is a noticeable change in the relative contributions of the isomers to the NO stretching bands with increasing Ar solvation. Specifically, the 1230 cm^{-1} frontside transition, which is slightly larger than the backside 1203 cm^{-1} line in the spectrum of the m = 1 parent, is reduced by about a factor of 2 in the m = 6 spectrum. We have often encountered situations in which the isomer distribution is strongly dependent on the extent of Ar salvation [212,214,245] and have even used this to our advantage in several systems as a means with which to obtain isomer-selective spectra. For the present application, however, the diminishing population of the frontside isomer in the larger cluster is a disadvantage, and the situation is further

complicated by significant broadening of its OH stretching pattern, which makes it difficult to exclusively excite this species. As a result, we were able to carry out an isomerization study only starting from the more abundant backside isomer.

In the case of OH stretching excitation, the higher power available for the pump laser led to a favorable situation in which we were able to interrogate its isomeric composition by probing the two nearby bands in the NO stretching region (i.e., the backside band at 1203 cm^{-1} and the frontside band at 1230 cm^{-1}). Figure 35 displays the low-energy spectrum of the $NO_2^- \cdot H_2O \cdot Ar$ fragment ion from the process,

$$NO_2^- \cdot H_2O \cdot Ar_6 + h\nu \rightarrow NO_2^- \cdot H_2O \cdot Ar + 5\ Ar \qquad (3)$$

with the pump laser tuned to excite the backside isomer at its strong 2975 cm^{-1} resonance corresponding to the fundamental of the ion-bound OH stretch [$\nu_{OH}^{IHB}(back)$ in Figure 32a]. The predissociation spectrum of the fragment ion does, indeed, display significant population in both isomers, with the higher energy band from the frontside isomer appearing with about one third of the intensity as the band due to the backside species. With this observation, we have thus succeeded in driving the isomerization reaction in both directions.

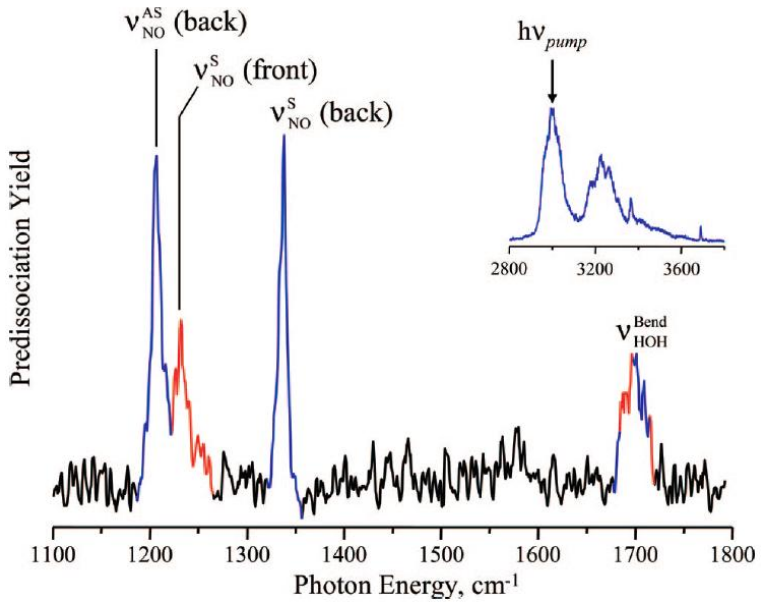

Figure 35. Argon predissociation spectrum of the NO_2^-·H_2O·Ar photofragment produced by photoexcitation of NO_2^-·H_2O·Ar_6 (OH stretch spectrum shown in inset) with $h\nu_{pump}$ at 3000 cm^{-1}, which is the ion-bound OH stretch of the backside isomer. Approximately 30% conversion to the frontside isomer is evidenced by the presence of the NO_2 asymmetric stretch at 1230 cm^{-1}, which is a characteristic feature of the frontside complex.

The ability to drive isomerization in both directions is key to extracting the relative stability of the isomers as well as the magnitude of the barrier separating them, as discussed at length by Zwier and co-workers.[246,247,248,249,250,251,252] The observation of isomerization at 1200 cm^{-1} is consistent with our calculated barrier of ~1076 cm^{-1} from the reaction path displayed in Figure 33. Unfortunately, the large energy gap between the NO and OH stretching quanta allows for only a crude bracketing of the energetics, and the likely suppression of isomerization by Ar evaporation further complicates quantitative determination of these quantities. There is, on the other hand, an alternative available in the Ar-mediated scheme that can be used to establish the relative energies of the isomers, even when the isomerization rate is suppressed in one direction, as appears to be the case here. Specifically, the relative energetics are encoded in the number of

Ar atoms evaporated when isomerization does or does not occur [(m - n(I)) and (m - n(II)) in eqs 1a and 1b, respectively], where the differences in Ar loss can be considered in the context of microcalorimetry.[253,254] Thus, the chemical energy from isomerization, ΔE (see Figure 30), should effectively add to the photon energy, $h\nu$, in determining the number of evaporation events, $n_{evap} \approx (\Delta E + h\nu)/\Delta H_{evap}$ (Ar). In the case of $NO_2^- \cdot H_2O \cdot Ar_6$, we note that, despite the observed ~30% conversion, the number of Ar atoms evaporated is as expected for the typical Ar binding energy of about 400 cm^{-1}. This observation indicates that the difference in energy between the two isomers is at most on the order of the argon binding energy and supports the interpretation that the failure to drive the back-to-frontside reaction at 1200 cm^{-1} excitation results from the kinetics rather than a large error in the calculated relative energies.

Our goal in the present study was to explore whether the relative rates of the intracluster processes described in eqs 1a and 1b allow an isomerization reaction to occur in a system that is unstable with respect to evaporation of a weakly bound solvent. The high efficiency of the isomerization reaction in the strongly bound $NO_2^- \cdot H_2O$ complex upon excitation at 3000 cm^{-1} establishes the viability of this approach. In fact, the detailed energetic of this system indicate that reaction can be observed even when the isomerization barrier is more than twice the Ar atom evaporation energy. This hierarchy of timescales is interesting because it enables a microscopic view of the exchange of energy between a reactive subsystem and surrounding solvent in a microcanonical regime. Moreover, this occurs in a sufficiently small system that the solvent bath states can be explicitly treated from a quantum perspective.

IV. Summary

We have introduced an Ar-cluster-mediated, pump-probe photoexcitation method involving three stages of mass selection to monitor isomerization reactions in size-selected

cluster ions. This capability is demonstrated by carrying out vibrationally induced isomerization of a water molecule between two binding sites on the NO_2^- anion upon photoexcitation of the $NO_2^- \cdot H_2O$ complex within the Ar clusters $NO_2^- \cdot H_2O \cdot Ar_3$ and $NO_2^- \cdot H_2O \cdot Ar_6$. This is significant because it establishes that embedded systems can cross reaction barriers that are larger than the Ar binding energy. Specifically, photoexcitation in the NO stretch region near 1200 cm^{-1} gives a small amount of frontside-to-backside isomerization but no backside to frontside isomerization. The front-to-backside reaction can be driven, however, upon excitation in the OH stretch region near 3000 cm^{-1}. These observations are consistent with our calculations of the isomerization path, which place the barrier around 1100 cm^{-1}.

APPENDIX D

ISOLATING THE SPECTRAL SIGNATURES OF INDIVIDUAL SITES IN WATER NETWORKS

Results have been published in: |*J. Phys. Chem. Lett.* **2010**, 1, 2396–2401.

I have carried out the theoretical calculations.

Isolating the Spectral Signatures of Individual Sites in Water Networks Using Vibrational Double-Resonance Spectroscopy of Cluster Isotopomers

Timothy L. Guasco, Ben M. Elliott, and Mark A. Johnson*

Sterling Chemistry Laboratory, Yale University, P.O. Box 208107, New Haven, Connecticut 06520

Jing Ding and Kenneth D. Jordan*

Department of Chemistry, University of Pittsburgh, Pittsburgh, Pennsylvania 15260

We report the spectral signatures of water molecules occupying individual sites in an extended H-bonding network using mass-selective, double resonance vibrational spectroscopy of isotopomers. The scheme is demonstrated on the water heptamer anion, $(H_2O)_7^-$, where we first randomly incorporate a single, intact D_2O molecule to create an ensemble of isotopomers. The correlation between the two OD stretching frequencies and that of the intramolecular DOD

bending transition is then revealed by photochemical modulation of the isotopomer population responsible for particular features in the vibrational spectrum. The observed patterns confirm the assignment of the dominant doublet, appearing most red-shifted from the free OD stretch, to a single water molecule attached to the network in a double H-bond acceptor (AA) arrangement. The data also reveal the unanticipated role of accidentally overlapping transitions, where the highest energy OD stretch, for example, occurs with its companion OD stretch obscured by the much stronger AA feature.

Because of the strong dependence of the OH stretching frequency on the H-bonding environment, vibrational spectroscopy has emerged as the method of choice for the structural assignment of the network shapes adopted by small water clusters.[255,256,257] There are, however, complications inherent to this method because anharmonic couplings [258] lead to large shifts from harmonic predictions, which makes it difficult to identify the spectral signatures of individual molecules in the network. This is especially true in cases like the anionic water clusters, where there are many isomers at play.[259, 260, 261] Here, we report an experimental method which isolates the vibrational features associated with a water molecule occupying a specific site within a particular structural isomer. This technique exploits pump-probe, isomer-selective, IR-IR double resonance (IR^2DR) vibrational spectroscopy[262] of mass-selected, Ar-tagged isotopomers generated by incorporation of a single, intact D_2O molecule in a field of H_2O molecules. We demonstrate this approach by applying it to explore the site-specific spectra of heavy water molecules in the highest electron binding isomer class [257, ,260] (type I and possibly I') of the Ar solvated water heptamer anion, $D_2O(H_2O)_6^-\cdot Ar_m$. Because the weaker binding classes (II and III) undergo fast vibrational autodetachment1 in the OH and OD stretching regions, only the high

binding class is available for application of this method, as it is the only one which yields sharp bands throughout the mid-infrared.

These experiments were carried out using the isomer selective spectroscopic strategy recently developed at Yale and described in detail in its application to the NO_2^--H_2O and $NO^+ \cdot (H_2O)_n$ systems.[262,263] Briefly, this method is based on photochemical hole burning in which both pump and probe excitations are carried out through vibrational transitions within the Ar-tagged predissociation regime. Three stages of mass selection are required to extract the isomer-selective signal, (i) isolation of a particular parent ion for interaction with the pump laser, (ii) rejection of unwanted, pump-induced photofragments prior to interaction of parent ions with the probe laser, and (iii) selective detection of the predissociation fragments arising from probe laser excitation of the same mass/charge ion packet isolated in step (i).

The photoproducts from the third separation stage are continuously monitored to record the population in a given ground-state level (and hence isotopomer) interrogated by the probe. All three mass-selection stages are carried out using time-of-flight techniques. In a typical experiment, the probe laser is tuned to a particular resonance while a powerful pump laser is scanned through the vibrational spectrum. This causes depletion in the probe signal when the two lasers are tuned to features which arise from the same isotopomer, so that the isotopomer-specific spectrum is recovered as a series of dips in the probe signal. Experimental details on ion preparation and laser parameters are included in the section at the end of the paper.

Figure 36 presents the (one-laser) argon predissociation [264] spectrum of $D_2O(H_2O)_6^-$. The bands are grouped into four distinct regions, the OH stretches (3000-3800 cm^{-1}, right side of Figure 36A), the OD stretches (2400-2800 cm^{-1}, left side of Figure 36A), the HOH bends (1500-1800 cm^{-1}, right side Figure 36B), and the DOD bends (1100-1300 cm^{-1}, left side Figure 36B).

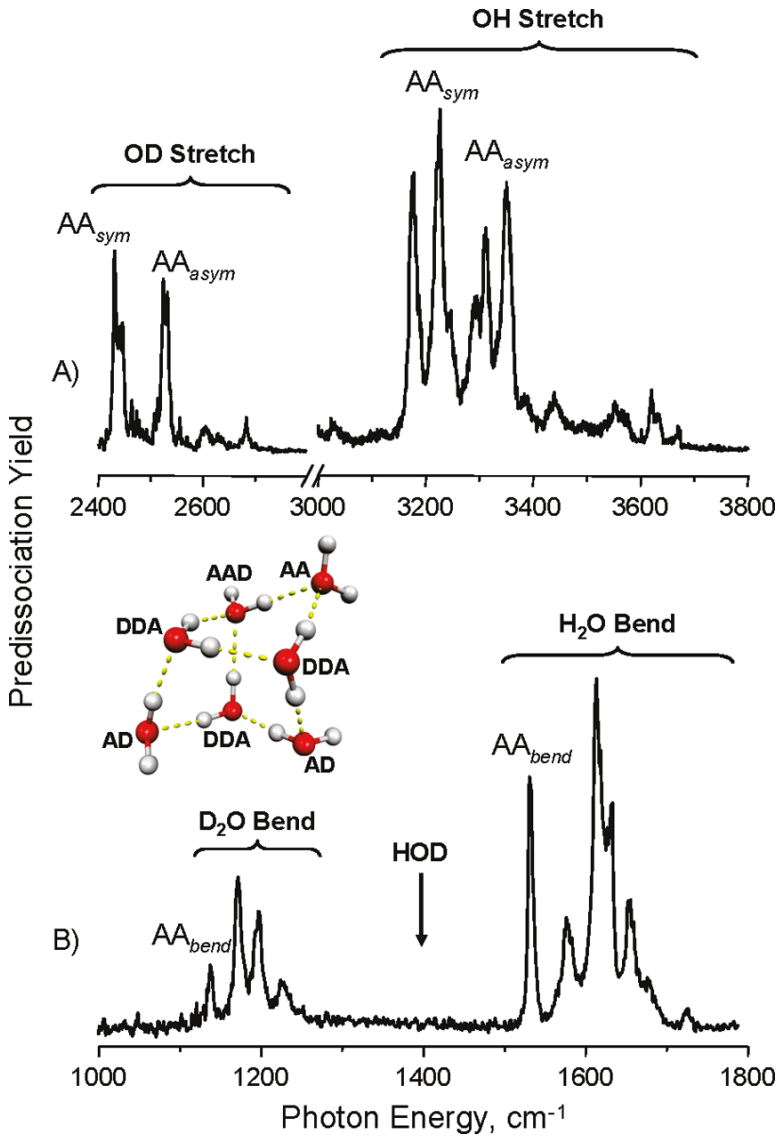

Figure 36. Ar predissociation spectrum of $D_2O(H_2O)_6^-\cdot Ar_m$ in the (A) OH and OD stretching regions and (B) HOH and DOD bending regions. The transitions nominally associated with the AA position are indicated in the stretching (sym and asym are symmetric and asymmetric stretches, respectively) and bending regions. A = H-bond acceptor, and D = H-bond donor in the site labels. The arrow indicates the location of the HOD bend fundamental in the isolated molecule. The lack of spectral features in this region establishes that the D_2O remains intact upon incorporation. The inset displays a representative minimum-energy structure identified earlier for the type I isomer.[255]

As reported previously,[265] there is no activity in the region of the HOD bending transitions (arrow in Figure 36B), which confirms that D_2O remains intact upon Ar cluster- mediated

condensation into the anionic hexamer clusters, $(H_2O)_6^-$·Ar_p. The plethora of bands associated with the OD stretches and D_2O bends indicates that the D_2O molecule occupies many (if not all) of the available sites, with the overall spectrum (Figure 36) appearing qualitatively similar to that of the perdeuterated isotopologue (Supporting Information).

There is consensus [255, 256, 266,267] that the isomers that bind the excess electron most strongly feature a unique water molecule bound to the network in a double H-bond acceptor (AA) motif, which allows it to orient both of its hydrogen atoms directly into the excess electron cloud. Unfortunately, the exact structural assignments of the heptamer anions in the type I (AA) isomer class are not yet available. It has been established, however, that only two distinct forms are generated under experimental conditions (denoted I and I'). It is therefore useful to anticipate the behavior expected for the site-specific vibrational patterns in the context of the calculated structures reported previously. Although there are many possible candidate structures, all of them feature the close-packing arrangement similar to that presented in the inset of Figure 36, which is the Pnf-a structure tentatively assigned to the experimentally observed isomer I vibrational spectrum.[255] Note that both the high binding type I and I' forms [268] yield similar vibrational patterns and are thus based on closely related structures. All candidates occur with water molecules in a variety of network sites (e.g., AAD, DDA, AD, and AA H-bonding configurations, where A=H -bond acceptor and D=H-bond donor). As such, this rather low-symmetry isomer class based on AA water attachment to the excess electron presents an excellent system with which to explore the spectral signatures of the different sites.

Figure 37 displays the calculated harmonic vibrational frequencies16 for the $D_2O(H_2O)_6^-$ isotopologue shown in Figure 36 in the DOD bending (MP2/aug-cc-pVDZ) and OD stretching (B3LYP [269]/6-31(1+,3+)G(d)[270]) regions. The top trace (A) corresponds to the net spectrum

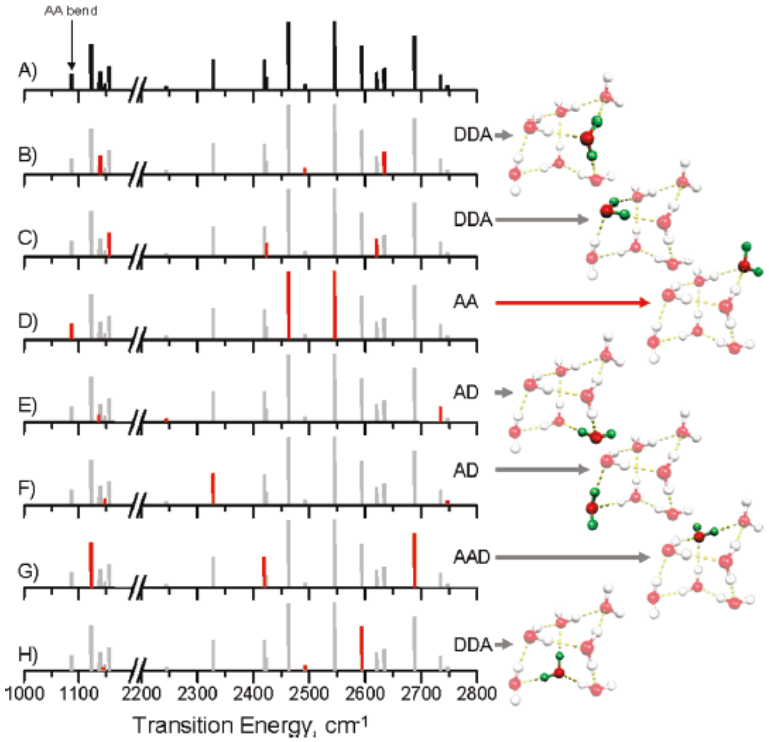

Figure 37. Calculated harmonic spectra of $D_2O(H_2O)_6^-$ in the DOD bend (MP2/aug-cc-pVDZ) and OD stretch (B3LYP/6-31(1+,3+)G*) regions. The calculated frequencies have been scaled by 0.93 and 0.974 in the bend and stretch regions, respectively. (A) Composite spectra of all seven isotopomers (assuming equal populations). The arrow indicates the calculated position of the DOD bend in the AA position. (B-H) Contributions (red sticks) of the individual isoptopomers with the D_2O molecule occupying each of the seven unique sites (in green). The overall spectrum (shown in gray) is included in each panel for reference.

expected for an ion ensemble with random incorporation of D_2O at all network sites, while the red sticks in traces B-H display the three fundamentals (two stretches and one bend) associated with the D_2O molecule in each of the seven unique network sites within this cluster, with the specific location highlighted by the colored water molecule in the structures on the right.

On the basis of the calculated spectra, [256] the two strongest OD stretching bands in small $(D_2O)_n^-$ clusters have been assigned to the symmetric and asymmetric stretching vibrations (denoted AA sym and AA asym in Figure 36A) of the deuterium atoms of the AA water pointing

into the excess electron cloud. In this assignment scheme, the unique AA molecule also accounts for the singular feature in the DOD bending region at 1138 cm^{-1} (denoted AA bend in Figure 36B) that is redshifted from the 1178 cm^{-1} band in free D_2O.[271] Because the bending transition of the AA water molecule is completely isolated in the spectrum, this band provides the cleanest transition with which to begin the exploration of the embedded patterns of the isotopomers. Note that the AD sites (Figure 37E and F) are calculated to exhibit the widest splitting between the two OD stretches, while the DDA sites (Figure 37B, C, and H) contribute closer doublets toward the center of the stretching region.

The discussion above indicates that, although the AA molecule is expected to contribute much of the intensity to the two dominant bands at the lower-energy range of the OD stretches, other sites also yield activity throughout this region. We therefore first used the double-resonance approach to survey the behavior of all isotopomers in which the D_2O molecule is not in the AA binding site, which is readily accomplished by fixing the probe laser on the unique HOH AA bend transition indicated in Figure 38A. The resulting dip spectrum is presented in Figure 38C, with the spectrum of all isotopomers (reproduced from Figure 36A) displayed in trace B. Interestingly, there are strong dips in the vicinity of the α and β bands that were nominally assigned to the AA molecule in previous reports, [255,256,258] along with the expected transitions from other non-AA sites that occur higher in energy (δ and γ). This establishes that the strong doublet (α and β) is actually comprised of several overlapping features, some of which do not involve the AA network site. Note that the dip intensities are quite different than the pattern observed in the nonselective scan. For example, the bands near α and γ appear with similar strength in the dip scan (panel C), while α is much more intense in the nonselective spectrum (panel B).

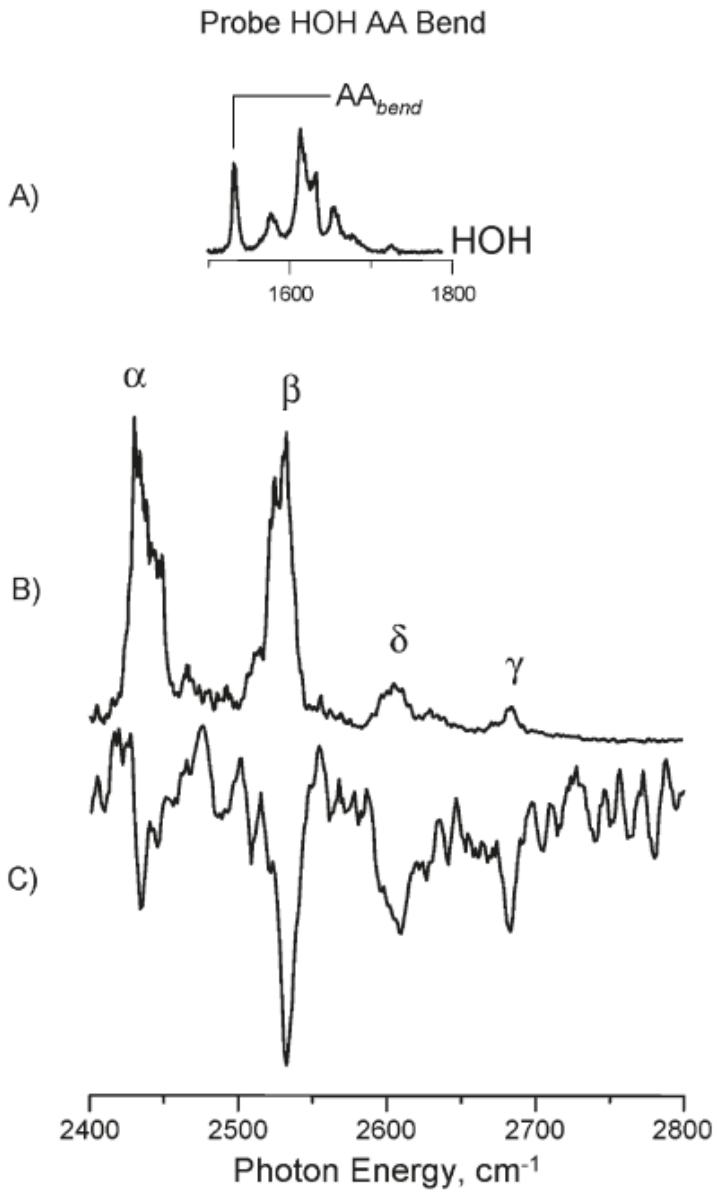

Figure 38. Ar predissociation spectrum of $D_2O(H_2O)_6^-$ Ar_5 in the (A) HOH bending region and (B) OD stretching region (reproduced from Figure 36B and A, respectively). (C) IR^2DR scan with the probe laser fixed at 1528 cm^{-1}, the energy of the AA HOH bend (indicated in trace A). Of note is that some intensity is recovered for all bands (α-γ), indicating that each of these peaks has contributions from non-AA sites.

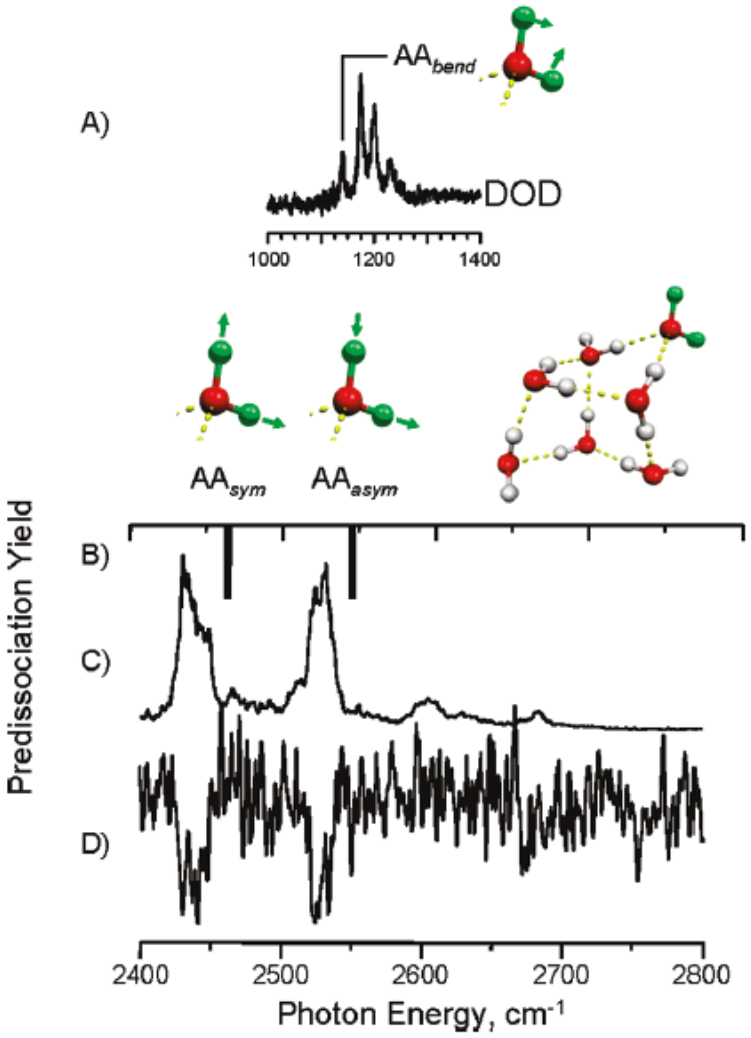

Figure 39. (A) Ar predissociation spectrum of $D_2O(H_2O)_6^-$·Ar_5 in the DOD bending region (reproduced from Figure 1B). (B) Calculated stick spectrum of $D_2O(H_2O)_6$h when D_2O occupies the AA position. (C) Ar predissociation spectrum of $D_2O(H_2O)_6^-$·Ar_5 in the OD stretching region (reproduced from Figure 36A). (D) IR^{2}DR scan with the probe laser fixed at 1138 cm^{-1}, the energy of the nominal AA DOD bend. The inset highlights the isotopically labeled position and the atomic displacements associated with the two fundamentals shown in (B).

Having identified the spectral profiles of the ensemble in which D_2O is not in the AA site, it is also of interest to recover the bands that are exclusively due to occupation of the AA site. This is accomplished by placing the probe laser on the low energy AA bend (D_2O) bending transition at 1138 cm^{-1}, indicated in Figure 39A. This was the most challenging experiment

carried out in this study because the laser power is quite weak at this probe frequency and D_2O occupation of the AA site upon condensation onto the hexamer anion is relatively ineffiecient. Figure 39D presents the resulting dip trace, and while compromised by limited signal-to-noise, it clearly reveals the two strong bands expected for the symmetric and asymmetric stretches of the AA water molecule, as indicated by the scaled harmonic values shown in Figure 39B. This result was expected based on previous theoretical analyses of the assignments,[256,266,267,272] but it is nonetheless useful to emphasize that this is the first independent experimental confirmation of the connectivity between the most red-shifted bending mode and the strong doublet in the OD stretching region.

The data in Figure 39 establish the spectral signature of the water molecule in the AA binding site by correlating the locations of the bands in the intramolecular bend and OD stretching regions. This is straightforward because of the fact that the bending mode associated with this molecule is well separated from the other transitions. Unfortunately, the other bands in the bending region are more congested, making them less useful in the isolation of the patterns arising from the other isotopomers. The OD stretching bands are more spread out, however, and offer another route to identify the embedded patterns by carrying out pump-probe measurements entirely within the higher-energy OD stretching region. Figure 40 presents the results of the double-resonance experiment carried out at two probe transitions located at the opposite ends of the OD stretching region. The top trace was obtained by fixing the probe laser on the γ band (trace E in Figure 40) at 2685 cm^{-1}, which is nominally associated with either an AD or AAD binding site in previous analyses.[258] Harmonic calculations universally predict that the highest frequency OH stretches should occur when the water molecule has the other H-atom strongly bound in an extended cycle or chain. The transition primarily derived from this bound hydrogen

displays a large red shift as a consequence of the cooperative enhancement of the H-bonds embedded in the homodromic sequence.[273,274,275,276,277,278,279,280,281] As an example, the calculated bands for the water molecule in the AAD site (highlighted in the inset) are shown in Figure 40B, which accurately account for the positions of the two dominant dip transitions associated with the γ transition, denoted OD_{AAD}(H-bond) and OD_{AAD}(free) in Figure 40B. Note that the observed lower energy OD_{AAD}(H-bond) dip is weaker than the higher-energy OD_{AAD}(free) feature, while the relative intensities of the two regions is just the opposite in the nonselective spectrum (Figure 40E). The characters of the OD_{AAD}(H-bond) and OD_{AAD}- (free) dips in Figure 40A are, in fact, similar to that observed when a H_2O molecule occupies the AA position (reproduced from Figure 38C in trace 40D, dotted red). The low-energy band thus assigned to the AAD site almost completely coincides with band α, nominally associated with the AA molecule, an identification that would have proven very difficult to establish without the use of the hole burning technique.

To further explore the extent of the heterogeneity at play in the α and β features, the probe laser was fixed at the lowest energy component within the α feature at 2431 cm^{-1}, which yielded the black dip trace shown in Figure 40D. Two strong bands are recovered in the vicinity of the α and β bands, as expected for the behavior of the AA D_2O molecule probed in the bending region (Figure 39D). The widths of both dips are indeed substantially narrower than the bands in 39D, however, which suggests that the AA site may accommodate multiple isomers with effectively degenerate DOD bends but slightly different OD stretches.

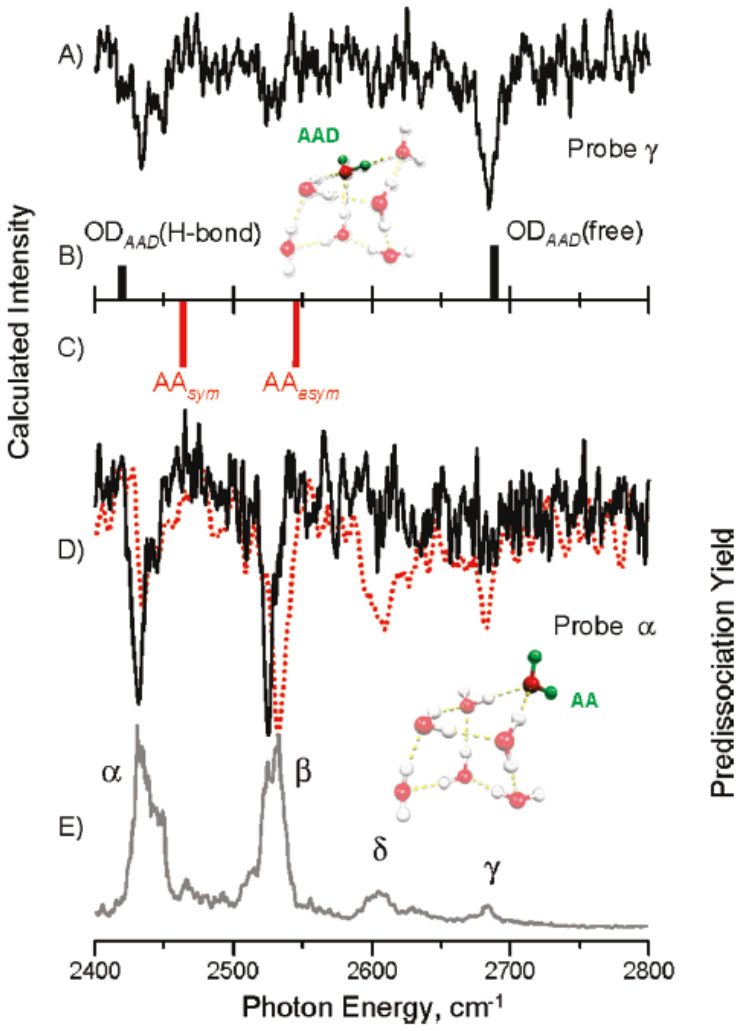

Figure 40. (A) IR^{2}DR spectrum in the OD stretching region with the probe laser fixed on the γ feature. (B, C) Calculated harmonic spectra (B3LYP/6-31(1+,3+)G*, scaled by 0.974) in the OD stretch region for the isotopomers with the location of the D_2O label indicated in green. Trace (B) corresponds to D_2O occupation in an AAD site, while (C) results from D_2O in the AA site. (D) Overlay of IR^{2}DR spectra in which the probe laser is fixed at the lower-energy portion of the R feature at 2431 (black) and 1528 cm^{-1} (dotted red, reproduced from Figure 38C), which corresponds to the AA(H_2O) bend transition. These two traces contrast the different spectral signatures arising from D_2O occupation of the AA site (black), as opposed to the other six positions available in the H-bond scaffold (dotted red). (E) Reproduction (from Figure 36A) of the Ar predissociation spectrum of $D_2O(H_2O)_6^-$· Ar_5 in the OD stretching region.

It is also useful to quantify the detailed nature of the overlap with other (i.e., non-AA) sites, and Figure 40D presents an overlay of the dip traces due to the D_2O molecule in the AA

site (black) and that resulting from D_2O occupation of the remaining locations (dotted red, reproduced from Figure 38C). The β feature is resolved into a very closely spaced doublet arising from different binding sites. Moreover, the non-AA band which contributes to the β feature is not present when γ is probed (Figure 40A). This establishes that it arises from a site without a dangling OH group, consistent with the behavior expected for the D_2O molecule in a DDA configuration such as that shown in Figure 37H.[282]

Systematic disentangling of all sites and definitive structural assignment of the rather complicated water heptamer anion are beyond the scope of this report describing the performance and type of information available from the site-specific spectra. It is useful to note, however, that even in the complex scenario presented by the heptamer (i.e., with seven unique network sites in a field of multiple isomers), we can extract many subtle features of the spectral correlations associated with particular sites. We are presently applying it to deduce the exact structures of the more technically demanding smaller clusters such as $(H_2O)_{4,5}^-$, which are much more difficult to synthesize with an intact D_2O molecule by Ar-mediated condensation because of their very low electron binding energies (see Experimental Section for details).

Finally, we remark that, although it is perhaps not surprising at the temperatures in play in the Ar-tagging regime (30-50 K), these observations of persistent hole burning arising from D_2O occupation of particular network sites provide the first conclusive evidence that the Ar tagged isotopomers are not, in fact, fluxional on the time scale of the experiment (~10 μs). The AAD site behavior is particularly compelling in this regard as the modulation signal obtained when monitoring the OD_{AAD}(free) band (γ) is unresponsive upon excitation near the very strong β feature (Figure 40A). This is significant because if there were rapid spectral diffusion, one would expect population to be removed from the entire ion ensemble according to the residence

times of D_2O in the various sites. In this context, there is an excellent opportunity to extend this method to warmer clusters [283] and thus identify the onset of intersite migration by observing the resulting spectral diffusion.

EXPERIMENTAL SECTION

The Ar-tagged water cluster anions were prepared by passing ~4 atm of Ar over a reservoir of water held at -3 ℃. This mixture was supersonically expanded and ionized by a counter propagating 1 keV electron beam.[284] The heavy water (D_2O) was then introduced into the vacuum chamber through a remote pulsed valve and becomes entrained in the expansion, as discussed in an earlier report.[265] The $D_2O(H_2O)_6^-{\cdot}Ar_m$ clusters are formed by Ar-mediated condensation onto $(H_2O)_6^-{\cdot}Ar_p$. This method was demonstrated [265] to incorporate an intact D_2O molecule (i.e., without scrambling of the H and D atoms between water molecules).We focus on the n = 7 case in this study because it is the smallest cluster anion that can be readily formed with an intact D_2O by Ar-mediated condensation. This occurs because n = 3-5 are only prepared in minor abundance by the ion source, limiting the production of $D_2O(H_2O)_{3\text{-}5}^-$. [265] Because of their very low electron binding energies, the anion dimer and trimer are not suitable to study the OH and OD stretches. This limitation occurs because the vibrational transitions are broadened by extremely rapid electron autodetachment.[255] Infrared light was generated by two independent Nd:YAG pumped OPO/OPA parametric converters (Laser Vision), each of which is equipped with an additional mixing stage based on $AgGaSe_2$.[285,286] This scheme provides sufficient energy (>5 mJ/pulse) to saturate infrared transitions over most of the 2400-4500 cm^{-1} range in a configuration where the laser is passed through the ion packet six times using a five-mirror arrangement housed inside of the vacuum envelope. All calculations were performed with the Gaussian 03 package.[131]

APPENDIX E

PHTOINITIATION OF VIBRATIONALLY-MEDIATED, INTRA-CLUSTER ELECTRON SCAVENGING THROUGH THE SOLVENT AND THE REACTANT: AN IR STUDY OF THE $[CH_3NO_2 \cdot (H_2O)_6]^-$ ANION

Manuscripts under preparation

Timothy L. Guasco, Kristin J. Breen, Jing Ding, Kenneth D. Jordan, Ryuzo Nakanishi, Takashi Nagata and Mark. A. Johnson.

Abstract

We report the photoinitiation of an intra-cluster electron capture reaction starting from the high-energy isomer of the $[(H_2O)_6 \cdot CH_3NO_2]^-$ cluster ion, a species that features accommodation of the excess electron in a diffuse orbital. This process is triggered by infrared excitation of vibrational transition localized on the water network as well as on the neutral CH_3NO_2 reactant. The photoproduct corresponds to the hydrated radical anion of nitromethane, $CH_3NO_2 \cdot (H_2O)_n$ on the basis of the observed energetic. The spectra of the reactive isomer (R) are isolated from bands associated with the product isomer (P) by selectively monitoring the photoproducts corresponding to the loss of the three water molecules. This channel is only open

for the high-energy isomer because the ~1.5eV required to evaporate three water molecules is much larger than the photon energy in the mid-infrared, and the necessary energy becomes available upon the release of the substantial exothermicity associated with the intracluster electron capture process. The vibrational spectrum of the R isomer is dramatically different than that obtained from isomer P, such that the R spectrum displays sharp bands that are remarkably similar to those found in the type I isomer of the isolated $(H_2O)_6^-$ reactant anion. This observation establishes that the binding site of the diffuse excess electron remains largely intact in the isomer R structure. C-H and N-O stretching bands are also observed and confirm the presence of neutral CH_3NO_2 in the R isomer composition. These results indicate that the vibrational excitation of both the water network and the CH_3NO_2 reactant molecule can efficiently drive the intramolecular electron capture reaction, even when these transitions occur in the low-energy region of the N-O stretching vibrations.

BIBLIOGRAPHY

[1] D. Marx. ChemPhysChem. 2006, 7, 1848.

[2] N. I. Hammer, J-W. Shin, J. M. Headrick, E. G. Diken, J. R. Roscioli, G. H. Weddle, M. A. Johnson. Science 2004, 306, 675.

[3] M. R. Walsh, C. A. Koh, E.D. Sloan, A. K. Sum, D. T. Wu. Science 2009, 326, 1095.

[4] J.-W. Shin, N. I. Hammer,1 E. G. Diken, M. A. Johnson. R. S. Walters, T. D. Jaeger, M. A. Duncan, R. A. Christie, K. D. Jordan. Science 2004, 304, 1137.

[5] K. D. Jordan, M. A. Johnson. Science 2010, 329, 42.

[6] A.E. Bragg, J.R.Verlet, A. Kammrath, O. Cheshnovsky, D. M. Neumark. J. Am. Chem. Soc. 2005, 127, 15283.

[7] K.R. Siefermann, Y. Liu, E. Lugovoy, O. Link, M. Faubel, U. Buck, B. Winter, B. Abel. Nature Chem. 2010, 2, 274.

[8] J. R. R. Verlet, A. E. Bragg, A. Kammrath, O. Cheshnovsky, D. M. Neumark, Science 2005, 310, 1769.

[9] L. Turi, W.-S. Sheu, P. J. Rossky. Science 2005, 309, 914.

[10] J. R. R. Verlet, A. E. Bragg, A. Kammrath, O. Cheshnovsky, D. M. Neumark. Science 2005, 307, 93.

[11] N. I. Hammer, J. R. Roscioli, J. C. Bopp, J. M. Headrick, M. A. Johnson. J. Chem. Phys. 2005, 123, 244311.

[12] J.R. Roscioli, N.I. Hammer, M.A. Johnson. J. Phys. Chem. A. 2006, 110, 7517.

[13] E.b. Wilson, J.C. Decius,P.C. Cross. Molecular Vibrations: The Theory of Infrared and Raman Vibrational Spectra. Dover Pulication, 1980.

[14] D. A. McQuarrie, Statistical Mechanics. Harper & Row, New York, 2000.

[15] R. P. Feynman, Statistical Mechanics. Westview, Boulder,CO, 1972.

[16] F. Paesani, W. Zhang, D. A. Case, T. E. Cheatham III, G. A. Voth. J. Chem. Phys. 2006, 125, 184507.

[17] S. M. Woodley, R. Catlow. Nature Materials 2008, 7, 937.

[18] M. A. Neumann, F. J. J. Leusen, J. Kendrick. A Major Angew. Chem. Int. Ed. 2008, 47, 2427.

[19] A. Asmadi, J. Kendrick, F. J. J. Leusen. Chem. Eur. J. 2010, 16, 12701.

[20] A. Defusco, D.P. Schofield, K. D. Jordan. Mol. Phys. 2007, 105, 2681.

[21] R. Kumar, F-F. Wang, G. R. Jenness, K. D. Jordan. J. Chem. Phys. 2010, 132, 014309.

[22] B. Jeziorski, R. Moszynski, K. Szalewicz. Chem. Rev.1994, 94, 1887.

[23] R. E. Larsen, W. J. Glover, B. J. Schwartz. Science 2010, 329, 65.

[24] L. Ma, K. Majer, F. Chirot, B. von Issendorff. J. Chem. Phys. 2009, 131, 144303.

[25] R. G. Parr, W. Yang. Density-Functional Theory of Atoms and Molecules. 1989, Oxford University Press, New York.

[26] P. Cieplak, F-Y. Dupradeau, Y. Duan, J. Wang. J. Phys.: Condens. Matter 2009, 21, 333102.

[27] W. D. Cornell, P. C., Christopher, I. Bayly, I. R. Gould, K. M. Merz, D. M. Ferguson, D. C. Spellmeyer, T. Fox, J. W. Caldwell, P. A. Kollman. J. Am. Chem. Soc. 1995, 117, 5179.

[28] A. D. MacKerell, D. Bashford, M. Bellott, R. L. Dunbrack, J. D. Evanseck, M. J. Field, S. Fischer, J. Gao, H. Guo, S. Ha, D. Joseph-McCarthy, L. Kuchnir, K. Kuczera, F. T. K. Lau, C. Mattos, S. Michnick, T. Ngo, D. T. Nguyen, B. Prodhom, W. E. Reiher, B. Roux, M. Schlenkrich, J. C. Smith, R. Stote, J. Straub, M. Watanabe, J. Wiorkiewicz Kuczera, D. Yin, M. Karplus. J. Phys. Chem. B 1998, 102, 3586.

[29] W. L. Jorgensen, D. S. Maxwell, J. Tirado-Rives. J. Am. Chem. Soc. 1996, 118, 11225.

[30] L. D. Schuler, X. Daura, W.F. van Gunsteren. J. Comput. Chem. 2001, 22, 1205.

[31] N. L. Allinger, H. Y. Young, J. H. Lii. J. Am. Chem. Soc. 1989, 111, 8551.

[32] N. L. Allinger, K. H. Chen, J. H. Lii, K. A. Durkinm. J. Comput. Chem. 2003, 24, 1447.

[33] A. Rappe, C.J. Casewit, K. S. Colwell, W. A. Goddard, W. M. Skiff. J. Am. Chem. Soc. 1992, 114, 10024.

[34] T. A. Halgren, W. Damm. Curr. Opin. Struct. Biol. 2001, 11,236.

[35] B. Guillot. J. Mol. Liq. 2002, 101, 219.

[36] H.J.C. Berendsen, J.P.M. Postma, W.F. van Gunsteren, and J. Hermans, In *Intermolecular Forces*, edited by B. Pullman. Reidel, Dordrecht, 1981, p331.

[37] M. Jeziorska, P. Jankowski, K. Szalewicz, B. Jeziorski. J. Chem. Phys. 2000, 113, 2957.

[38] E. M. Mas, R. Bukowski, K. Szalewicz, G. C. Groenenboom, P. E. S. Wormer, A. van der Avoird. J. Chem. Phys. 2000, 113, 6687.

[39] G. C. Groenenboom, P. E. S. Wormer, A. van der Avoird, E. M. Mas, R. Bukowski, K. Szalewicz. J. Chem. Phys. 2000, 113, 6702.

[40] M. Torheyden, G. Jansen. Mol. Phys. 2006,104, 2101.

[41] I. C. Hayes, A. J. Stone. Mol. Phys. 1984, 53, 83.

[42] N. Gresh, G. A. Cisneros, T. A. Darden, J-P Piquemal. J. Chem. Theory Comput. 2007, 3, 1960.

[43] A. Warshel, M. Kato, A. V. Pisliakov. J. Chem. Theory Comput. 2007, 3, 2034.

[44] E. M. Mas, R. Bukowski, K. Szalewicz. J. Chem. Phys. 2003, 118, 4404.

[45] C. Chipot, J. G. Angyan. New J. Chem. 2005, 29, 411.

[46] A. Warshel, M. J. Levitt. Mol. Biol. 1976, 103, 227.

[47] J. Anwar, D. Zahn. Angew. Chem. Int. Ed. 2011, 50, 1996.

[48] S. W.Rick, S. J. Stuart. Rev. Comput. Chem.2002, 18 89–146.

[49] M. Matsumoto, S. Saito, I. Ohmine. Nature, 2002, 416, 409.

[50] B. T. Thole. Chem. Phys. 1981, 59, 341.

[51] S. S. Xantheas, C. J. Burnham, R. J. Harrison, J. Chem. Phys. 2002, 116, 1493.

[52] S. W.Rick, S. J.Stuart, B. J.Berne. J. Chem. Phys. 1994, 101, 6141.

[53] D. M. York, W. T. Yang. J. Chem. Phys. 1996, 104, 159.

[54] S. Patel, C. L. Brooks. J. Comput. Chem. 2004, 25, 1.

[55] H. B. Yu, T. Hansson, W. F. van Gunsteren. J. Chem. Phys. 2003, 118, 221.

[56] P. Day, J. H. Jensen, M. S. Gordon, S. P. Webb, W. J. Stevens, M. Krauss, D. R. Garmer, H. Basch, D. Cohen. J. Chem. Phys. 1996, 105, 1968.

[57] C. J. Millot, J. C. Soetens, M. P. Hodges, A. J. Stone. J. Phys. Chem. A. 1998, 102, 754.

[58] J. G. Angyan, C. Chipot, F. Dehez, C. Hattig, G. Jansen, C. Millot. J. Comput. Chem. 2003, 24, 997.

[59] J. W. Ponder, C. Wu. J. Phys. Chem. B. 2010, 114, 2549.

[60] L.X. Dang, T. M. Chang. J. Chem. Phys. 1997, 106, 8149.

[61] W. L. Jorgensen, J. Chandrasekhar, J. D. Madura, R. W. Impey, M. L Klein, J. Chem. Phys. 1983, 79, 926.

[62] M. W. Mahoney, W. L. Jorgensen. J. Chem. Phys. 2000, 112, 8910.

[63] P. Ren, J. W. Ponder. J. Phys. Chem. B. 2003, 107, 5933.

[64] H. A. Stern, F. Rittner, B. J. Berne, R. A. Friesner. J. Chem. Phys. 2001, 115, 2237.

[65] P. T. Kiss, A. Baranyai. J. Chem. Phys. 2009, 131, 204310.

[66] J. K. Gregory, D. C. Clary, K. Liu, M. G. Brown, R. J. Saykally. Science 1997, 275, 814.

[67] F. J. Lovas, J. Phys. Chem. Ref. Data 1978, 7, 1445.

[68] Y. S. Badyal, M.-L. Saboungi, D. L. Price, S. D. Shastri, D. R. Haeffner. J. Chem. Phys. 2000, 112, 9206.

[69] P. L. Silvestrelli, M. Parrinello. Phys. Rev. Lett. 1999, 82, 3308.

[70] P. Soderhjelm, J. W. Krogh, G. Karlstrom, U. Ryde, R. Lindh, J. Comput. Chem. 2007, 28, 1083.

[71] A.N Holt, J. Bostr, G. Karlstr, R. Lindh. J. Comput. Chem. 2010, 31,1583.

[72] G. Andrés Cisneros,J-P. Piquemal, T. A. Darden. J. Chem. Phys. 2005, 123, 044109.

[73] A. J. Stone. The Theory of Intermolecular Forces. Oxford University Press, Oxford, UK, 2000.

[74] C. Chipot, B. Maigret, J-L. Rivail, H. A. Sheraga. J. Phys. Chem. 1992, 96, 10276.

[75] R. F. W. Bader, Atoms in Molecules–A Quantum Theory, Oxford University Press, London, 1990.

[76] F. H. Stillinger, A. Rahman. J. Chem. Phys. 1974, 60, 1545-1557.

[77] S-B. Zhu, S. Singh, G. W. Robinson. J. Chern. Phys. 1991, 15, 95.

[78] J. M. Hermida-Ramon, S. Brdarski, G. Karlstrom, U. Berg. J. Comput. Chem. 2003, 24 161.

[79] D. P. Geerke, W.F. van Gunsteren. J. Chem. Theory. Comput. 2007, 3, 2128.

[80] Stone, A. J. Chem. Phys. Lett. 1981, 83, 233.

[81] K. Muller-Dethlefs, P. Hobza. Chem. Rev. 2000, 100, 143.

[82] A. Cembran, P. Bao, Y. Wang, L. Song, D. G. Truhlar, J. Gao. J. Chem. Theory. Comput. 2010, 6, 2469.

[83] F. Cinquini, C. D.Valentin, E. Finazzi, L. Giordano, G. Pacchioni. Theor. Chem. Acc. 2007, 117, 827.

[84] J. G. Angyan, C. Chipot. Int. J. Quant. Chem. 1994, 52, 17.

[85] K. T.Tang, J. P. Toennies. J. Chem. Phys. 1984, 80, 3726.

[86] D. E.Williams. J. Comput. Chem. 1988, 9, 745.

[87] P. Day, J. H. Jensen, M. S. Gordon, S. P. Webb, W. J. Stevens, M. Krauss. J Chem Phys. 1996, 105, 1968.

[88] J.-P. Piquemal, G. A. Cisneros, P. Reinhardt, N. Gresh, and T. A. Darden. J. Chem. Phys. 2006, 124, 104101.

[89] D. M. Elking, G. A. Cisneros, J-P. Piquemal, T. A. Darden, L. G. Pedersen. J. Chem. Theory Comput. 2010, 6, 190.

[90] M. A.Freitag, M. S.Gordon, J. H.Jensen, W. J.Stevens. J. Chem. Phys. 2000, 112, 7300

[91] J. P.Piquemal, N.Gresh, C.Giessner-Prettre. J. Phys. Chem. A 2003, 107, 10353

[92] G. A. Cisneros, S. Tholander, O. Parisel, O, T. A. Darden, D. Elking, L. Perera, J. P. Piquemal. Int. J. Quantum Chem. 2008, 108, 1905.

[93] B. Wang, D. G. Truhlar. J. Chem. Theory Comput. 2010, 6, 3330.

[94] J. N. Murrell, J. J. C. Teixeira-Dias, Mol. Phys. 1970, 19, 521.

[95] H. F. J. Savage, J. L.Finney. Nature 1986, 322, 717.

[96] S. Creuzet, J. Langlet, N. Gresh. J Chim-Phys Phys Chim Biol. 1991, 88, 2399.

[97] C. Millot, A.J. Stone. Mol. Phys. 1992, 77, 439.

[98] A. J. Stone. Science. 2008, 321, 787.

[99] K. Ichikawa, Y. Kameda, T. Yamaguchi, H. Wakita, M. Misawa, Mol. Phys. 1991, 73, 79.

[100] V. F. Petrenko, R. W. Whitworth, Physics of Ice. Oxford University Press, New York, 1999, pp. 31–33.

[101] C. Baianu, N. Boden, D. Lightowlers, M. Mortimer, Chem. Phys. Lett. 1978, 54, 169.

[102] W. F. Kuhs, M. S. Lehmann, J. Phys. Chem. 1983, 87, 4312.

[103] R. Car, M. Parrinello, Phys. Rev. Lett. 1985, 55, 2471.

[104] D. D. Kemp, M. S. Gordon. J. Phys. Chem. A, 2008, 112 , 4885.

[105] G. S. Fanourgakis, S. S. Xantheas. J. Chem. Phys. 2006, 124, 174504,

[106] M. Allesch, E. Schwegler, F. Gygi, G. Galli. J. Chem. Phys. 2004, 120, 5192.

[107] S. L. Price. Phys. Chem. Chem. Phys., 2008, 10, 1996.

[108] J.-W. Shin, N. I. Hammer, E. G. Diken, M. A. Johnson, R. S. Walters, T. D. Jaeger, M. A. Duncan, R. A. Christie, K. D. Jordan, , Science 2004, 304, 1137.

[109] M. S. Bergen, D. Schuh, M. G. Sceats, S. A. Rice. J. Chem. Phys. 1978, 69, 3477.

[110] J. R. Reimers, R. O. Watts. Chem. Phys. 1984, 91, 201.

[111] K. Toukan, A. Rahman. Phys. Rev. B 1985, 31, 2643.

[112] D. M. Ferguson. J. Comput. Chem. 1995, 16, 501.

[113] L. X. Dang, B. M. Petit. J. Phys. Chem. 1987, 91, 3349.

[114] C. J. Burnham, G. F. Reiter, J. Mayers, T. Abdul-Redah, H. Reichertc, H. Dosch. Phys. Chem. Chem. Phys. 2006, 8, 3966.

[115] E. Harder, J. D. Eaves, A. Tokmakoff, B. J. Berne. PNAS, 2005, 102, 11611.

[116] C. J. Burnham and S. S. Xantheas. J. Chem. Phys. 2002, 116, 5115.

[117] G. S. Fanourgakis, S. S. Xantheas. J. Phys. Chem. A 2006, 110, 4100.

[118] G. S. Fanourgakis, S. S. Xantheas, J. Chem. Phys. 2008, 128, 074506.

[119] C. J. Burnham, D. A. Anick, P. K. Mankoo, G. F. Reiter J. Chem. Phys. 2008, 128, 154519.

[120] C. J. Burnham, S. S. Xantheas. J. Chem. Phys. 2002, 116, 1500.

[121] C. J. Burnham, S. S. Xantheas. J. Chem. Phys. 2002, 116, 1479.

[122] A. J. Stone. Science 2008, 321, 787.

[123] S. F. Boys, F. Bernardi. Mol. Phys. 1970, 19, 553.

[124] H. Partridge, D. W. Schwenke. J. Chem. Phys. 1997, 106, 4618.

[125] P. T. van Duijnen, M. Swart. *J. Phys. Chem. A*, 1998, 102, 2399.

[126] P. K. Mankoo, T. Keyes. J. Chem. Phys. 2008, 129, 034504.

[127] B. J. Smith, D. J. Swanton, J. A. Pople, H. F. Schaefer III, L. Radom, J. Chem. Phys. 1990, 92, 1240.

[128] R. A. Kendall, R. J. Harrison. J. Chem. Phys. 1992, 96, 6769.

[129] H.-J. Werner, F. R. Manby, P. J. Knowles. J. Chem. Phys. 2003, 118, 8149.

[130] MOLPRO is a package of *ab initio* programs by H.-J. Werner,et al.

[131] Gaussian 03, Revision C.02, M. J. Frisch, et al. Gaussian Inc., Wallingford CT, 2004.

[132] SAPT 2008, by R. Bukowski, et al. Chem. Rev. 1994, 94, 1887.

[133] J. Wang, P. A. Kollman. J. Comput. Chem. 2001, 22, 1219.

[134] GAlib, a C++ Library of Genetic Algorithm Components by Matthew Wall. See http://lancet.mit.edu/ga/

[135] A. K. Soper. Chem. Phys. 2000, 258, 121.

[136] G. A. Cisneros, J. P. Piquemal, T. A. Darden. J. Chem. Phys. 2005, 123, 044109.

[137] T. C. Lillestolen, R. J. Wheatley. J. Phys. Chem. A 2007, 111, 11141.

[138] G. J. Williams, A. J. Stone. J. Chem. Phys. 2003, 119, 4620.

[139] C. Le Sueur, A. Stone. J. Mol. Phys. 1994, 83, 293.

[140] J. Angyan, G. Jansen, M. Loos, C. Hattig, B. A. Hess. Chem. Phys. Lett. 1994, 219, 267.

[141] A. J. Misquitta, A. J. Stone, S. L. Price. J. Chem. Theory Comput. 2008, 4, 19.

[142] A. J. Stone, A. J. Misquitta. Int. Rev. Phys. Chem. 2007, 26, 193.

[143] A. J. Stone. A. J. Misquitta. Chem. Phys. Lett. 2009, 473, 201.

[144] R. Z. Khaliullin, E. A. Cobar, R. C. Lochan, A. T. Bell, M. Head-Gordon, J. Phys. Chem. A 2007, 111, 8753.

[145] N. Gresh. J. Comput. Chem. 1995, 16, 856.

[146] N. Gresh. J. Phys. Chem. A 1997, 101, 8680.

[147] J. H. Jensen, P. N. Day, M. S. Gordon, H. Basch, D. Cohen, D. R.Garmer, M. Krauss, W. J. Stevens in "Modeling the Hydrogen Bond" (D.A. Smith, ed.) ACS Symposium Series 1994, 569, pp 139.

[148] S. Brdarski, G. Karlstro1m. J. Phys. Chem. A 1998, 102, 8182.

[149] CFOUR, Coupled-Cluster techniques for Computational Chemistry**,** a quantum-chemical program package by J. F. Stanton, et. al.

[150] R. Bukowski, K. Szalewicz, G. C. Groenenboom, A. Avoird. J. Chem. Phys. 2008, 128, 094313.

[151] Y. Wang, B. C. Shepler, B. J. Braams, J. M. Bowman. J. Chem. Phys. 2009, 131, 054511.

[152] F-F. Wang, K. D. Jordan. unpublished results.

[153] F. Wang, K. D. Jordan. Annul. Rev. Phys. Chem. 2003, 54, 367.

[154] P. Skurski, M. Gutowski, J. Simon. Int. J. Quant. Chem. 2000, 80, 1024.

[155] F. Wang, K. D. Jordan. J. Chem. Phys. 2001, 114, 10717.

[156] Sommerfeld, T.; Jordan, K. D. J. Phys. Chem. A 2005, 109, 11531

[157] T. Sommerfeld, A. DeFusco, K. D. Jordan. J. Phys. Chem. A 2008, 112, 11021.

[158] T. Sommerfeld, K. D. Jordan. J. Phys. Chem. A 2005, 109, 11531.

[159] T. Koopmans. Physica. 1934, 1, 104.

[160] M. Gutowski, P. Skurski, K. D. Jordan, J. Simons. J. Int. J. Quantum Chem. 1997, 64, 183

[161] T-H. Choi, T. Sommerfeld, S. L. Yilmaz, K. D. Jordan. J. Chem. Theory. Comp. 2000, 6, 2388.

[162] L. Kevan. Acc. Chem. Res. 1981, 14, 138.

[163] L. D. Jacobson, J. M. Herbert. J. Chem. Phys. 2010, 133, 154506.

[164] P. W. Atkins. Physical Chemistry, 7th ed. Freeman, New York, 2002.

[165] G. Zundel. In The Hydrogen Bond: Recent Developments in Theory and Experiment; Schuster, P., Zundel, G., Sandorfy, C., Eds.; North-Holland: Amsterdam, 1976; Vol. II, p 683

[166] P. A. Giruere, S. Turrel. Can. J. Chem. 1976, 54, 3477.

[167] N. B. Librovich, V. P. Sakun, N. D. Sokolov. Chem. Phys. 1979, 39, 351.

[168] M. Eigen, E. Wicke. J. Phys. Chem. 1954, 58, 702.

[169] G. Zundel, H. Z. Metzger. Phys. Chem. (Muenchen, Ger.) 1968, 58, 225.

[170] N. Agmon. Chem. Phys. Lett. 1995, 244, 456.

[171] L. L. Yeh, M. Okumura, J. D. Myers, J. M. Price, Y. T. Lee .J. Chem. Phys. 1989, 91, 7319.

[172] K. R. Asmis,N. L. Pivonka, G. Santambrogio, M. Brummer, C. Kaposta, D. M. Neumark, L. Woste. Science 2003, 299, 1375.

[173] T. D. Fridgen, T. B. McMahon, L. MacAleese, J. Lemaire, P. Maitre. J. Phys. Chem. A 2004, 108, 9008.

[174] J. M. Headrick, J. C. Bopp, M. A. Johnson. J. Chem. Phys. 2004, 121, 11523.

[175] J.-C. Jiang, Y.-S. Wang, H.-C. Chang, S. H. Lin, Y. T. Lee, G. Niedner-Schatteburg, H.-C. Chang. J. Am. Chem. Soc. 2000, 122, 1398.

[176] J. M. Headrick, E. G. Diken, R. S. Walters, N. I. Hammer, R. A. Christie, J. Cui, E. M. Myshakin, M. A. Duncan, M. A. Johnson, K. D. Jordan. Science 2005, 308, 1765.

[177] N. I. Hammer, E. G. Diken, J. R. Roscioli, M. A. Johnson, E. M. Myshakin, K. D. Jordan, A. B. McCoy, J. M. Bowman, S. Carter. J. Chem. Phys. 2005, 122, 244301.

[178] L. McCunn, J. R. Roscioli, M. A. Johnson, A. B. McCoy. J. Phys. Chem. B 2008, 112, 321.

[179] M. Kaledin, A. L. Kaledin, J. M. Bowman. J. Phys. Chem. A 2006, 110, 2933.

[180] O. Vendrell, F. Gatti, H.-D. Meyer. Angew. Chem., Int. Ed. 2007, 46, 6918.

[181] O. Vendrell, F. Gatti, H.-D. Meyer. J. Chem. Phys. 2007, 127, 184303.

[182] M. H. Beck, A. Jackle, G. A. Worth, H.-D. Meyer. Phys. Rep. 2000, 234, 1.

[183] X. Huang, B. J. Braams, J. M. Bowman. J. Chem. Phys. 2005, 122, 044308.

[184] J. Sauer, J. Dobler. ChemPhysChem 2005, 6, 1706.

[185] M. Park, I. Shin, N.J. Singh, K. S. Kim. J. Phys. Chem. A 2007,111, 10692.

[186] J. P. Devlin,M. W. Severson, F. Mohamed, J. Sadlej, V. Buch, M. Parrinello. Chem. Phys. Lett. 2005, 408, 439.

[187] R. Car, M. Parrinello. Phys. Rev. Lett. 1985, 55, 2471.

[188] D. Marx, J. Hutter. In Modern Methods and Algorithms of Quantum Chemistry; Grotendorst, J., Ed. Germany, 2000, pp 301-449.

[189] A. D. Becke. Phys. Rev. A 1988, 38, 3098.

[190] C. Lee, W. Yang, R. C. Parr. Phys. Rev. B 1988, 37, 785.

[191] N. Troullier, J. L. Martins. Phys. Rev. B 1991, 110, 2810.

[192] J. Martyna, M. E. Tuckerman. J. Chem. Phys. 1999, 110, 2810.

[193] S. Nosé Mol. Phys. 1984, 52, 255.

[194] S. Nosé J. Chem. Phys. 1984, 81, 511.

[195] W. G. Hoover. Phys. Rev. A 1985, 31, 1695.

[196] P. P. Kumar, D. Marx. Phys. Chem. Chem. Phys. 2006, 8, 573.

[197] I.-F.Kuo, C. J. Mundy, M. J . McGrath, J. I. Siepmann. J. Chem. Theory Comput. 2006, 2, 1274.

[198] R. Ramirez, T. López-Ciudad, T, P. P. Kumar, D. Marx. J. Chem. Phys. 2004, 121, 3973.

[199] P. H. Berens, K. R. Wilson. J. Chem. Phys. 1981, 74, 4872.

[200] J. Hutter, et al. CPMD. http://www.cpmd.org/. Copyright IBM Corp.1990-2006. Copyright Stuttgart 1997-2001.

[201] L. R. McCunn, J. R. Roscioli, M. A. Johnson, A. B. McCoy. J. Phys. Chem. B 2008, 112, 321.

[202] L. R. McCunn, L. J. R. Roscioli, B. M. Elliott, M. A. Johnson, A. B. McCoy. J. Phys. Chem. A 2008, 112, 6074.

[203] O. Vendrell, F. Gatti, H-D. Meyer. Angew. Chem. Int. Ed. 2009, 48, 352.

[204] M. Okumura, L. L. Yeh, J. D. Myers, Y. T. Lee. J. Chem. Phys. 1986, 85, 2328.

[205] P. Ayotte, G. H. Weddle, J. Kim, M. A. Johnson. J. Am. Chem. Soc. 1998, 120, 12361

[206] C. G. Bailey, J. Kim, C. E. H. Dessent, M. A. Johnson. Chem. Phys. Lett. 1997, 269, 122.

[207] P. Ayotte, C. Bailey, G. H. Weddle, M. A. Johnson. J. Phys. Chem. A 1998, 102, 3067.

[208] M. S. Johnson, K. T. Kuwata, C-K. Wong, M. Okumura. Chem. Phys. Lett. 1996, 260, 551.

[209] P. Ayotte, J. A. Kelley, S. B. Nielsen, M. A. Johnson. Chem. Phys. Lett. 2000, 316, 455.

[210] E. G. Diken, J. M. Headrick, J. R. Roscioli, J. C. Bopp, M. A. Johnson, A. B. McCoy, X. Huang, S. Carter, J. M. Bowman. J. Phys. Chem. A 2005, 109, 571.

[211] W. H. Robertson, E. A. Price, J. M. Weber, J. W. Shin, G. H. Weddle, M. A. Johnson. J. Phys. Chem. A 2003, 107, 6527.

[212] E. M. Myshakin, K. D. Jordan, W. H. Robertson, G. H. Weddle, M. A. Johnson, J. Chem. Phys. 2003, 118, 4945.

[213] M. Kolaski, H. M. Lee, Y. C. Choi, K. S. Kim, P. Tarakeshwar, D. J. Miller, J. M. Lisy. J. Chem. Phys. 2007, 126.

[214] J. R. Roscioli, N. I. Hammer, M. A. Johnson, K. Diri, K. D. Jordan. J. Chem. Phys. 2008, 128, 104314.

[215] B. M. Elliott, R. A. Relph, J. R. Roscioli, J. C. Bopp, G. H. Gardenier, T. L.Guasco, M. A. Johnson. J. Chem. Phys. 2008, in press.

[216] F. A. Ensminger, J. Plassard, T. S. Zwier, S. Hardinger. J. Chem. Phys. 1993, 99, 8341.

[217] A. D. Becke. J. Chem. Phys. 1993, 98, 5648.

[218] C. Lee, W. Yang, R. G. Parr. Phys. Rev. B 1988, 37, 785.

[219] P. J. Stephens, F. J. Devlin, C. F. Chabalowski, M. J. Frisch. J. Phys. Chem. 1994, 98, 11623.

[220] A. D. Becke. Phys. Rev. A 1988, 38, 3098.

[221] R. A. Kendall, T. H. Dunning, R. J. Harrison. J. Chem. Phys. 1992, 96, 6796.

[222] D. E. Woon, T. H. Dunning. J. Chem. Phys. 1993, 98, 1358.

[223] M. A. Johnson. Stanford University, 1983.

[224] J. M.Smith, X.Zhang, J. L.Knee. J. Chem. Phys. 1993, 99, 2550.

[225] D. H.Paik, I.-R.Lee, D.-S.Yang, J. S.Baskin, A. H. Zewail. Science 2004, 306, 672.

[226] M. A. Johnson, M. A, W.C. Lineberger, W. C. Pulsed Methods for Cluster Ion Spectroscopy. In Techniques for the Study of Ion-Molecule Reactions; Farrar, J. M., Saunders, W. H., Jr., Eds.; Wiley: New York, 1988; Vol.XX; p 591.

[227] W. H. Robertson, J. A. Kelley, M. A. Johnson. Rev. Sci. Instrum. 2000, 71, 4431.

[228] J. A. Stearns, A. Das, T. S. Zwier. Phys. Chem. Chem. Phys. 2004, 6, 2605.

[229] M. Gerhards, C. Unterberg, A. Gerlach. Phys. Chem. Chem. Phys. 2002, 4, 5563.

[230] E. M. Myshakin, E. L.Sibert III, M. A. Johnson,K. D. Jordan. J. Chem. Phys. 2003, 119, 10138.

[231] M. Head-Gordon, J. A. Pople, J. M. J. Frisch. Chem. Phys. Lett. 1988, 153, 503.

[232] C. Peng, H.B. Schlegel. Isr. J. Chem. 1993, 33, 449.

[233] D. Forney, W. E. Thompson, M. E. Jacox. J. Chem. Phys. 1993, 99, 7393.

[234] Cizek, J. Adv. Chem. Phys. 1969, 14, 35.

[235] Purvis, G. D.; Bartlett, R. J. J. Chem. Phys. 1982, 76, 1910.

[236] G. E. Scuseria, C. L. Janssen, H. F. Schaefer. J. Chem. Phys.1988, 89, 7382.

[237] G. E. Scuseria, H. F. Schaefer. J. Chem. Phys. 1989, 90, 3700.

[238] J. A. Pople, M. Head-Gordon, K. Raghavachari. J. Chem. Phys.1987, 87, 5968.

[239] Hirao, K. Chem. Phys. Lett. 1993, 201, 59.

[240] Campagnola, P. J.; Posey, L. A.; Johnson, M. A. J. Chem. Phys. 1991, 95, 7998.

[241] L. R. McCunn, J. Headrick, M. A. Johnson. Phys. Chem. Chem. Phys. 2008, 10, 3118.

[242] C.-C. Han, M. A. Johnson. Chem. Phys. Lett. 1992, 189, 460.

[243] R. Li, K. A. Hanold, M. C. Garner, A. K. Luong, R. E. Continetti. Faraday Discuss. 1997, 108, 115.

[244] C. E. Klots. J. Chem. Phys. 1985, 83, 5854.

[245] N. I. Hammer, J. R. Roscioli, M. A. Johnson. J. Phys. Chem. A 2005, 109, 7896.

[246] B. C. Dian, J. R. Clarkson, T. S. Zwier. Science 2004, 303, 1169.

[247] J. R. Clarkson, E. Baquero, V. A. Shubert, E. M. Myshakin, K. D.Jordan, T. S. Zwier. Science 2005, 307, 1443.

[248] T. M. Selby, J. R. Clarkson, D. Mitchell, J. A. J. Fitzpatrick, H. D. Lee, D. W. Pratt, T. S. Zwier. J. Phys. Chem. A 2005, 109, 4484.

[249] J. R. Clarkson, B. C. Dian, L. Moriggi, A. DeFusco, V. McCarthy, K. D. Jordan, T. S. Zwier. J. Chem. Phys. 2005, 122.

[250] J. R. Clarkson, E. Baquero, T. S. Zwier. J. Chem. Phys. 2005, 122.

[251] T. S. Zwier. J. Phys. Chem. A 2006, 110, 4133.

[252] T. A. LeGreve, J. R. Clarkson, T. S. Zwier. J. Phys. Chem. A 2008, 112, 3911.

[253] L. A. Posey, M. J. DeLuca, P. J. Campagnola, M. A. Johnson. J. Phys. Chem. 1989, 93, 1178.

[254] S. T. Arnold, R. A. Morris, A. A. Viggiano, M. A. Johnson. J. Phys. Chem. 1996, 100, 2900.

[255] J. R. Roscioli, N. I. Hammer, M. A. Johnson, K. Diri, K. D. Jordan. J. Chem. Phys. 2008, 128, 104314.

[256] N. I. Hammer, J.-W. Shin, J. M. Headrick, E. G. Diken, J. R. Roscioli, G. H. Weddle. M. A. Johnson. Science 2004, 306,675.

[257] N. I. Hammer, J. R. Roscioli, M. A. Johnson. J. Phys. Chem. A 2005, 109, 7896.

[258] N. I. Hammer, J. R. Roscioli, J. C. Bopp, J. M. Headrick, M. A. Johnson. J. Chem. Phys. 2005, 123, 244311.

[259] J. V. Coe, G. H. Lee, J. G. Eaton, S. T. Arnold, H. W. Sarkas, K. H. Bowen, C. Ludewigt, H. Haberland, D. R. Worsnop. J. Chem. Phys. 1990, 92, 3980.

[260] J. Kim, I. Becker, O. Cheshnovsky, M. A. Johnson. Chem. Phys. Lett. 1998, 297, 90.

[261] L. Ma, K. Majer, F. Chirot, B. von Issendorff. J. Chem. Phys. 2009, 131, 144303.

[262] B. M. Elliott, R. A. Relph, J. R. Roscioli, J. C. Bopp, G. H. Gardenier, T. L. Guasco, M. A. Johnson. J. Chem. Phys. 2008, 129, 094303.

[263] R. A. Relph, et. al. Science 2010, 327, 308.

[264] M. Okumura, L. L. Yeh, Myers, J. D.; Lee, Y. TJ. Chem. Phys. 1986, 85, 2328.

[265] L. R. McCunn, J. Headrick, M. A. Johnson. Phys. Chem. Chem. Phys. 2008, 10, 3118.

[266] H. M. Lee, S. Lee, K. S. Kim. J. Chem. Phys. 2003, 119, 187.

[267] T. Tsurusawa, S. Iwata. Chem. Phys. Lett. 1999, 315, 433.

[268] Although both forms I and I' bind the excess electron with a single water molecule in an AA motif, they exhibit different electron binding energies, which are due to subtle differences in their H-bonding arrangements.

[269] A. D. Becke. J. Chem. Phys. 1993, 98, 5648.

[270] J. M. Herbert, M. Head-Gordon. J. Phys. Chem. A 2005, 109, 5217.

[271] T. Shimanouchi. Tables of Molecular Vibrational Frequencies Consolidated, Volume I; National Bureau of Standards: Gaithersburg, MD, 1972; pp 1-160.

[272] J. M. Herbert, M. Head-Gordon. J. Am. Chem. Soc. 2006, 128, 13932.

[273] S. S. Xantheas, T. H. Dunning. J. Chem. Phys. 1993, 99, 8774.

[274] J. O. Jensen, P. N. Krishnan, L. A. Burke. Chem. Phys. Lett. 1995, 246, 13.

[275] S. S. Xantheas. J. Chem. Phys. 1994, 100, 7523.

[276] C. J. Gruenloh, J. R. Carney,C. A. Arrington, T. S. Zwier, S. Y. Fredericks, K. D. Jordan. Science 1997, 276, 1678.

[277] U. Buck, I. Ettischer, M. Melzer, V. Buch, J. Sadlej. Phys. Rev. Lett. 1998, 80, 2578.

[278] C. P. Lawrence, J. L. Skinner. J. Chem. Phys. 2002, 117, 8847.

[279] C. J. Fecko, J. D. Eaves, J. J. Loparo, A. Tokmakoff, P. L. Geissler. Science 2003, 301, 1698.

[280] S. A. Corcelli, C. P. Lawrence, J. L. Skinnee. J. Chem. Phys. 2004, 120, 8107.

[281] K. B. Moller, R. Rey, J. T. Hynes. J. Phys. Chem. A 2004, 108, 1275.

[282] Note that the low-energy band of the AAD molecule was also labeled in this measurement (Figure 40a), but its contribution to the probe signal is so small that the companion AAD band at 2685 cm^{-1} is barely visible, if indeed present. This asymmetry in response occurs because the cross section of the AA transition is much larger than that for the AAD band, in addition to possible nonstatistical population of the isotopomers.

[283] C. Hock, M. Schmidt, R. Kuhnen, C. Bartels, L. Ma, H. Haberland, B. von Issendorff. Phys. Rev. Lett. 2009, 103, 073401.

[284] L. A.Posey, L. A.; M. A. Johnson. J. Chem. Phys. 1988, 89, 4807.

[285] M. Gerhards, C. Unterberg, C.Gerlach, Phys. Chem. Chem. Phys. 2002, 4, 5563.

[286] J. A. Stearns, A. Das, T. S. Zwier. Phys. Chem. Chem. Phys. 2004, 6, 2605.